



**Max-Planck-Institut für Intelligente Systeme**  
*(ehemals Max-Planck-Institut für Metallforschung)*  
Stuttgart

---

# **Stress relaxation mechanisms in thin Sn films and its alloys – Sn whisker formation and its mitigation**

Jendrik Stein

Dissertation  
an der  
**Universität Stuttgart**

---

Bericht Nr. 251  
März 2015



**STRESS RELAXATION MECHANISMS  
IN THIN Sn FILMS AND ITS ALLOYS –  
Sn WHISKER FORMATION AND ITS MITIGATION**

Von der Fakultät Chemie der Universität Stuttgart zur Erlangung der  
Würde eines Doktors der Naturwissenschaften (Dr. rer. nat.)  
genehmigte Abhandlung

Vorgelegt von  
**Jendrik Stein**  
aus Böblingen

Hauptberichter	Prof. Dr. Ir. E. J. Mittemeijer
Mitberichter	Prof. Dr. rer. nat. J. Bill
Prüfungsvorsitzender	Prof. Dr. rer. nat. T. Schleid
Tag der Einreichung	13.01.2015
Tag der mündlichen Prüfung	03.03.2015

MAX-PLANCK-INSTITUT FÜR INTELLIGENTE SYSTEME  
(EHEMALS MAX-PLANCK-INSTITUT FÜR METALLFORSCHUNG)  
INSTITUT FÜR MATERIALWISSENSCHAFT DER UNIVERSITÄT STUTTGART

**2015**



# Table of contents

<b>1</b>	<b>General Introduction.....</b>	<b>9</b>
1.1	Formation and growth of Sn whiskers .....	10
1.1.1	Nucleation and growth models .....	10
1.1.2	Sources of stress leading to Sn whisker growth .....	11
1.2	Mitigation strategies against Sn whisker formation .....	13
1.2.1	Post-bake treatment .....	13
1.2.2	Impact of alloying .....	13
1.2.3	Deposition of additional surface or intermediate layers .....	14
1.3	Focus of this thesis.....	15
1.3.1	Analysis methods.....	15
1.3.2	Outline of this thesis .....	18
1.4	References.....	20
<b>2</b>	<b>Aging time resolved, in-situ, microstructural investigation of tin films electroplated on copper substrates, applying 2D-detector X-ray diffraction ..</b>	<b>23</b>
2.1	Abstract.....	23
2.2	Introduction.....	24
2.2.1	Whisker and hillock growth in the Sn/Cu system .....	25
2.2.2	Microstructural analysis.....	25
2.3	Experimental.....	26
2.3.1	Specimen preparation .....	26
2.3.2	X-ray diffraction analysis .....	27
2.4	Microstructural changes in the as-deposited films; observations as function of aging time and their evaluation.....	32
2.5	Microstructural stability of the post-baked films.....	38
2.6	Microstructural change and whisker formation .....	39
2.7	Conclusions.....	41
2.8	References.....	43

<b>3</b>	<b>The role of silver in mitigation of whisker formation on thin tin films .....</b>	<b>45</b>
3.1	Abstract.....	45
3.2	Introduction.....	46
3.2.1	Whisker growth in the Sn/Cu system .....	46
3.2.2	Effects of alloying of Sn films on Sn whisker growth.....	47
3.3	Experimental.....	48
3.3.1	Specimen preparation and imaging methods.....	48
3.3.2	X-ray diffraction (XRD) methods .....	49
3.4	Results and evaluation .....	49
3.4.1	Initial microstructure .....	49
3.4.2	Microstructural evolution during room temperature aging .....	53
3.5	General discussion .....	59
3.6	Conclusions.....	61
3.7	Appendix.....	62
3.8	Supplementary material .....	63
3.9	References.....	65
<b>4</b>	<b>Microstructural development and possible whiskering behavior of thin Sn films electro-deposited on Cu(Zn)-substrates .....</b>	<b>67</b>
4.1	Abstract.....	67
4.2	Introduction.....	68
4.3	Experimental.....	69
4.3.1	Specimen preparation .....	69
4.3.2	Microscopy and electron back scatter diffraction.....	70
4.3.3	X-ray diffraction (XRD) methods .....	70
4.4	Results.....	72
4.4.1	Phase and microstructural analysis of the as-deposited state .....	72
4.4.2	Stress evolution and microstructural development upon aging at room temperature .....	76
4.5	Discussion.....	80
4.6	Conclusions.....	83
4.7	Acknowledgment.....	83
4.8	References.....	84

<b>5</b>	<b>Imposition of defined states of stress on thin films by a wafer-curvature method; validation and application to aging Sn films.....</b>	<b>87</b>
5.1	Abstract.....	87
5.2	Introduction.....	88
5.3	Experimental.....	89
5.3.1	Experimental setup for stress imposition and specimen preparation.....	89
5.3.2	X-ray diffraction analyses.....	91
5.4	Results and discussion .....	94
5.4.1	Characterization of the imposed state of strain/stress.....	94
5.4.2	Application to aging Sn film in a state of stress .....	97
5.5	Conclusions.....	101
5.6	References.....	102
<b>6</b>	<b>The crystallographic growth directions of Sn whiskers.....</b>	<b>103</b>
6.1	Abstract.....	103
6.2	Introduction.....	104
6.3	Experimental.....	105
6.3.1	Specimen preparation and analysis methods .....	105
6.3.2	Approach for the analysis of the Sn whisker-growth directions.....	107
6.4	Results.....	109
6.5	Discussion.....	112
6.5.1	Relevance of periodic bond chains for whisker growth .....	112
6.5.2	Comparison with experimental results .....	118
6.6	Conclusions.....	119
6.7	Acknowledgment.....	120
6.8	References.....	121
<b>7</b>	<b>Summary .....</b>	<b>123</b>
7.1	Summary in English .....	123
7.2	Zusammenfassung in Deutsch .....	128
	<b>List of publications .....</b>	<b>133</b>
	<b>Danksagung.....</b>	<b>135</b>
	<b>Curriculum vitae .....</b>	<b>137</b>





# Chapter 1

## 1 *General Introduction*

The spontaneous formation of needle-like filaments on metal surfaces is well known and has been reported in the literature for now more than six decades [1,2]. These so-called metallic whiskers (see Fig. 1-1), usually of single crystalline nature [3,4], can grow by a solid state process from the surface of metals with low melting points, as e.g. Cd, Zn, or Sn (see e.g. [1-2,5-7]). Sn whiskers have been first reported by Compton et.al in 1951 [8]. Since then, the scientific and technological interest for this topic has continuously increased: Many research groups have carried out studies in order to investigate and describe the driving force and the nucleation and growth mechanisms and kinetics of, in particular, Sn whiskers (see section 1.1).

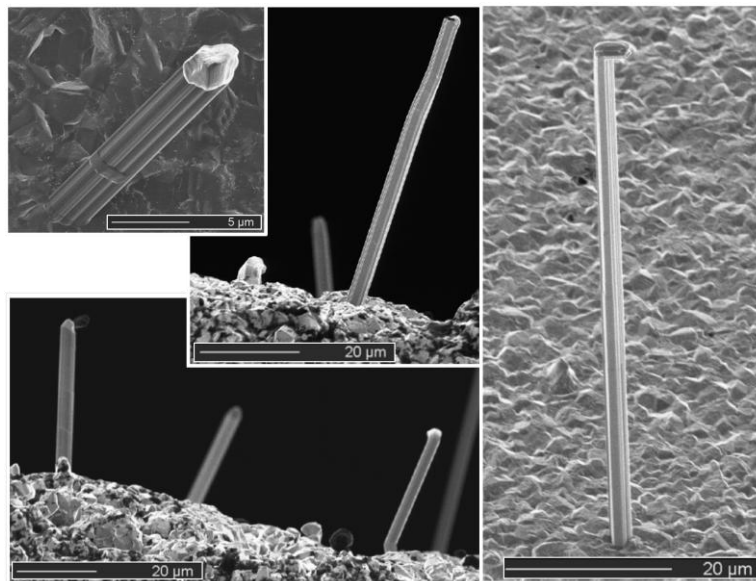


*Fig. 1-1: Exemplary focused ion beam images of Sn whiskers growing from the surfaces of pure Sn films electro-deposited on Cu substrates.*

From the industrial point of view, Sn whisker formation is a severe reliability issue for electronic devices such as electronic control units. Pins of various electronic components, e.g. micro-controllers, are composed of lead frame material (frequently copper based alloys) coated with pure Sn or Sn alloy films since such films possess a good corrosion resistance, favorable electronic properties and good solderability.

However, Sn whiskers (typical diameters are in the range of 0.5 to 10  $\mu\text{m}$ ) can grow from the surface of Sn based films up to lengths of several hundreds of micrometers [5] and thereby can bridge the fine gaps of neighboring conductors which usually results in a failure (short circuit) of the electronic device [9-11]. In order to avoid such failures, several mitigation strategies against Sn whisker formation have been developed and reported in the literature (see section 1.2).

## ***1.1 Formation and growth of Sn whiskers***

### **1.1.1 Nucleation and growth models**

Various Sn whisker growth models have been proposed in the literature in order to explain the spontaneous formation of Sn whiskers by a solid state process on the surface of thin Sn films [2,12]. Some models involve the presence of (a) dislocation(s) either at the center of the whisker, (i.e. a whisker grows with a screw dislocation (and its Burgers vector is) running parallel to its axis allowing migration of atoms to the whisker tip; see e.g. [13]) or at the base of a whisker where a dislocation source (e.g. a Frank-Read dislocation) emits loops towards the surface thereby transferring atoms towards the surface leading to the growth of a whisker from the base (see e.g. [14,15]). In all these models, the dislocation is oriented such that it meets the surface with a component of its Burgers vector normal to the surface [12].

Another group of proposed models is based on recrystallization (see e.g. [5,16-18]) of existing Sn grains at the Sn film surface, e.g. as a consequence of the pile up of dislocations and other defects at grain boundaries as a result of deformation processes inside the Sn film [16].

Some studies indicate that Sn whisker growth can be explained as a stress-driven diffusional creep mechanism (see e.g. [10,19-20]). In a very recent study this idea has been developed most elaborately leading to the following model of the whisker growth mechanism [21].

The electro-deposition of a pure Sn film on a Cu substrate (often) leads to the formation of a predominantly columnar Sn film microstructure where most grain

boundaries are oriented perpendicular to the Sn film surface. Stress introduction (by e.g. irregular formation of the intermetallic compound  $\text{Cu}_6\text{Sn}_5$  at the Sn/Cu interface – cf. section 1.1.2) can take place in such way that stress gradients can develop in the out-of-plane and in-plane direction [22,23]. Sn transport via a Coble type creep mechanism (i.e. diffusion along grain boundaries; [24]) then takes place in the opposite direction of the stress-gradient, i.e. mainly from the bottom region of the Sn film, i.e. from locations where relatively high compressive stresses act, towards the surface (locations with low compressive or tensile stresses). Further, it is suggested that whiskers grow from so-called surface grains, relatively small grains, located at the Sn film surface, with grain boundaries inclined with respect to the surface. At such inclined grain boundaries, shear stresses act due to the (overall) planar state of stress inside the Sn film, which allows the surface grain to grow in the outward, unconstrained direction by gliding (i.e. shearing) along the grain boundaries. It follows that Sn whisker growth can be understood as a (localized) stress-relaxation mechanism [21,25].

### 1.1.2 Sources of stress leading to Sn whisker growth

Several stress generation sources have been reported in the literature, capable of initiating and supporting Sn whisker growth. The most frequently mentioned ones are discussed in the following.

The (likely) best-known stress generation source leading to Sn whisker growth is the chemical reaction between film and substrate inside a Sn/Cu specimen: During room temperature storage of such specimens, Cu diffusion takes place by an interstitial mechanism into the Sn film matrix, whereas Sn diffusion into Cu is negligible at those temperatures [26,27]. Intermetallic compound (IMC)  $\text{Cu}_6\text{Sn}_5$  formation takes place predominantly at triple junctions of the Sn grain boundaries meeting the Sn/Cu interface [25,28-30]. Thus, formation of  $\text{Cu}_6\text{Sn}_5$  takes place in an “irregular” manner, i.e. pyramidal  $\text{Cu}_6\text{Sn}_5$  protrusions on the Sn film side develop leading to a volume increase of up to 43% at these locations (see Fig. 1-2 and [31]). The  $\text{Cu}_6\text{Sn}_5$  reaction can be a continuous stress generation source as long as diffusion of Cu into Sn continuous.

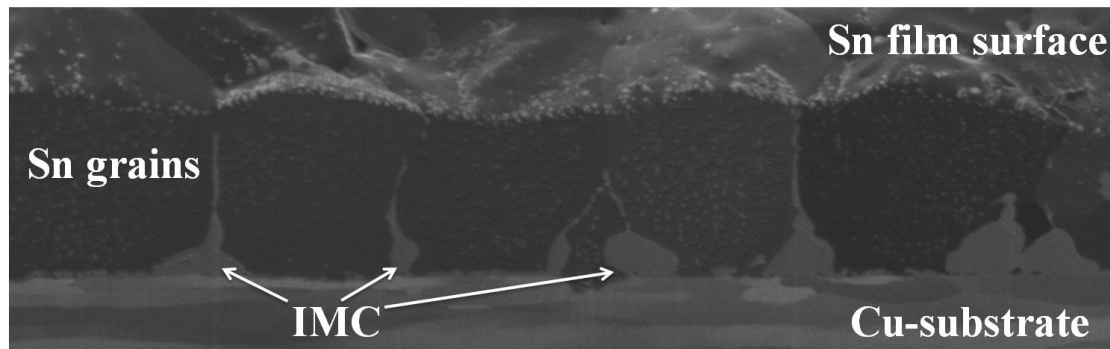


*Fig. 1-2: Exemplary focused ion beam image of a cross-section showing a pure Sn film electro-deposited on Cu substrate after a few weeks of storage at room temperature. Irregular formation of the intermetallic compound (IMC)  $\text{Cu}_6\text{Sn}_5$  takes place predominantly at triple junctions of Sn grain boundaries meeting the Sn/Cu interface.*

Some authors have stated that the formation of Sn oxidation/corrosion products (e.g.  $\text{SnO}_2$ ) at the surface, usually developing at high temperatures and high relative humidity (r.h.) conditions (such as  $60^\circ\text{C}/93\%$  r.h. and  $55^\circ\text{C}/85\%$  r.h.) or in pure oxygen environments, can lead to Sn whisker growth from the surface in the of such products (see e.g. [32-35]). Further, the chemical reaction of Sn with an alloying element (for instance Cu) inside the Sn film, as it can occur in co-deposited Sn-alloy films, is known to be able to support Sn whisker formation [36-38].

Stresses can also be induced already during the Sn film deposition procedure (e.g. when using sputtering techniques for Sn deposition). Such intrinsic stresses are relieved during whisker formation and, in case no additional continuous stress generation source exists, whisker growth usually stops after a short period of time [39,40].

Further, thermal cycling of certain material combinations (e.g. Sn/Fe-based alloys), where film and substrate can show high thermal mismatch as a consequence of significantly different thermal expansion coefficients [41,42], and external applied loads are known to be able to initiate or enhance Sn whisker growth drastically. For the latter case, experimental setups involving e.g. clamps or indenters in direct contact with the Sn surface were often used, often leading to severe plastic deformation at localized regions of the Sn film [43-48].

## ***1.2 Mitigation strategies against Sn whisker formation***

### **1.2.1 Post-bake treatment**

The avoidance of whisker formation has been the focal point of several studies reported in the literature. A widely-used treatment to mitigate Sn whisker formation on Sn/Cu specimens is the so-called “post-bake“ (also denoted as “post-annealing”) treatment: A heat treatment performed usually shortly after Sn film deposition e.g. at 150°C for 1 hour [25,49-50]. An explanation for the Sn whisker mitigating effect of the post-bake procedure has been given in [49]: At elevated temperatures, the IMC morphology changes from irregular (formation of pyramidal protrusions at grain boundary triple junctions) to regular: a continuous IMC layer, consisting of  $\text{Cu}_6\text{Sn}_5$  and  $\text{Cu}_3\text{Sn}$ , forms at the film/substrate interface and further IMC formation during subsequent room temperature storage of these specimens is strongly slowed down. Even though the integral measured state of stress (i.e. the stress state measured over the entire Sn film thickness) is of compressive nature after pronounced room temperature aging times, significant stress-gradients, which are essential for Sn whisker growth [21-23], do not develop under these conditions.

### **1.2.2 Impact of alloying**

It was found empirically already in the 1960’s [51] that alloying Sn with lead (Pb) can mitigate Sn whisker growth on top of thin Sn film surfaces. Sn,Pb alloys replaced pure Sn as coating material for electrical components in the micro-electronic industry (not only due to its Sn whisker mitigating effect but also) due to its favorable melting characteristics. Nowadays, regulations such as the RoHS (restriction of hazardous substances, a directive of the European Parliament) [52] restrict the usage of Pb, which is known to harm health and the environment, and thus alternative Sn alloy film compositions (such as Sn,Cu; Sn,Bi and Sn,Ag,...) were tested with respect to their Sn whisker-growth behavior [37,53-54].

The film morphology of a Sn-alloy film in its initial state directly after (electro-co-) deposition and its development during subsequent storage can be

significantly different as compared to the film morphology of a pure Sn film. In some cases, these changes lead to an increase of the propensity for whisker growth (e.g. Sn-Cu alloys – see section 1.1.2), for other material combinations a reduced risk for Sn whisker growth is observed (e.g. Sn,Pb; Sn,Bi and Sn,Ag.).

The impact of alloying Pb with the Sn on the film microstructure, stress development and whisker growth behavior is described and reported in the literature (see e.g. [10,23,30,55]). The Sn-Pb film microstructure exhibits, in the initial state, an equiaxed grain morphology whereas for (most) pure Sn film usually a predominantly columnar grain morphology is observed. FIB images of the microstructure indicate that Pb forms as separated grains within the film microstructure, however, it is assumed that the Sn grain boundaries are also occupied with Pb. During room temperature storage, the Pb occupation of the Sn grain boundaries leads to an alternation of the Sn-Cu IMC growth-behavior from irregular to a regular growth mode. The formation of such a *planar*  $\text{Cu}_6\text{Sn}_5$  layer at the Sn/Cu interface leads to the development of a lower level of an overall residual compressive stress state/compressive stress-gradients in the Sn-alloy film as compared to the irregular formation in pure Sn films. Further, a high amount of inclined (with respect to the surface) grain boundaries exists in Sn-Pb films due to its equiaxed grain morphology. These inclined grain boundaries are subjected to shear stresses (cf. section 1.1.2) and are therefore able to accommodate creep induced grain shape changes by grain-boundary sliding. Thus, stress relaxation can occur at many locations inside the Sn-Pb films whereas in pure Sn films, only a few locations exist (i.e. the whisker roots) [10,23].

### 1.2.3 Deposition of additional surface or intermediate layers

A popular whisker mitigation strategy is the application of an additional intermediate film (often deposited thin Ni films are used) between Sn film and Cu substrate [31,56-59]: In order to prevent the (irregular) formation of the IMC  $\text{Cu}_6\text{Sn}_5$  in Sn films deposited on Cu substrates, which is known to support and initiate Sn whisker formation (cf. section 1.1.2), a Cu-diffusion barrier (as the Ni layer) can be deposited in-between film and substrate. Even though IMC formation takes also place at the Ni/Sn interface,  $\text{Ni}_3\text{Sn}_4$  (and other Ni-Sn phases [60]) induce usually tensile stresses in the Sn

film [31]. Thus negative compressive stress-gradients, essential for Sn whisker growth, cannot form in the Sn film under these conditions.

Further, covering the surface of a Sn film with a polymer [61] or a metal coating [62,63] can prevent oxidation/corrosion of the Sn film (which can be a stress generation source able to induce whisker formation – cf. section 1.1.2) or even block the growth of Sn whisker.

### ***1.3 Focus of this thesis***

In this thesis project, stress relaxation processes in thin Sn and Sn-alloy films have been investigated and described by employing a combination of well-known and new-developed advanced methods of stress- and microstructural analysis. The role of the film microstructure, as it develops during electro-deposition, and its development during storage of the specimens, on stress development and relaxation, in particular Sn whisker formation and growth, is the focal point of interest for this thesis. Further, the crystallographic growth directions of Sn whiskers have been analyzed and for explanation a model has been derived applying a modified version of the Hartmann-Perdok theory.

#### **1.3.1 Analysis methods**

In order to trace the evolution of film microstructure, composition and state of stress in the electro-deposited Sn or Sn alloy films as a function of room temperature aging time, a combination of several methods was employed: Detailed observation of the Sn film surface was done with help of Scanning electron microscopy (SEM) or Focused ion beam (FIB) microscopy which was operated with a high-energy electron or Ga<sup>+</sup>-beam. These microscopy methods allow the determination of the onset of whisker growth and/or enable gathering information about the growth morphology of Sn whiskers. The observations were carried out at several aging stages of the specimen in order to achieve a time-resolved result.

The film-microstructure below the surface, including the area around the film/surface interface, was investigated preparing cross-sections by FIB milling, i.e. cutting/milling of a trench in the specimen using the high-energy  $\text{Ga}^+$ -beam and a subsequent polishing of one edge/side of the trench. The polished side of the trench can then be imaged when tilting the specimen stage (with the specimen on top) around an axis which is parallel to the surface. This method allows an analysis of the morphology of the Sn (alloy) film and the intermetallic compound developing at the film/substrate interface. However, FIB milling strongly influences diffusion processes and stress states in the proximity of the film where a trench is cut. Thus, in order to gather information about the microstructure at different aging stages under undisturbed conditions, cross-sections had to be prepared at different locations of the specimen.

The phase composition and its evolution were determined applying X-ray diffraction analysis. Diffraction maxima in survey scans of specimens at different aging times were compared with reference patterns of the respective phases from the literature. The relative increase or decrease of a phase volume was traced (in this work the phase evolution of the intermetallic compounds  $\text{Cu}_6\text{Sn}_5$  and  $\text{Ag}_3\text{Sn}$  was investigated) by evaluation of integrated intensities of specific reflections. These peak areas were determined by fitting peaks from the diffraction patterns with a Pseudo Voigt function which were recorded at different aging times but with the same step size and time per step.

Analysis of the film texture was done either by recording pole-figures using X-ray diffraction analysis or by scanning of the film surface of a specimen using an electron back scattered diffraction (EBSD) detector installed in a SEM (i.e. recording of Kikuchi patterns). The EBSD technique was also applied, in combination with FIB microscopy (the FIB is used for determination of the physical growth angles of Sn whiskers), in order to determine crystallographic growth directions along Sn whiskers growth axes.

The state of stress in the Sn film was traced applying laboratory XRD residual stress measurements (see Fig. 1-3) employing the  $\sin^2\psi$ -method. In thin Sn films, the



state of stress is usually planar and rotationally symmetric. Thus, the state of stress parallel to the surface  $\sigma_{\parallel}$  can be calculated from the equation [64]

$$\varepsilon_{\psi}^{hkl} = \left( 2S_1^{hkl} + \frac{1}{2}S_2^{hkl} \sin^2 \psi \right) \sigma_{\parallel} \quad (1.1)$$

using measurements of the strain  $\varepsilon_{\psi}^{hkl}$  at different tilt angles  $\psi$  of the diffraction vector for the  $hkl$  reflection with respect to the specimen surface.

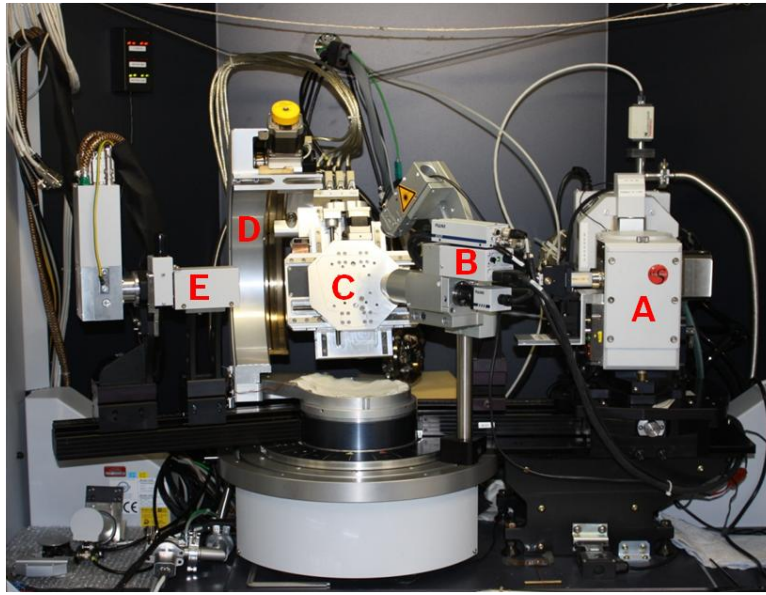


*Fig. 1-3: Photograph of the X-ray diffractometer (XRD) chamber showing the “Bruker AXS D8 Discover diffractometer” with A) X-ray source, B) Laser/video camera system for sample alignment C) sample stage, D) Eulerian Cradle for tilting and rotating of the sample stage and E) X-ray detector.*

A plot of  $\sin^2 \psi$  vs.  $\varepsilon_{\psi}^{hkl}$  allows the determination of  $\sigma_{\parallel}$  by evaluation of the slope of a straight line fitted to the experimental data. The  $hkl$ -dependent diffraction elastic constants  $S_1^{hkl}$  and  $S_2^{hkl}$  were calculated adopting the Neerfeld Hill model using single crystal elastic constants data from the literature [64,65].

Furthermore, applied stress states in Sn films (as well as in thin W films) deposited on a Si wafer substrates were determined by evaluation of the wafer curvature (the coated wafer is bent in case the thin film coating is residually stressed). For such

measurements, the rocking curve scan mode was applied utilizing a Si reflection, i.e. scans were recorded with variable angle of incidence,  $\omega$ , with respect to the film surface on the specimen at fixed diffraction angle,  $2\theta$  set by the detector position. When recording rocking curves at different positions,  $x_i$ , on the film surface, the radius of curvature,  $R$ , can be calculated from the difference in  $\omega$  of the peak maxima of the rocking curves measured at  $x_2$  and  $x_1$ ,  $\Delta\omega$ , applying [66,67]

$$R = \frac{\Delta x}{2 \sin\left(\frac{\Delta\omega}{2}\right)}. \quad (1.2)$$

An additional XRD method, applied in the current work, is the two-dimensional X-Ray diffraction (2D-XRD) analysis [68]. When using a two-dimensional detector, diffracted X-rays from sets of lattice planes of Sn grains in Sn/Cu specimens appear as diffraction spots in the 2D diffraction patterns. A continuous and repeated recording of these 2D diffraction patterns allows tracing of such Sn diffraction spot, i.e. positional and intensity changes can be tracked. Careful interpretation about such changes, allow conclusions about microstructural changes, such as grain rotation and grain growth or dissolution.

### 1.3.2 Outline of this thesis

In *Chapter 2*, stress relaxation processes taking place in pure Sn films electroplated on copper substrates are investigated and described. The method adopted, the two-dimensional X-ray diffraction analysis, enables the study of local microstructural changes (as a result of stress relaxation processes) in as-deposited Sn/Cu specimens. These changes in the microstructure appear before the onset of and accompany Sn whisker growth and can be traced without influencing the processes taking place inside the specimens. The impact of a post-bake procedure on the occurrence of these local microstructural changes is discussed as well.

*Chapters 3 and 4* deal with the role of alloying on the formation/mitigation of Sn whiskers on top of the film surface. Electro-co-deposited Sn,Ag films on pure Cu substrates or pure Sn films electro-deposited on Cu(Zn) substrates with 15% or 36% Zn content are used as specimens. The initial microstructure after electro-deposition and its

development during room temperature storage, in particular the formation rate and growth morphology of the IMC phase  $\text{Cu}_6\text{Sn}_5$  is investigated and described in detail. The results are discussed in light of the current whisker growth model.

In *Chapter 5*, a new developed wafer-curvature method is presented which enables the application of well defined and controllable loads in a contact-free manner and the determination of the stress/strain states of the thin film by two independent X-ray diffraction methods. The validation of this stress-imposition method is carried out with a tungsten film of 500 nm thickness, since tungsten is known to be (practically) intrinsically elastically isotropic. Further, the method is applied to a potentially whiskering, aging Sn film of 3  $\mu\text{m}$  thickness. The decisive role of stress gradients for Sn whisker formation is discussed.

*Chapter 6* is concerned with the crystallographic growth directions of Sn whiskers. Crystallographic directions along whisker axes are determined by a two-step analysis: i) determination of the physical growth angles of the whiskers with respect to a specimen (reference) coordinate system and ii) determination of the crystallographic orientation of the whisker with respect to the crystal coordinate system. The experimental findings of this study (and most of the results presented in the literature as well) are explained by applying, in a modified way, the Hartman-Perdok concept of periodic bond chains, i.e. chains of strong bonds running uninterruptedly through the structure, to the Sn whisker-growth phenomenon.

## 1.4 References

- [1] H.L. Cobb, *Monthly Rev. Am. Electroplaters Soc.* 33, 28-30 (1946).
- [2] G.T. Galyon, *IEEE Trans. Electron. Packag. Manuf.* 28, 94-122 (2005).
- [3] C. Herring, J.K. Galt, *Physical Review* 85, 1060-1061 (1952).
- [4] S. Donald, M. Joseph, R.P. Grant, B. McKenzie, W.G. Yelton, *Met. Mat. Trans* 44A, 1485-1496 (2013).
- [5] V. K. Glazunova, N. T. Kudryavtsev, *Zh. Prikl. Khim.* 36, 543-550 (1963).
- [6] S.E. Koonce, S.M. Arnold, *J. Appl. Phys.* 24, 365-366 (1953)
- [7] W.C. Ellis, *Trans. Met. Soc. AIME* 236,872-875 (1966).
- [8] K.G. Compton, A.A. Mendizza, S.M. Arnold, *Corrosion* 7, 327-334 (1951).
- [9] NASA, Whisker Failures: <http://nepp.nasa.gov/whisker/failures/index.htm>.
- [10] W.J. Boettinger, C.E. Johnson, L.A. Bendersky, K.W. Moon, M.E. Williams, G.R. Stafford, *Acta Mater.* 53, 5033-5050 (2005).
- [11] Y. Fukuda, M. Osterman, M. Pecht, *Electron. Pack. Manuf. IEEE* 30, 36-40 (2007).
- [12] F.R.N. Nabarro, P.J. Jackson, *Growth and Perfection of Crystals* (John Wiley & Sons; Inc, New York, 1958).
- [13] M.O. Peach, *J.Appl.Phys.* 23, 1401-1403 (1952).
- [14] J.D. Eshelby, *Phys.Rev.* 91, 755-756 (1953).
- [15] F.C. Frank, *Phil.Mag.* XLIV, 854-860 (1953).
- [16] P. T. Vianco, J. A. Rejent, *J.Electron. Mat.* 38, 1815-1825 (2009).
- [17] W. C. Ellis, D. F. Gibbons, R. C. Treuting, *Growth and Perfection of Crystals*, edited by Doremus, R. H., Roberts, B. W. and Turnbull, D. (Wiley, New York, 1958), 102-120
- [18] N.Furuta, K. Hamamura, *Jpn. J. Appl. Phys.* 9, 1404-1410 (1969).
- [19] K.N. Tu, C. Chen, A.T. Wu, *J. Mater. Sci. – Mater. Electron.* 18, 269-281 (2007).
- [20] E. J. Buchovecky, N. Jadhav, A. F. Bower, E. Chason, *J. Electron. Mater.* 38, 2676-2684 (2009).
- [21] M. Sobiech, J. Teufel, U. Welzel, E.J. Mittemeijer, W. Huegel, *J. Electron. Mater.* 40, 2300-2313 (2011).
- [22] M. Sobiech, M. Wohlschloegel, U. Welzel, E.J. Mittemeijer, W. Huegel, A. Seekamp, W. Liu, G.E. Ice, *Appl. Phys. Lett.* 94, 221901 (2009).
- [23] M. Sobiech, U. Welzel, E.J. Mittemeijer, W. Huegel, A. Seekamp, *Appl. Phys. Lett.* 93, 011906 (2008).
- [24] R.L. Coble, *J. Appl. Phys.* 34, 1679 (1963).
- [25] B. Z. Lee, D. N. Lee *Acta Mater.* 46, 3701-3714 (1998).
- [26] B.F. Dyson, T.R. Anthony, D. Turnbull, *J. Appl. Phys.* 38, 3408 (1967).
- [27] K.N. Tu, R.D. Thompson, *Acta Metall.* 30, 947-952 (1982).
- [28] M. Sobiech, C. Krueger, U. Welzel, J.Y. Wang, E.J. Mittemeijer, W. Huegel, *J. Mater. Res.* 26, 1482-1493 (2011).
- [29] K.S. Kumar, *J. Mater. Res.* 23, 2916–2934 (2008).
- [30] E. Chason, N. Jadhav, W. L. Chan, L. Reinbold, K. S. Kumar, *Appl. Phys. Lett.* 92, 171901 (2008).

- 
- [31] G. T. Galyon, C. Xu, S. Lal, B. Notohardjono, L. Palmer, Proc. of 55th Electron. Comp. Techn. Conf., 421-428 (2005).
- [32] J. W. Osenbach, J. M. DeLucca, B. D. Potteiger, A. Amin, R. L. Shook, F. A. Baiocchi, IEEE Trans. Electron. Packag. Manuf. 30, 23-35 (2007).
- [33] M. W. Barsoum, E. N. Hoffman, R.D. Doherty, S. Gupta, A. Zavaliangos, Phys. Rev. Lett. 93, 206104 (2004).
- [34] P. Oberndorff, M. Dittes, P. Crema, P. Su, E. Yu, IEEE Trans. Electron. Packag. Manuf. 29, 239-245 (2006).
- [35] E. R., Crandall, G. T. Flowers, R. N. Dean, M. J. Bozack, Proc. of 56th IEEE Holm Conf. Electr. Contacts, 412-416 (2010).
- [36] A.E. Pedigo, C.A. Handwerker, J.E. Blendell, Proc. of 58th Electr. Comp. Techn. Conf. 1498-1504 (2008).
- [37] A. Baated, K. Hamasaki, S.S. Kim, K.S. Kim, K. Suganuma, J. Electron. Mater. 40, 2278-2289 (2011).
- [38] P. Sarabol, A.E. Pedigo, P. Su, J.E. Blendell, C.A. Handwerker, IEEE Trans. Electron. Packag. Manuf. 33, 159-164 (2010).
- [39] E. R. Crandall, G. T. Flowers, R. N. Dean, M. J. Bozack, Proc. of 56th IEEE Holm Conf. Electr. Contacts, 514-519 (2010).
- [40] M. E. Williams, K.-W. Moon, W. J. Boettinger, D. Josell, A.D. Deal, J. Electron. Mater. 36, 214-219 (2007).
- [41] C. M. Chen, P. Y. Shih J. Mater. Res. 23, 2668-2675 (2008).
- [42] N. Vo, Y. Nadaira, T. Matsura, M. Tsuruya, R. Kangas, J. Conrad, B. Sundram, K. Lee, S. Arunsalam, Proc. of IEEE Electron. Comp. Techn. Conf., 213-218 (2001).
- [43] K. Suganuma, A. Baated, K. S. Kim, K. Hamasaki, N. Nemoto, T. Nakagawa, T. Yamada, Acta Mater. 59, 7255-7267 (2011)
- [44] V. K. Glazunova, Sov. Phys. – Crystallogr. Sov. Phys. 7, 761-766 (1962).
- [45] H. Moriuchi, Y. Tadokoro, M. Sato, T. Furusawa, N. Suzuki, J. Electron. Mater. 36, 220-225 (2007).
- [46] S. K. Lin, Y. Yorikado, J. X. Jiang, K. S. Kim, K. Saganuma, S. W. Chen, M. Tsujimoto, I. Yanada, J. Mater. Res. 22, 1975 (2007).
- [47] S. K. Lin, Y. Yorikado, J. X. Jiang, K. S. Kim, K. Suganuma, S. W. Chen, M. Tsujimoto, I. Yanada, J. Electron. Mater. 36, 1732-1734 (2007).
- [48] B. Horvaacuteth, G. Harsaacutenyi, Proc. of 15th Intern.Symp. Design Techn. Electron. Pack. 389 (2009).
- [49] M. Sobiech, U. Welzel, R. Schuster, E.J. Mittemeijer, W. Huegel, A. Seekamp, V. Muller, Proc. of IEEE 57th Electro. Comp. Techn. Conf., 192-197 (2007).
- [50] J. W. Osenbach, R. L. Shook, B. T. Vaccaro, B. D. Potteiger, A.N. Amin. K.N. Hooghan, P. Suratkar, P. Ruengsinub, IEEE Trans. Electron. Packag. Manuf. 28, 36-62 (2005).
- [51] S.M. Arnold, Plating 53, 96-99 (1966).
- [52] European-Parliament (2003). Official Journal of the European Union L37.
- [53] R. Schetty, W. Sepp, Proc. of 11th Electron. Pack. Techn. Conf., 225-234 (2009).
- [54] N. Jadhav, M. Williams, F. Pei, G. Stafford, E. Chason, J. Electro. Mat. 42, 312-318 (2013).
- [55] N. Jadhav, J. Wasserman, F. Pei, E. Chason, J. Electron. Mater. 41, 588 (2012)
- [56] K. Whitlaw, J. Crosby, Proc. of AESF SUR/FIN Conf., 289 (2003).

- [57] Britton S. C. *Trans. Inst. Metal Finish.* 52, 95-102 (1974).
- [58] C. Xu, Y. Zhang, C. Fan, J. A. Abys, *CircuitTree* 15, 94-105 (2002).
- [59] L. Sauter, A. Seekamp, Y. Shibata, Y. Kanameda, H. Yamashita, *Micro.Reliability* 50, 1631–1635 (2010).
- [60] G. Gosh, *Met. Mat. Trans A* 40, 4-23 (2009)
- [61] T. A. Woodrow, E. A. Ledbury, *Proc. of IPC/JEDEC 8th Intern.Conf. Lead-Free Electron. Comp. Assemblies*, 18-20 (2005).
- [62] E.R. Crandall, G.T. Flowers, P. Lall, M.J. Bozack, *Proc. of. IEEE 58th Holm Conf. Electr. Contacts*, 1-6 (2012).
- [63] L. Reinbold, N. Jadhav, E. Chason, and K. S. Kumar, *J. Mater. Res.* 24, 3583-3589 (2009).
- [64] U. Welzel, J. Ligot, P. Lamparter, A. C. Vermeulen, E. J. Mittemeijer, *J. Appl. Crystallogr.* 38, 1-29 (2005).
- [65] C. J. Smithells, E. A. Brandes, *Metal reference book* (Butterworths, London, 1976).
- [66] K. J. Martinschitz, E. Eiper, S. Massl, H. Kostenbauer, R. Daniel, G. Fontalvo, C. Mitterer, J. Keckes, *J. Appl. Crystallogr.* 39, 777-783 (2006).
- [67] A. Segmueller, I. C. Noyan, V. S. Speriosu, *Prog. Cryst. Growth Charact. Mater.* 18, 21-66 (1989).
- [68] B. He, *Two-Dimensional X-Ray Diffraction*. (John Wiley & Sons; Inc. Hoboken, New Jersey, 2009).

## Chapter 2

### ***2 Aging time resolved, in-situ, microstructural investigation of tin films electroplated on copper substrates, applying 2D-detector X-ray diffraction***

J.Stein<sup>1,2</sup>, U. Welzel<sup>1</sup>, W. Huegel<sup>2</sup>, S. Blatt<sup>2</sup>, and E.J. Mittemeijer<sup>1,3</sup>

<sup>1</sup> Max Planck Institute for Intelligent Systems (formerly Max Planck Institute for Metals Research), Heisenbergstr. 3, 70569 Stuttgart (Germany)

<sup>2</sup> Robert Bosch GmbH, Automotive Electronics / Engineering Assembly Interconnection Technology (AE/EAI2), Robert-Bosch-Str. 2, 71701 Schwieberdingen (Germany)

<sup>3</sup> University Stuttgart, Institute for Materials Science, Pfaffenwaldring 55, 70569 Stuttgart (Germany)

Key words: Sn whisker formation, creep, two-dimensional x-ray diffraction, grain rotation, grain growth

#### ***2.1 Abstract***

Pure thin, tin films, electroplated on copper substrates, were investigated by X-ray diffraction analysis, in-situ during room-temperature aging, using a laboratory diffractometer equipped with a two-dimensional detector. Diffraction spots of single Sn grains in the Sn film could be observed and traced over time by using the diffraction method adopted. For the as-deposited specimens, outspoken changes of the Sn reflection spots, concerning their position and intensity, as well as sudden appearances and disappearances of additional diffraction spots, were observed. This could be ascribed to local microstructural changes in the films such as grain rotation, grain growth and grain dissolution. In contrast with the as-deposited specimens, so-called post-baked specimens (i.e. annealed at 150 °C ( $\approx$  423 K) for 1 h after layer deposition) exhibited a stable microstructure. The results obtained were discussed with respect to their relevance for the Sn whisker-growth phenomenon.

## ***2.2 Introduction***

Filamentary, needle-like single crystals of Sn or other metals, such as e.g. Ag, Cu, Co [1], Cd [2], Si [3] or Zn [4], are denoted as metallic “whiskers”. Galvanic deposited Sn coatings are frequently used, in the electronic components industry, as protective layers against corrosion of the lead frame material (frequently composed of Cu based alloys) in electronic devices, since Sn films, next to a good corrosion resistance, possess favorable electronic properties and good solderability. Sn whiskers can grow on top of (and out of these) films up to lengths of several millimeters [2] and are therefore able to bridge fine-pitched gaps between conductors [5] which can lead to electronic failures [6,7].

Research in order to understand and to prevent Sn whisker growth has been carried out already since the 1950’s [8]. An interim solution for the Sn whisker-growth problem was found empirically by usage of Sn-Pb alloys as coating material [9], which were found to be much less prone to whisker formation compared to pure Sn films [10,11]. Nowadays, regulations such as RoHS (=Restriction of hazardous substances in electrical and electronic equipment - a directive of the European Parliament [12]) restrict the implementation of Pb which is known to harm health due to its toxicity [13]. Thus, the scientific and technological interest for research on whisker development has been reinvigorated.

In order to understand the Sn whisker-growth phenomenon and, on the basis of this knowledge, to find whisker-growth mitigation strategies, it is necessary to understand the mechanisms which lead to whisker growth and thus to investigate the processes which take place inside the film material during and before whisker development. In this work, the focus is on microstructural changes taking place in pure Sn films electrodeposited on pure Cu substrates during room temperature aging.



### 2.2.1 Whisker and hillock growth in the Sn/Cu system

Electro-deposition of a thin, pure Sn film on a Cu substrate, using an industrial Sn electrolyte, leads usually to a predominantly columnar<sup>1</sup> Sn grain morphology [10]. Cu diffuses with an interstitial mechanism [14,15] into the tin matrix during aging at ambient temperatures and the intermetallic compound (IMC)  $\text{Cu}_6\text{Sn}_5$  forms as an irregular layer at the Sn/Cu interface exhibiting pyramidal protrusions along Sn grain boundaries at triple junctions of Sn grain boundaries with the Sn/Cu interface [16,17]; diffusion of Sn into Cu is negligible at ambient temperatures. Thus, formation of IMC takes place at the Sn film side (see also the thermodynamic analysis in Ref. [17]), which leads to a volume increase of up to 43% in the bottom region of the Sn film [18]. It was shown experimentally that in-plane and out-of-plane strain *gradients* develop inside the Sn film as a response [19]. These strain gradients provide the driving force for transport of Sn [20] through its grain boundaries (Coble creep [21]) towards the surface and thus Sn whisker growth can be initiated and supported (cf. discussion in [10]); Sn whisker growth can thereby be regarded as a diffusion controlled, stress relief phenomenon.

Sn whiskers can be straight, curved, curled or kinked [22]. Usually, the whisker has a practically constant periphery which is defined by the surrounding grains at its root. If extensive lateral grain growth takes place during whisker formation in the substrate at the whisker root, which is connected with grain-boundary movement and thus consumption of one or more neighboring grains, the Sn protrusion at the surface is denoted as hillock. Typically, aspect ratios of hillocks are smaller than one, i.e. their height is smaller than their diameter [10, 23-25].

### 2.2.2 Microstructural analysis

Apart from surface characterization, possibly time resolved, as by application of scanning electron microscopy (e.g. see Refs. [22-23,26]), genuine microstructural analysis requires application of transmission electron microscopy techniques or x-ray diffraction techniques (see what follows). However, preparation of electron transparent

---

<sup>1</sup> It is also possible to achieve a non-columnar, more equiaxed tin grain morphology, for instance by electro-co-deposition of Sn alloy (e.g. Sn-Pb) films. For further details, the reader is referred to Ref. [10].

foils, as by FIB machining or other techniques, leads to stress relaxation, and hence such (cross-) sections cannot be used for in-situ observations of local microstructural changes.

Against this background, an approach is presented in this paper for non-destructive, in-situ microstructural investigation of the aging Sn film based on a two-dimensional x-ray diffraction technique using a laboratory X-ray diffractometer. A fundamental advantage of the 2D-XRD technique (see Ref. [27]) is that a wide range of orientations and lengths of the diffraction vector is collected in one diffraction pattern in a relatively short period of time (i.e. generally only a few seconds are needed), thereby making possible in-situ studies with high time resolution. Conclusions about the microstructure (e.g. number of grains in the illuminated specimen volume, texture, etc.) of the investigated specimen can be drawn from e.g. the spottiness or the intensity distribution of the diffraction rings on the diffraction patterns. Further, one dimensional diffraction patterns can be achieved from the 2D patterns by integration (i.e. summing up) of e.g. intensities pertaining to a particular length of the diffraction vector but to different orientations. Thus, good statistics can be achieved in a relatively short period of time.

It will be shown in the following that application of this 2D-XRD technique allows direct detection of microstructural changes, such as grain rotation, grain growth and grain dissolution.

## ***2.3 Experimental***

### **2.3.1 Specimen preparation**

Pure thin Sn films, with a thickness of  $\sim 3 \mu\text{m}$  were electroplated on pure Cu substrates (“Wieland” platelets with dimensions:  $2.5 \text{ cm} \times 1.5 \text{ cm} \times 1 \text{ mm}$ ) at room temperature using an industrial “matte-tin” electrolyte and a current density of  $1.5 \text{ A/dm}^2$ . The Sn film thickness and microstructure were determined with help of scanning electron microscopy (SEM) images of cross sections prepared with a Novo 600 NanoLab focused ion beam (FIB) workstation (“FEI”). The tin grains were found to be

predominantly of columnar morphology (with grain boundaries perpendicular to the surface of the film) with an in-plane size between ~1 to 5  $\mu\text{m}$ .

Two types of specimen were used: Specimens in as-deposited state without any additional post-plating treatment and specimens subjected to a post-bake treatment (also called post-plating annealing) directly after layer deposition by annealing the specimens for 1 h at 150°C ( $\approx 423$  K) in a conventional furnace.

The as-deposited specimens were investigated directly after Sn deposition whereas the post-baked specimens were investigated directly after the post-bake treatment, in both cases using the two-dimensional X-ray diffraction (2D-XRD) technique (see section 2.3.2) during room temperature storage.

### 2.3.2 X-ray diffraction analysis

The measurements were performed applying a “Bruker AXS D8 Discover diffractometer” with Cu- $K_{\alpha}$  radiation. The X-ray source of this diffractometer was a “TXS Superspeed” rotating anode (50 kV / 20 mA) operating in point-focus mode with a size of  $0.1 \times 1$  mm focal spot size. A 2D-collimating mirror (“Xenocs Fox 2D”) was used for parallelizing as well as for monochromizing the X-ray beam. A pinhole with 200  $\mu\text{m}$  diameter was installed in order to reduce the area of illumination of the specimen. The diffractometer was equipped with a “Huber” 1/4-circle Eulerian cradle, which allows tilting and rotating of the specimen stage. The diffracted X-rays were detected using a gas-filled 2D area detector (“Bruker Highstar”). Specimen alignment was performed with help of a justified laser and video camera system. The diffractometer chamber was air-conditioned in order to maintain a constant temperature of about 22 °C. The diffractometer was operated utilizing the “2D-GADDS” software which was also used to carry out flood field and spatial-distortion corrections [29] of the 2D diffractograms. Additional software (custom-made) was needed for data export and analyses.

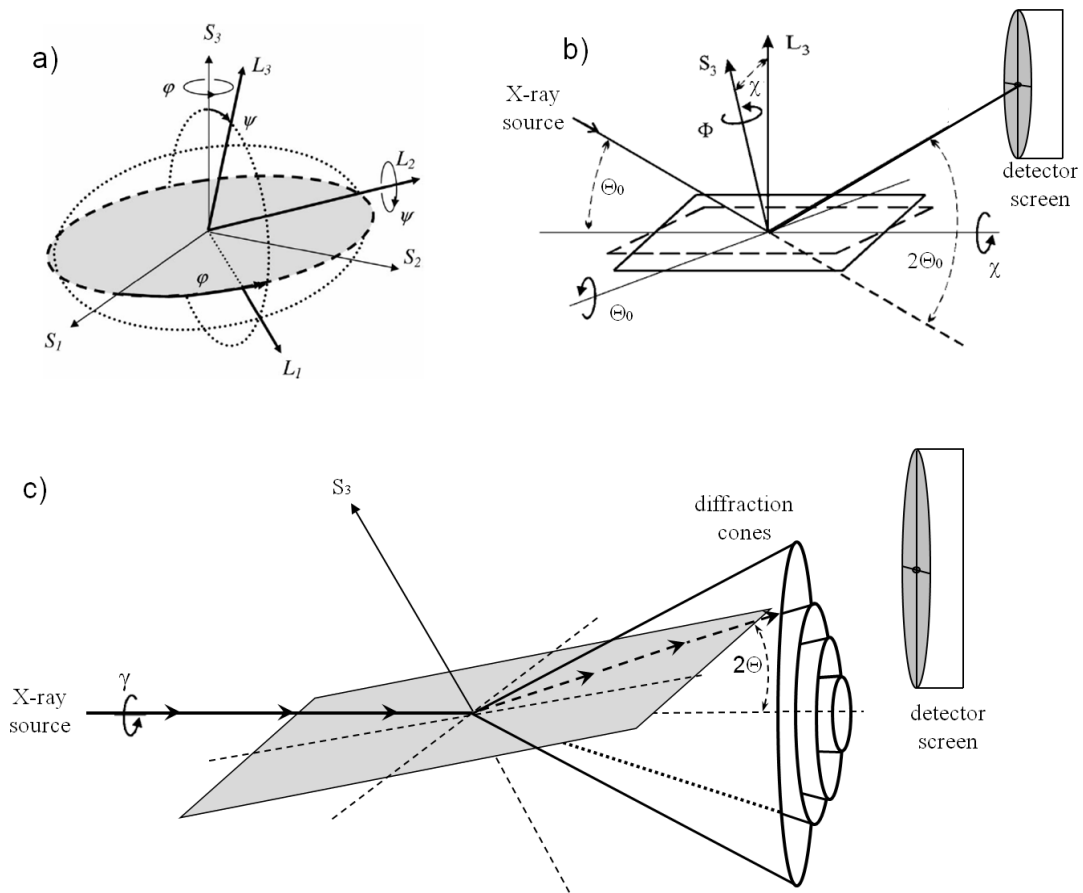


Fig. 2-1: a) and b): Definition of angles and relations between the specimen frame of reference ( $S$ ) and the laboratory frame of reference ( $L$ ) required to describe the XRD geometry (see also text) – images are taken (modified) from Welzel et al., 2005. c): X-rays are diffracted by sets of lattice planes of multiple grains within a polycrystalline sample along diffraction cones. The 2D detector screen records cuts through the diffraction cones. The specimen surface is indicated either as grey area (in a) and c)) or as (transparent) area with dashed lines in b). The diffracting lattice is indicated as (transparent) area with solid lines.

The various angles, required to describe the X-ray diffraction geometry are illustrated in Fig. 2-1 and will be defined in the following. All specimens were mounted on top of the specimen stage such that the specimen-stage surface normal and the specimen-surface normal coincide. The definition and relations between the (Cartesian) specimen frame of reference ( $S$ ) and the (Cartesian) laboratory frame of reference ( $L$ ) are shown in Figs. 2-1 a) and b): The  $S_1$  and  $S_2$  axes are oriented parallel with (i.e. in-plane) and the  $S_3$  axis is oriented perpendicular to (i.e. out-of-plane) the specimen/specimen-stage surface. The  $L_3$  axis of the laboratory frame of reference, per

definition, coincides with the diffraction vector (=normal of the set of diffracting  $\{hkl\}$  lattice planes). As illustrated in Fig 2-1 a), the specimen frame of reference and the laboratory frame of reference coincide for  $\psi = \varphi = 0$ . The tilt angle  $\psi$  is given by the angle between the normal of the specimen surface,  $S_3$ , and the normal of the set of diffracting lattice planes,  $L_3$ , and  $\varphi$  is the angle of rotation about the specimen-surface normal  $S_3$  (If  $\psi = 0$ , the value of  $\varphi$  is irrelevant for the diffraction process).

The angles  $\psi$  and  $\varphi$  describe the orientation of the normal of a set of  $\{hkl\}$  planes with respect to the specimen frame of reference  $S$  (see text above and Fig. 2-1 a) whereas the instrumental angles  $\chi$  and  $\Phi$  (describing the orientation of the specimen-stage with respect to the laboratory system  $L$ ) are only used to bring  $\{hkl\}$  planes, oriented in a certain way in the specimen, into diffracting conditions (s. Fig. 2-1 b). For a set of  $\{hkl\}$  planes in diffraction conditions at the center of the 2D detector (as indicated as an area with dashed lines in Fig. 2-1 b) with  $2\Theta_0$  as twice the diffraction angle considered at the center of the 2D detector screen,  $\Phi$  is defined as the rotation angle about the specimen-stage surface normal  $S_3$  and  $\chi$  as the angle of rotation of the specimen-stage around an axis defined by the intersection of the diffraction plane. The values of  $\chi$  and  $\psi$  as well as the values of  $\Phi$  and  $\varphi$  equal (or are simply related by a constant offset) when considering these values at the center of the 2D detector screen. In the setup applied for our investigations, the diffraction angle  $\Theta_0$ , considered at the center of the diffraction screen, is taken two times the corresponding angle between the incident X-ray beam axis and the diffracting lattice plane (cf. Fig. 2-1 b). For further details, the reader is referred to Refs. [28,29].

As indicated in Fig. 2-1 c), X-rays interacting with a polycrystalline sample are diffracted by sets of lattice planes in diffraction conditions, of multiple grains within the illuminated specimen volume, along diffraction cones. A particular diffraction corresponds with a fixed diffraction angle  $2\Theta$  (=half of the opening angle (“semi-angle”) of the cone) and is connected to the lattice spacing  $d$  of the diffracting lattice planes as well as to the wavelength  $\lambda$  of the X-rays according to Bragg’s law. A cut through the diffraction cones is recorded by the 2D detector screen, as can be seen in Fig. 2-2 showing an exemplary 2D diffraction pattern recorded from a Sn layer on a Cu specimen: Diffracted intensity from Cu and Sn is shown a function of  $2\Theta$  (horizontal

direction) and  $\gamma$  (azimuthal angle). The angle  $\gamma$  (cf. Fig. 2-1 c) is the rotation angle of the diffraction vector around the direction of the incident beam (An expression of  $\gamma$  as function  $\psi$  and  $\varphi$  cannot be given with simple relationships. For further details, see He, 2009). Diffracted intensity variations have been indicated in Fig. 2-2: from low to high intensity corresponds with color changes from orange to white. Only a minute fraction of the Sn grains in the illuminated specimen volume have lattice planes in diffracting condition. Since a pinhole was used, which reduces the illuminated specimen volume, a diffraction spot on the detector is in most cases caused by one single Sn grain inside the Sn film: Of course, the diffraction spots of different, but crystallographically identically oriented grains, in principle, coincide on the detector, which is however unlikely for the Sn film in view of the small illuminated volume (about  $360000 \mu\text{m}^3$ , containing about 5000 Sn grains). If several grains within the illuminated specimen volume have orientations close to each other, overlapping of the diffraction spots takes place which leads to a (partially) closed diffraction circle/ellipse. This is the case for the Cu substrate, which has considerably smaller grains as compared to the Sn film. Since the Sn films (as well as the Cu substrates) are weakly textured, the distribution of diffraction spots along the intersection of the diffraction cone with the detector screen is somewhat inhomogeneous.

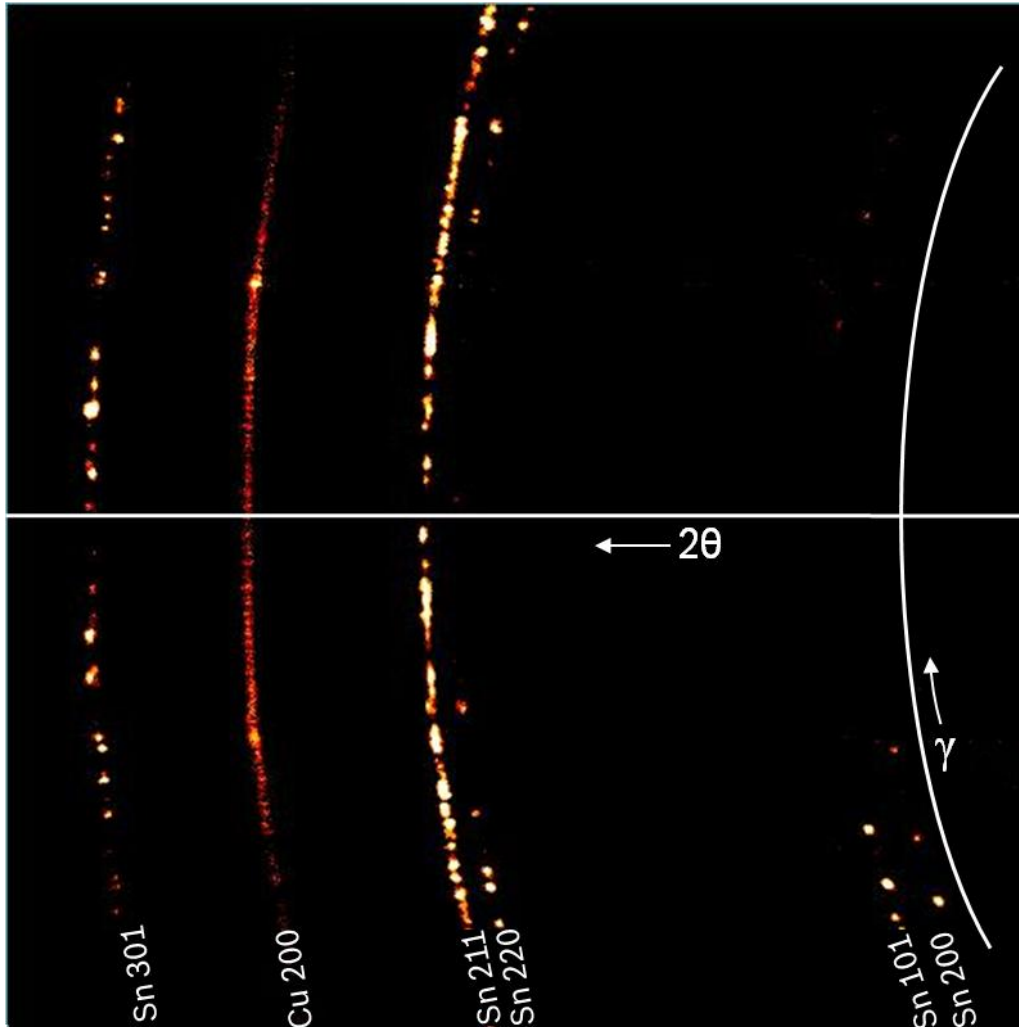


Fig. 2-2: 2D diffraction pattern recorded from an as-deposited Sn/Cu specimen applying the 2D-XRD technique. The diffraction pattern shows cuts through diffraction cones originating from a Sn film and the Cu substrate as function of  $2\theta$  (horizontal distance) and  $\gamma$  (azimuthal angle). The diffraction pattern was recorded in the detector and specimen-stage position given by the instrumental angles:  $2\theta_0=42^\circ$ ,  $\chi=0^\circ$  and  $\Phi=0^\circ$ .

Several specimens, both as deposited and post-baked specimen, were subjected to the 2D-XRD technique immediately after deposition or after the post-bake treatment, respectively, most of them for a maximum investigation time of 120 hours (5 days) per specimen. A few of the as-deposited samples were investigated up to three weeks. Diffraction patterns were recorded at eight or ten different detector and specimen-stage positions as given by the values of  $2\theta_0$  and  $\chi$  (cf. Fig. 2-1 and its above discussion and see Tabs. 2-1 and 2-2) in order to get several grains with different orientations with respect to the specimen frame of reference in diffracting condition. One diffraction

pattern in each of the employed detector and specimen-stage position was taken at 30 min intervals; the measurement time per diffraction pattern was kept constant (=12 seconds). The diffraction patterns were analyzed by subtracting patterns taken after different times of aging at room temperature using image processing software (cf. Figs. 2-9 and 2-10) or by comparing the images simply by eye.

*Tab. 2-1: Listing of one set of eight different detector and specimen-stage positions (i.e. listing of the instrumental angles  $2\theta_0$  and  $\chi$ . Value for  $\Phi$  was left constant at  $0^\circ$ ) employed for the investigation of as-deposited and post-baked Sn films on Cu substrates during aging at room temperature (pertains to the results shown in Figs. 2-2 to 2-6 and Figs. 2-9 and 2-10)*

No.	1	2	3	4	5	6	7	8
$2\theta_0$	$42^\circ$	$42^\circ$	$42^\circ$	$42^\circ$	$68^\circ$	$68^\circ$	$68^\circ$	$68^\circ$
$\chi$	$0^\circ$	$20^\circ$	$40^\circ$	$60^\circ$	$0^\circ$	$20^\circ$	$40^\circ$	$60^\circ$

*Tab. 2-2: Listing of a set of ten different detector and specimen-stage positions (i.e. listing of the instrumental angles  $2\theta_0$  and  $\chi$ . Value for  $\Phi$  was left constant at  $0^\circ$ ) employed for the investigation of as-deposited Sn films on Cu substrates during aging at room temperature (pertains to the result shown in Fig. 2-7)*

No.	1	2	3	4	5	6	7	8	9	10
$2\theta_0$	$30^\circ$	$30^\circ$	$30^\circ$	$30^\circ$	$30^\circ$	$60^\circ$	$60^\circ$	$60^\circ$	$60^\circ$	$60^\circ$
$\chi$	$0^\circ$	$15^\circ$	$30^\circ$	$45^\circ$	$60^\circ$	$0^\circ$	$15^\circ$	$30^\circ$	$45^\circ$	$60^\circ$

## ***2.4 Microstructural changes in the as-deposited films; observations as function of aging time and their evaluation***

Several striking changes, concerning both the position and the intensity of Sn diffraction spots, as well as appearances and disappearances of new diffraction spots, were found by investigation of the as-deposited specimens (see Figs. 2-3 to 2-7). All of the findings presented below are exemplary results; their observations were made several times at different locations in the diffraction patterns and at different aging times upon investigating the as-deposited specimens.



A frequently appearing type of change is the sudden appearance of an additional diffraction spot which disappears after a short period of time. Such an additional reflection spot is visible usually only in a single 2D diffraction pattern (2D diffraction patterns were recorded in 30 min intervals, cf. section 2.3.2). See Fig. 2-3: A diffraction pattern taken after 111.5 hours at room temperature aging is shown in Fig. 2-3 a). An enlarged part of this diffraction pattern is shown in Fig. 2-3 b) together with the same enlarged parts recorded as half an hour before and half an hour later for the same detector and specimen-stage positions; the extra diffraction spot occurs only in the diffraction pattern recorded at 111.5 h.

A similar observation is presented in Fig. 2-4. Here, the additional diffraction spot appears close to the position of an existing reflection spot which leads to a remarkable intensity increase at that location (see diffraction pattern recorded at 80.5 h as shown in Fig. 2-4 b).

Another type of observation involves the migration of a diffraction spot. A series of eight successive diffraction patterns at 30 min intervals is shown Fig. 2-5 b). The area enclosed by the white ellipse in the figures contains two diffraction spots: One of them is immobile and of constant intensity (i.e. the low intensity diffraction spot at the bottom part of the white ellipse) and one of them moves in association with a simultaneous change of intensity. The positional change of this migrating diffraction spot has been indicated with help of a sequence of circles in Fig. 2-5 c).

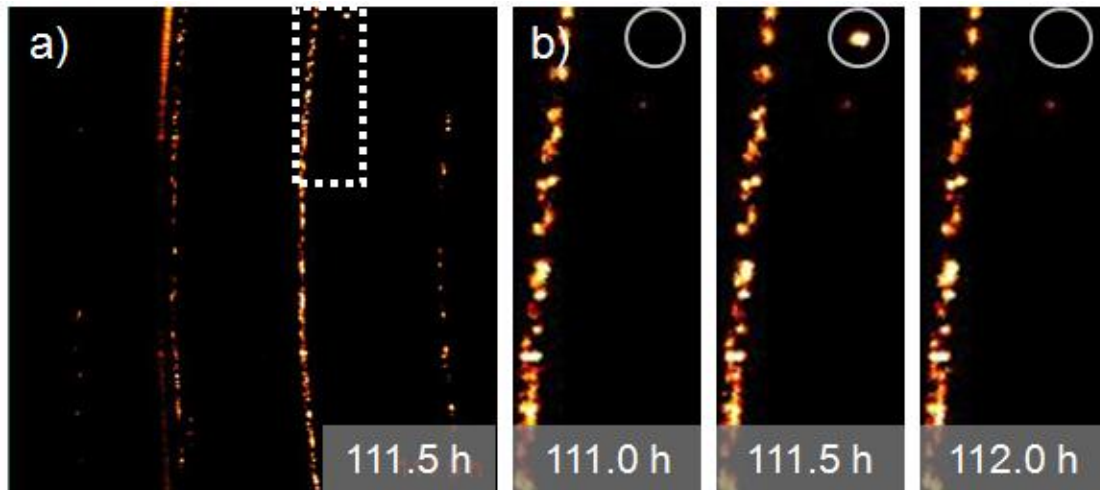


Fig. 2-3: a) 2D diffraction pattern and b) enlarged series of cutouts, for the indicated aging times at room temperature, revealing an additional appearing and subsequently disappearing  $S_n$  diffraction spot. The diffraction patterns are recorded in the detector and specimen-stage position given by the instrumental angles:  $2\Theta_0=68^\circ$ ,  $\chi=0^\circ$  and  $\Phi=0^\circ$ .

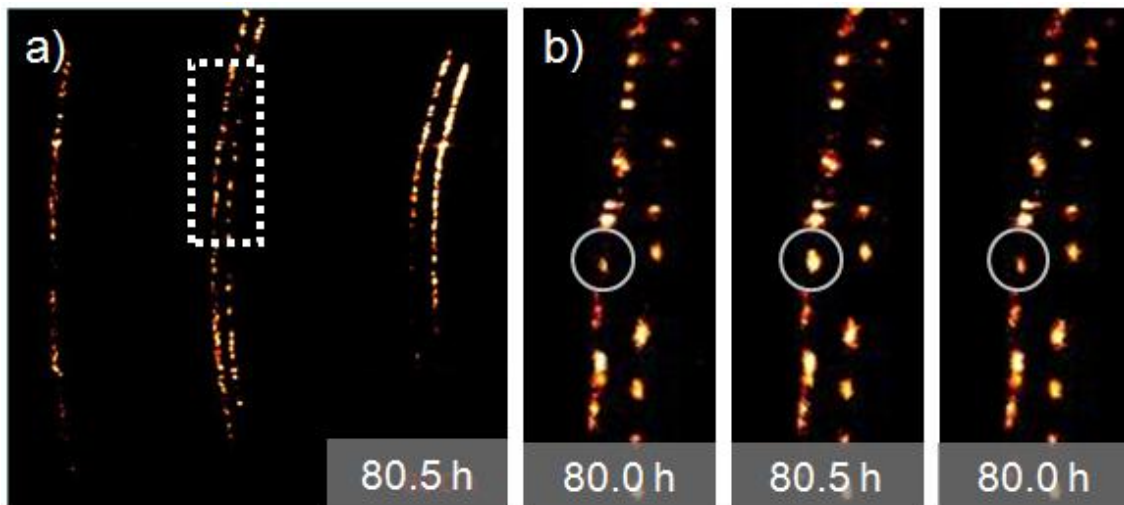


Fig. 2-4: a) 2D diffraction pattern and b) enlarged series of cutouts, for the indicated aging times at room temperature, revealing an additional appearing and subsequently disappearing  $S_n$  diffraction spot. The additional diffraction spot appears here at about the same position as that of an already existing spot, which leads to a remarkable intensity increase. The diffraction patterns were recorded in the detector and specimen-stage position given by the instrumental angles:  $2\Theta_0=42^\circ$ ,  $\chi=60^\circ$  and  $\Phi=0^\circ$ .

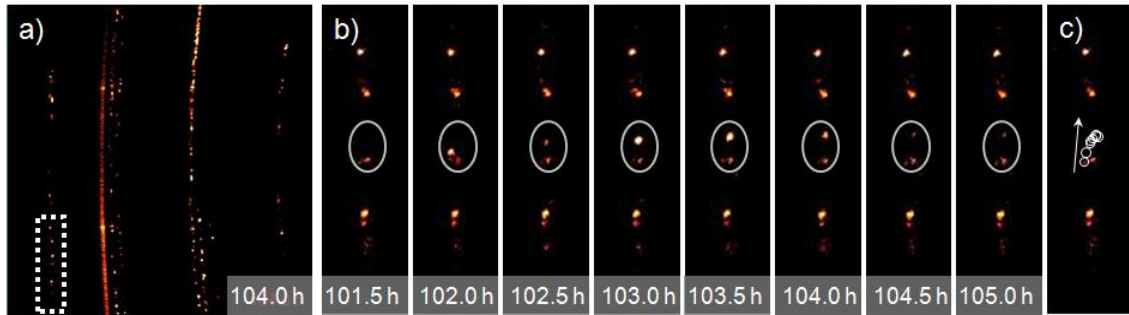


Fig. 2-5: a) 2D diffraction pattern and b) enlarged series of cutouts, for the indicated aging times at room temperature, revealing a migrating Sn diffraction spot. The successive positions of the migrating diffraction spot have been indicated by weight circles in c). The diffraction patterns were recorded with the detector and specimen-stage position given by the instrumental angles:  $2\Theta_0=68^\circ$ ,  $\chi=20^\circ$  and  $\Phi=0^\circ$ .

The findings shown in Figs. 2-3 to 2-5 take place within a relatively short period of time (half an hour to a few hours). Some other changes in the diffraction patterns take place on the time scale of several days or even during the entire time of investigation:

The diffraction patterns shown in Fig. 2-6 b) reveal the emergence of two Sn reflection spots at different moments of time and of intensities which relatively slowly increase with time. Generally it was observed that diffraction spots can exhibit increase and/or decrease of their intensities (also increase followed by a decrease: see Fig. 2-7) during long periods of time.

Since the diffraction spots generally pertain to only a single Sn grain inside the Sn film (cf. section 2.3.2 and the start of section 2.6), the above observations can be interpreted as local microstructural changes such as grain rotation, grain growth and grain dissolution occurring at room temperature in the as-deposited Sn films, as follows from the subsequent discussion.

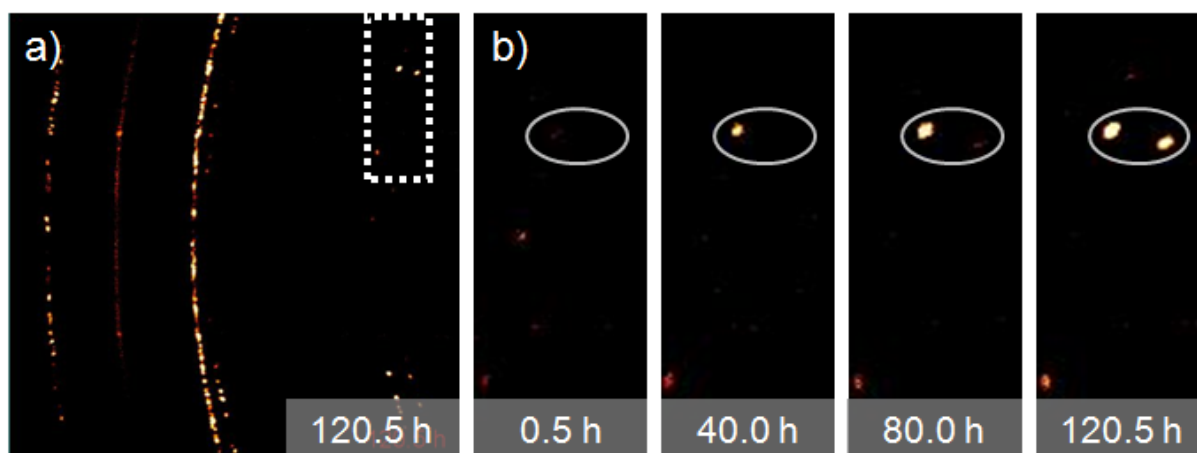


Fig. 2-6: a) 2D diffraction pattern and b) enlarged series of cutouts, for the indicated aging times at room temperature, revealing two Sn diffraction spots, slowly increasing their intensity. The diffraction patterns were recorded in the detector and specimen-stage position given by the instrumental angles:  $2\Theta_0=42^\circ$ ,  $\chi=0^\circ$  and  $\Phi=0^\circ$ .

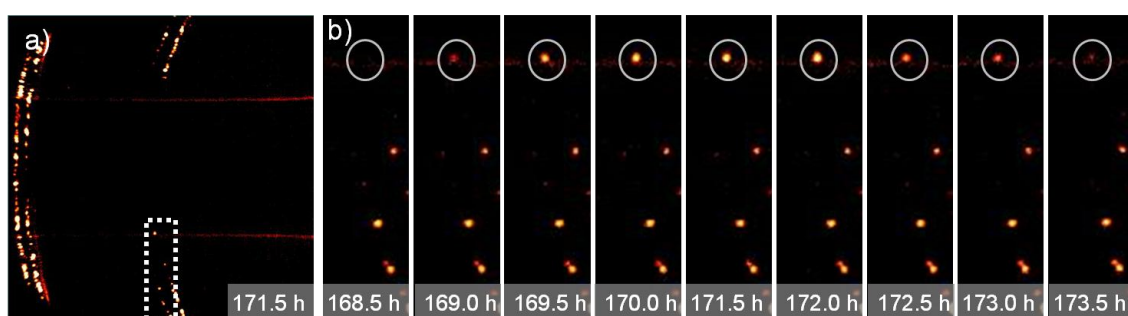


Fig. 2-7: a) 2D diffraction pattern and b) enlarged series of cutouts, for the indicated aging times at room temperature, revealing a periodic intensity increase and decrease of a Sn diffraction spot. The diffraction patterns were recorded in the detector and specimen-stage position given by the instrumental angles:  $2\Theta_0=30^\circ$ ,  $\chi=0^\circ$  and  $\Phi=0^\circ$ .

Consider Fig. 2-8 showing a sketch of a Sn grain inside the Sn film, which has a set of lattice planes in diffraction condition (in the case shown in Fig. 2-8, the diffracting lattice planes are oriented parallel to the specimen surface). The rotation of this grain around the specimen normal (vector **a** in Fig. 2-8) does not lead to a deviation from the diffraction condition (the specimen normal coincides with the diffraction vector). However, rotation of the same Sn grain around an axis which is not the diffraction vector (e.g. vector **b** in Fig. 2-8) leads to loss of the diffraction condition for the particular set of lattice planes. Thus grain rotation can bring lattice planes into and out of orientation in space compatible with the diffraction condition. Sn grain rotations

occurring upon room temperature aging can thus lead to the *abrupt* appearance and disappearance of diffraction spots on the 2D detector, as observed experimentally (see Figs. 2-3 and 2-4).

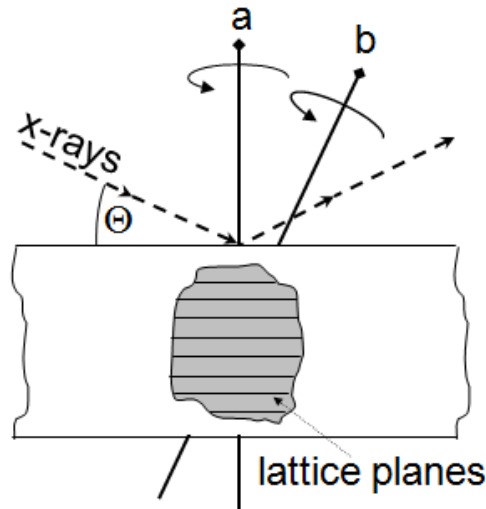


Fig. 2-8: Sketch of a Sn grain inside the Sn film with lattice planes oriented parallel to the surface, satisfying the diffraction condition. **a**, **b** indicate different axes of grain rotation. Rotation of the grain around the vector **a** (=diffracting lattice planes normal) maintains satisfaction of the diffraction condition, whereas rotation of the grain about vector **b** leads to violation of the diffraction condition, for the particular set of lattice planes considered.

Further, if a grain rotates about a certain axis which coincides with the direction of the incident beam, a migration of the diffraction spot along the intersection of the diffraction cone with the detector screen occurs (cf. Fig. 2-5): The rotation axis of the grain, which corresponds with the migrating spot shown in Fig 2-5 b), is likely close to but not exactly coincident with the incident beam, or the orientation of the rotation axis changes over time. As a consequence of such effect, the migrating diffraction spot can be observed only for a limited range of  $\gamma$  (i.e. only for a period of time), as observed in Fig. 2-5 b). Additional radial migration of the spot on the detector screen (as pertains to Fig. 2-5 b) can be due to local microstructural effects, e.g. the evolution of inhomogeneous stress states, as can be experienced during grain rotation.

If the rotation axis of the grain is not exactly the diffraction vector, but very close to it, a varying but small deviation from the ideal diffraction condition occurs during the grain rotation and thus a *cyclic* variation in intensity (slow increase and

decrease of the intensity) of the diffraction spot concerned occurs as experimentally observed in Fig 2-7.

In case grain growth and/or dissolution takes place, a *gradual* but significant change of the intensity of the corresponding diffraction spot (proportional to its (diffracting) volume) will occur, as observed in Fig. 2-6.

## ***2.5 Microstructural stability of the post-baked films***

None of the above discussed changes, concerning emergence and disappearance, variation in intensity and/or position of Sn diffraction spots, could be observed for the post-baked specimens as function of aging time at room temperature. This can be best illustrated by comparing Figs. 2-9 and 2-10: The difference of the first diffraction patterns (taken right after deposition or post-bake) and the last diffraction pattern (taken after 5 days of room temperature aging) for a particular detector and specimen-stage position was determined by using image processing software for an as-deposited specimen (Fig. 2-9) and for a post-baked specimen (Fig. 2-10). In case of the as-deposited films it can be seen that a large amount of diffraction spots had changed either their intensity and/or position (Fig. 2-9). No such changes had occurred for the post-baked specimens (Fig. 2-10). Evidently, grain rotation, grain growth and grain dissolution do not take place upon room temperature aging of the post-baked films.

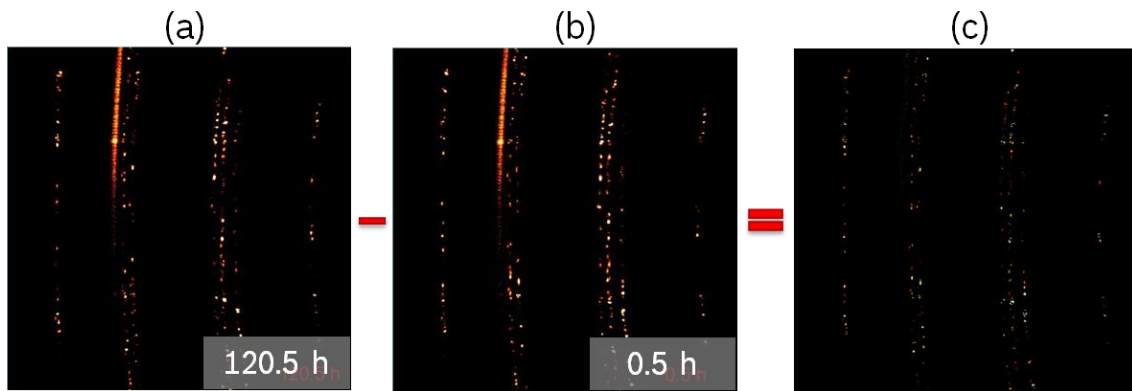


Fig. 2-9: Difference of 2D diffraction patterns recorded from an as-deposited specimen after 120.5 hours and 0.5 hours of aging at room temperature: (a)-(b)=(c). Obviously, a relatively large amount of reflection spots changed either their position and/or their intensities during the five days of aging. Diffraction patterns were recorded in the detector and specimen-stage position given by the instrumental angles:  $2\Theta_0=68^\circ$   $\chi=40^\circ$  and  $\Phi=0^\circ$ .

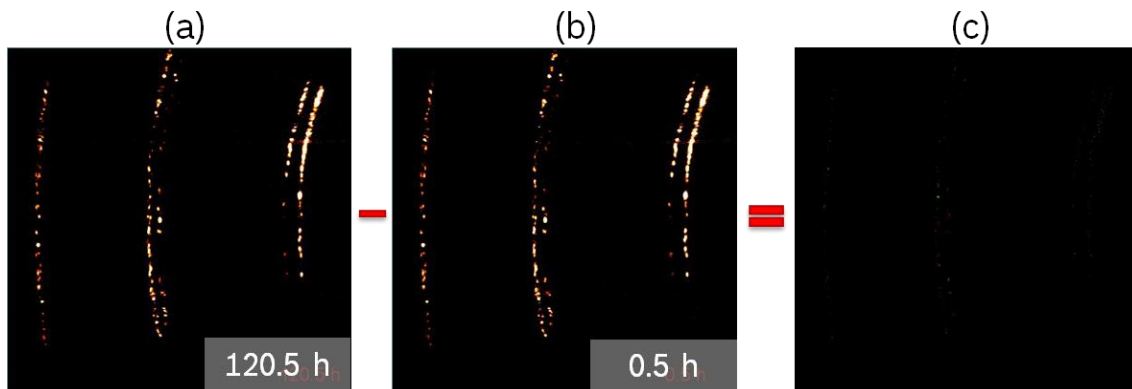


Fig. 2-10: Difference of 2D diffraction patterns recorded from a post-baked specimen after 120.5 hours and 0.5 hours of aging at room temperature: (a)-(b)=(c). No changes of the Sn diffraction spot took place which leads to the conclusion that post-baked samples hold a stable microstructure for the time of investigation. The diffraction patterns were recorded in the detector and specimen-stage position given by the instrumental angles:  $2\Theta_0=42^\circ$ ,  $\chi=60^\circ$  and  $\Phi=0^\circ$ .

## 2.6 Microstructural change and whisker formation

Whiskers can rotate while growing [23], i.e. grain rotation can take place due to (probably one-sided) attachment of Sn atoms at Sn grains. Thus it may be speculated that the phenomena observed and discussed in section 2.4 originate from whisker

grains, however, as demonstrated by the following discussion, the changes in the diffraction patterns are representative of changes in the microstructure of the films:

i) The onset of whisker growth is between the 2nd and the 3rd day of room temperature-aging (which was observed in this work by FIB surface investigations applied to similar specimens as investigated by 2D-XRD), whereas, the first distinct changes in the diffraction patterns occurred before even the end of the first day (i.e. first observation of the sudden appearance of an additional diffraction spots was made at 16.5 hours of aging). Thus, grain rotation, grain growth and grain dissolution start before whisker formation takes place.

ii) The illuminated specimen area  $G$  can be calculated according to Ref. [30]:

$$G = G_0 / \sin \theta \cdot \cos \psi \quad (1.2)$$

where  $G_0$  represents the cross-sectional area of the incident beam.  $G_0$  equals, for the setup used in this work, approximately 0.01 mm<sup>2</sup>, taking the residual divergence into account. The illuminated area  $G$  then varies between 0.06 and 0.18 mm<sup>2</sup>. Assuming a columnar, hexagonally shaped grain morphology with a lateral grain size of 3 μm (distance between facing edges), a total amount of ~2500 and 7500 Sn grains is comprised by the illuminated specimen area. Each diffraction pattern contains approximately 100 to 300 Sn diffraction spots. Thus, approximately 4% of all Sn grains in the diffracting volume are in diffracting condition. On the basis of the experimental observations by FIB, an estimated whisker and hillock density of 400 whiskers and hillocks per mm<sup>2</sup> develops, which implies that only ~24 to 72 whiskers could be protruding from the illuminated specimen area. Hence it follows that only 1 to 3 reflection spots (of the 100 to 300 diffraction spots on the recorded diffraction patterns) could be due to diffraction from a whisker (or a hillock). Because tens of suddenly appearing/disappearing and/or migrating diffraction spots occur, it is concluded that the microstructural changes in terms of grain rotation, grain growth and grain dissolution pertain to the microstructure within the films and not to the whiskers growing on top of the films.

The IMC formation of *irregular* morphology at the Cu-substrate/Sn layer interface during room temperature-aging in the as-deposited films leads to stress



gradients inside the tin film and thus diffusion of Sn atoms is induced in order to relief these stress gradients [10]. The present in-situ 2D diffraction results demonstrate that local grain rotation, grain-growth and grain-dissolution processes take place as a consequence (cf. Figs. 2-3 to 2-7).

The observation of microstructural changes as grain rotation, grain growth and grain dissolution in the Sn films can be interpreted as the result of (Coble) creep in the Sn layer. Indeed, Sobiech et al. [10] were the first to relate the presence of stress gradients in the film to the occurrence of Coble creep leading to whisker formation at locations at the surface where grain boundaries inclined with respect to the surface occur (along such oriented grain boundaries the stress driven Creep results in grain shape changes and thus is associated with processes as grain boundary sliding and grain rotation). Also recent reports in the literature with Sn based solder joints under an acting shear stress support the present observations of grain rotations as a response of stress driven creep (see e.g. Refs. [31,32])

In contrast with the as-deposited films at room temperature, Cu can diffuse into the Sn film during the post-bake treatment with a much higher rate as triggered by the elevated temperature, which leads to a more or less *planar* IMC layer [33,34]. X-ray diffraction measurements with and without controlling the penetration depth have shown that, even though an overall compressive stress state had developed inside the Sn films of post-baked samples after room temperature storage of several months, no distinct stress gradients had developed (i.e. no mass transport/creep was induced according to the above interpretation (cf. Ref. [34])). Indeed no whisker growth, and as demonstrated in this work, neither grain rotation, nor grain growth or grain dissolution take place upon room temperature aging in the post-baked films.

## ***2.7 Conclusions***

Local microstructural changes in residually stressed Sn films, as grain rotation, grain growth and grain dissolution, can be well exposed and traced as function of aging time by an in-situ two-dimensional detector X-ray diffraction technique, utilizing a rotating

anode: Diffraction spots originating from single grains emerge, disappear, migrate, increase and/or decrease their intensity.

The diffraction dynamics observed upon application of this technique to as-deposited Sn films on Cu substrates are predominated by microstructural changes and not by the whisker formation itself.

The occurrence of grain rotation, grain growth and grain dissolution lead to the following changes in the 2D diffraction patterns as experimentally revealed in this work:

- Grain rotation is generally exhibited by the *abrupt* appearance and disappearance of individual diffraction spots.
  - a) If the orientation of the axis of grain rotation is close to the of the incident beam, tangential migration of the diffraction spot, practically along the diffraction circle/ellipse, can be observed for a short period of time.
  - b) Radial migration of the diffraction spot is caused by local changes of the internal stress state.
  - c) If the orientation of the axis of grain rotation is close to that of the diffraction vector a *cyclic*, slowly occurring increase and decrease of intensity of the diffraction spot can be observed.
- Grain growth or grain dissolution is associated with the *gradual*, monotonous increase or decrease of intensity of the diffraction spot.

The exposed changes of the microstructure of the Sn films upon room temperature aging are consisted with the occurrence of (Coble) creep in a (residual) state of stress invoked by the development of intermetallic compound,  $\text{Cu}_6\text{Sn}_5$ , at the Sn layer/Cu substrate interface.

## 2.8 References

- [1] M. Schamel, C. Schopf, D. Linsler, S.T. Haag, L. Hofacker, C. Kappel, H.P. Strunk, G. Richter, *Int. J. Mater. Res.* 102, 828-836 (2011).
- [2] P.L. Key, *Proc. of the IEEE Electron. Comp. Techn. Conf.*, 155-157 (1970).
- [3] A. Baated, K.S. Kim, K. Suganuma, *J. Mater. Res.* 25, 2175-2182 (2010).
- [4] N. Zakharov, P. Werner, L. Sokolov, U. Gosele, *Physica E* 37, 148-152 (2007).
- [5] T. Fang, S. Mathew, M. Osterman, M. Fecht, *Circuit World* 33, 5-8 (2007).
- [6] G.T. Galyon, *IEEE Trans. Electron. Packag. Manuf.* 28, 94-122 (2005).
- [7] NASA, NASA Whisker Failures, <http://nepp.nasa.gov/whisker/failures/index.htm>.
- [8] K.G. Compton, A.A. Mendizza, and S.M. Arnold, *Corrosion* 7, 327 (1951).
- [9] S. M. Arnold, *Proc. of the IEEE Electron. Comp. Techn. Conf.*, 75-82 (1959).
- [10] M. Sobiech, J. Teufel, U. Welzel, E.J. Mittemeijer, W. Huegel, *J. Electron. Mater.* 40, 2300-2313 (2011).
- [11] E. Chason, N. Jadhav, W.L. Chan, L. Reinbold, K.S. Kumar. *Appl. Phys. Lett.* 92, 171901 (2008).
- [12] European-Parliament, *Official Journal of the European Union* L37 (2003).
- [13] M. Abtew, G. Selvaduray, *Mater. Sci. Eng. R-Rep.* 27, 95-141 (2000).
- [14] K.N. Tu, *Acta Metallurgica* 21, 347-354 (1973).
- [15] B. F. Dyson, T. R. Anthony, D. Turnbull, *J. Appl. Phys.* 38, 3408-3409 (1967).
- [16] B. Z. Lee, D. N. Lee *Acta Mater.* 46, 3701-3714 (1998).
- [17] M. Sobiech, C. Krueger, U. Welzel, J.Y. Wang, E.J. Mittemeijer, W. Huegel, *J. Mater. Res.* 26, 1482-1493 (2011).
- [18] G.T. Galyon, L. Palmer, *IEEE Trans. Electron. Packag. Manuf.* 28, 17-30 (2005).
- [19] M. Sobiech, M. Wohlschloegel, U. Welzel, E.J. Mittemeijer, W. Huegel, A. Seekamp, W. Liu, G.E. Ice, *Appl. Phys. Lett.* 94, 221901 (2009).
- [20] M. Sobiech, C. Krueger, U. Welzel, J.Y. Wang, E.J. Mittemeijer, W. Hugel, *J. Mater. Res.* 25, 2166-2174 (2010).
- [21] R. L. Coble *J. Appl. Phys.* 34, 1679 (1963).
- [22] J. B. N. LeBret, M.G. Norton, *J. Mater. Res.* 18, 585-593 (2002).
- [23] N. Jadhav, E. Buchovecky, E. Chason, A. Bower, *JOM* 62, 30-37 (2010).
- [24] J. Cheng, S. Chen, P. Vianco, J.C.M. Li, *Proc. of the 58th Electron. Comp. Techn. Conf.* 472-477 (2008).
- [25] A. E. Pedigo, C.A. Handwerker, J.E. Blendell *Proc. of the 58th Electron. Comp. Techn. Conf.* 1498-1504 (2008).
- [26] P. Snugovsky, S. Meschter, Z. Bagheri, E. Kosiba, M. Romansky, J. Kennedy, *J. Electron. Mater.* 41, 204-223 (2012).
- [27] E.J. Mittemeijer, U. Welzel, *Modern diffraction methods* (Wiley-VCH, Weinheim, Germany, 2012).
- [28] U. Welzel, J. Ligot, P. Lamparter, A.C. Vermeulen, E.J. Mittemeijer, *J. Appl. Crystallogr.* 38, 1-29 (2005).
- [29] B. He, *Two-Dimensional X-Ray Diffraction*. (John Wiley & Sons, Inc., Hoboken, New Jersey, 2009).
- [30] U. Welzel, M. Leoni, *J. Appl. Crystallogr.* 35, 196-206 (2002).

- [31] K. O. Lee, J.W. Morris, F. Hua, *J. Electron. Mater.* 42, 516-526 (2013).
- [32] Q. K. Zhang, Z.F. Zhang, *Scr. Mater.* 67, 289-292 (2012).
- [33] J. W. Osenbach, *J. Appl. Phys.* 106, 094903 (2009).
- [34] M. Sobiech, U. Welzel, R. Schuster, E.J. Mittemeijer, W. Huegel, A. Seekamp, V. Mueller, *Proc. of the IEEE 57th Electron. Comp. Techn. Conf.*, 192-197 (2007).

## Chapter 3

### 3 *The role of silver in mitigation of whisker formation on thin tin films*

J. Stein<sup>1,2</sup>, S. Rehm<sup>3</sup>, U. Welzel<sup>1</sup>, W. Huegel<sup>2</sup>, and E. J. Mittemeijer<sup>1,3</sup>

<sup>1</sup> Max Planck Institute for Intelligent Systems (formerly Max Planck Institute for Metals Research), Heisenbergstr. 3, 70569 Stuttgart (Germany).

<sup>2</sup> Robert Bosch GmbH, Automotive Electronics / Engineering Assembly and Interconnect Technology (AE/EAI2), Robert-Bosch-Str. 2, 71701 Schwieberdingen (Germany).

<sup>3</sup> Institute for Materials Science, University of Stuttgart, Pfaffenwaldring 55, 70569 Stuttgart (Germany).

Key words: Sn, Ag, tin whisker, whisker mitigation, X-ray diffraction.

#### 3.1 *Abstract*

The mitigating effect of alloying Sn thin films with Ag on the formation of Sn whiskers was investigated by time-resolved investigations employing X-ray diffraction for phase- and stress analyses and focused ion beam microscopy for morphological characterization of the surfaces and cross-sections of the specimens. The investigated Sn-6wt%Ag thin films were prepared by galvanic co-deposition. The results are compared with those obtained from investigation of pure Sn films and discussed with regard to current whisker-growth models. The simultaneous deposition of Sn and Ag leads to a fine grained microstructure consisting of columnar and equiaxed grains, i.e. an imperfect columnar Sn film microstructure. Isolated Ag<sub>3</sub>Sn grains are present at the Sn grain boundaries in the as-deposited films. Pronounced grain growth was observed during aging at room temperature, which provides a global stress relaxation mechanism that prevents Sn whisker growth.

## 3.2 Introduction

### 3.2.1 Whisker growth in the Sn/Cu system

Thin tin (Sn) films are frequently used in the electronics industry as surface finishes for lead-frame material (frequently composed of copper (Cu)- or iron (Fe)-based alloys) due to its favorable electronic properties, enhanced corrosion resistance and good solderability. However, it is known since the 1950s that pure Sn films are prone to whisker formation [1, 2]. Sn whiskers are filamentary [1], usually single crystalline [3, 4] metall-needles with high aspect ratio (typical diameters: 0.5-10  $\mu\text{m}$ , length up to several hundreds of micrometers [5]). Growing whiskers are able to bridge fine-pitched conductors (i.e. the pins of components) in electronic devices, which can lead to electronic failures (short circuits) [2, 6-8]. Thus, Sn whisker growth is known to be a severe reliability concern in particularly the micro-electronics industry.

Interstitial Cu diffusion into the Sn film matrix takes place during room-temperature aging of Sn films electrodeposited on Cu substrates [9, 10], leading to  $\text{Cu}_6\text{Sn}_5$  intermetallic compound (IMC) formation primarily at the Sn grain boundaries intersecting the Cu substrate [11-14]. This irregular IMC formation is connected with a volume increase, up to ~40% [15], in the lower regions of the predominantly columnar Sn film, leading to pronounced in-plane and out-of plane stress gradients [16, 17]. Due to the acting stress gradients inside the Sn film, Sn diffusion, via a Coble type creep mechanism (cf. [18]), predominantly towards the surface takes place as a response in order to relief stress, initiating and supporting Sn whisker formation and growth. [19]. Thus, whisker growth can be considered as a stress relaxation phenomenon [11, 20-23].

The appearances of the Sn whiskers, i.e. the whisker-growth forms, were found to be straight, curved, curled and/or kinked [4, 24-25]. In case the aspect ratio of a Sn protrusion on the surface is below one, i.e. its height is smaller than its diameter, the term hillock is frequently used [26-28].

### 3.2.2 Effects of alloying of Sn films on Sn whisker growth

The procedure of co-deposition of Sn and an alloying element has usually a big impact on the initial microstructure of the Sn-based film and its microstructural evolution upon aging (cf. e.g. [7,19,28-32]). Thus, the behavior of Sn alloy films can significantly deviate from pure Sn films regarding whisker growth, i.e. the alloying element may mitigate whisker growth (e.g. alloying with Pb, Bi or Ag) but it may as well enhance the whisker growth propensity and/or the (average) lengths of whiskers (e.g. alloying with Cu) [28-32].

The whisker-mitigating effect of co-depositing Sn with Pb can be explained as follows [7,19,33]. The initial, predominantly columnar microstructure of a pure Sn film changes to a more equiaxed grain morphology, with a higher amount of inclined (with respect to the surface) grain boundaries, upon the simultaneous deposition of Sn and Pb. Additionally, during room-temperature aging, the  $\text{Cu}_6\text{Sn}_5$  IMC forms in a more planar manner (since the Sn grain boundaries are occupied with Pb), which leads to a lower level of residual stress inside the Sn film and consequently to smaller stress gradients. Grain boundaries of equiaxed grains, inclined with respect to the surface, are subjected to shear stresses, due to the planar stress state of the film, which enables grain-boundary sliding. Thus, grain-shape changes induced by Coble type creep processes are accommodated globally, leading to a uniform, slight increase of the Sn film thickness. Directional Sn diffusion to a whisker root (as it appears in pure Sn films with predominantly columnar microstructure) does not take place in such films. The enhanced stress relaxation properties of Sn,Pb films with equiaxed microstructure were also demonstrated in a very recent work [34].

It has been observed that alloying thin Sn films with Ag can mitigate formation of Sn whiskers (cf. [29, 31-32, 35]) and therefore thin Sn,Ag films became a possible candidate as a lead-free coating material, for e.g. chip-components, in the micro-electronics industry. However, a fundamental understanding for the whisker resistance of Sn,Ag films lacks until today. Against this background in the present study, time resolved X-ray diffraction (XRD) phase- and stress analyses, in combination with morphological observations using focused ion beam (FIB) microscopy were carried out

to reveal the influence of Ag on the microstructural evolution of Ag alloyed, Sn thin films.

### **3.3 Experimental**

#### **3.3.1 Specimen preparation and imaging methods**

Sn,Ag and pure Sn films with a thickness of  $\sim 3 \mu\text{m}$  (thickness values validated with focused ion beam (FIB) cross-sectional analyses) on pure Cu substrates (dimensions:  $2.5 \text{ cm} \times 1.5 \text{ cm} \times 1 \text{ mm}$ ) were used. The substrates were ultrasonically cleaned in acetone and de-ionized water and surface activated (by dipping in a 10%-( $\text{H}_2\text{SO}_4$ )<sub>aq</sub> solution for a few minutes) prior to the deposition process. Sn,Ag co-deposition deposition was carried out applying an industrial electrolytes on the basis of methasulfonic acid with organic additives and dissolved metal ions by employing a laboratory setup with a current density of  $1.5 \text{ A/dm}^2$  at room temperature. The pure Sn films were produced applying the same electrolyte under the same plating conditions as done in an earlier work of our group (see [19]). Quantitative, chemical analyses of the Sn,Ag film material, dissolved from the substrate using a mixture of  $\text{HBF}_4$  and  $\text{HNO}_3$ , was performed by applying inductively coupled plasma optical emission spectrometry (ICP-OES). It was found that the films had an average composition of 6.3 wt.% Ag and 93.7 wt.% Sn. All specimens were room-temperature stored without controlling the ambient conditions.

Cross-sectional analyses carried out using a focused ion beam (FIB) microscope (FEI FIB 200), which was operated with an acceleration voltage of 30 kV and beam currents between 11 and 1000 pA for imaging and cutting. Surface observations and texture analysis were performed employing a LEO 145 VP scanning electron microscope (SEM) which is additionally equipped with an electron backscatter diffraction (EBSD)-system (TSL, EDAX, Inc.). For the texture analysis, an area of several tens of  $\mu\text{m}^2$  of the Sn,Ag film surface was scanned applying the EBSD technique. Inverse pole-figures (of these EBSD orientation-maps) were obtained using the data-analysis software OIM 4.5.



### 3.3.2 X-ray diffraction (XRD) methods

Phase analyses and diffraction-line measurements (integrated intensities of specific reflections (peak areas)) as a function of aging time at room temperature were performed using a Philips (now: PANalytical) MRD Pro diffractometer employing parallel-beam geometry and Cu  $K_{\alpha}$  radiation with a beam size of  $4 \times 4 \text{ mm}^2$  (the X-ray source was operated at 45kV/ 40 mA; for further details, see supplementary material).

The phase evolution was traced by comparing the positions of diffraction maxima in survey scans of specimens at different aging times with reference patterns of the respective phases from the literature [36]. Furthermore, integrated intensities of specific reflections (peak areas) were determined by fitting the peaks with a pseudo Voigt function. The reflections were recorded at different aging times, with the same step size and time per step, in order to achieve a time resolved result for the phase evolution. Thus, a relative (i.e. qualitative) increase or decrease of the phase volume can be measured.

Residual stress measurements [37] were performed without control of the penetration depth [38] on a “Bruker AXS D8 Discover” diffractometer using Cu- $K_{\alpha}$  radiation. The X-ray source of this diffractometer is a “TXS Superspeed” rotating anode (50 kV / 20 mA) with a filament size of  $0.1 \times 1 \text{ mm}$  point focus (for further details, see supplementary material).

Residual stresses of the film material were calculated by employing the  $\sin^2\psi$ -method [37] on the Sn 321-reflection, by assuming quasi-isotropy of the Sn film. The  $hkl$ -dependent diffraction elastic constants were derived from single crystal elastic constants [39] adopting the Neerfeld Hill model [37].

## 3.4 Results and evaluation

### 3.4.1 Initial microstructure

The composition and phase constitution of the as-deposited  $3 \mu\text{m}$  Sn,Ag films were obtained applying ICP-OES and XRD (cf. section 3.3.2). The XRD phase analysis

(Fig. 3-1, bottom) reveals that the specimens are initially composed of Cu (substrate material) and pure  $\beta$ -Sn and  $\text{Ag}_3\text{Sn}$  (film material). No pure Ag could be detected. This finding is consistent with the Sn-Ag phase diagram [40]: the solubility of Ag in Sn is negligible at room temperature and  $\text{Ag}_3\text{Sn}$  is a thermodynamically stable IMC. Note that it cannot be excluded that (some) segregation of Ag has occurred at the Sn grain boundaries (segregation of the alloying component at grain boundaries initially and/or during aging at room temperature in thin Sn alloy films has been observed before in the case of Sn,Pb films. Such a segregation of the alloying component at the Sn grain-boundaries can be responsible for an increase in grain-boundary mobility - see e.g. [19] and section 3.5). EBSD measurements reveal the presence of a Sn {110} texture of the film (see Fig. 3-2). The initial Sn and  $\text{Ag}_3\text{Sn}$  grain morphologies can be seen in the FIB image of a cross-section prepared by FIB milling (Fig. 3-3 a). A partially columnar and partially equiaxed, finely grained (typical column diameter  $<0.5\ \mu\text{m}$ ) Sn grain morphology is observed. The Sn/Sn grain boundaries are occupied with an IMC phase which appears in light grey in Fig. 3-3 a. It is known that FIB machining induces artifacts such as an occupation of the grain boundaries with a smooth thin IMC film<sup>2</sup>. However, the IMC morphology in Fig. 3-3 a) is different: the IMC grains at the Sn/Sn grain boundaries are much bigger and isolated from each other, which leads to the conclusion that  $\text{Ag}_3\text{Sn}$  precipitates occur at the Sn/Sn grain boundaries, in a more or less homogeneously distributed way (see also the sketch at the left-hand side of Fig. 3-3 a).

---

<sup>2</sup> When milling a Sn/Cu specimen with a high energy  $\text{Ga}^+$  beam, Cu atoms get removed from the substrate. Once the beam is switched off, Cu from the gas phase reacts with the freshly prepared Sn surface preferentially along the grain boundaries, which results in “highlighted” Sn/Sn grain boundaries, i.e. very thin, smooth and continuous Cu,Sn-IMC films formed along the original Sn/Sn grain boundaries (see Ref. [19]).

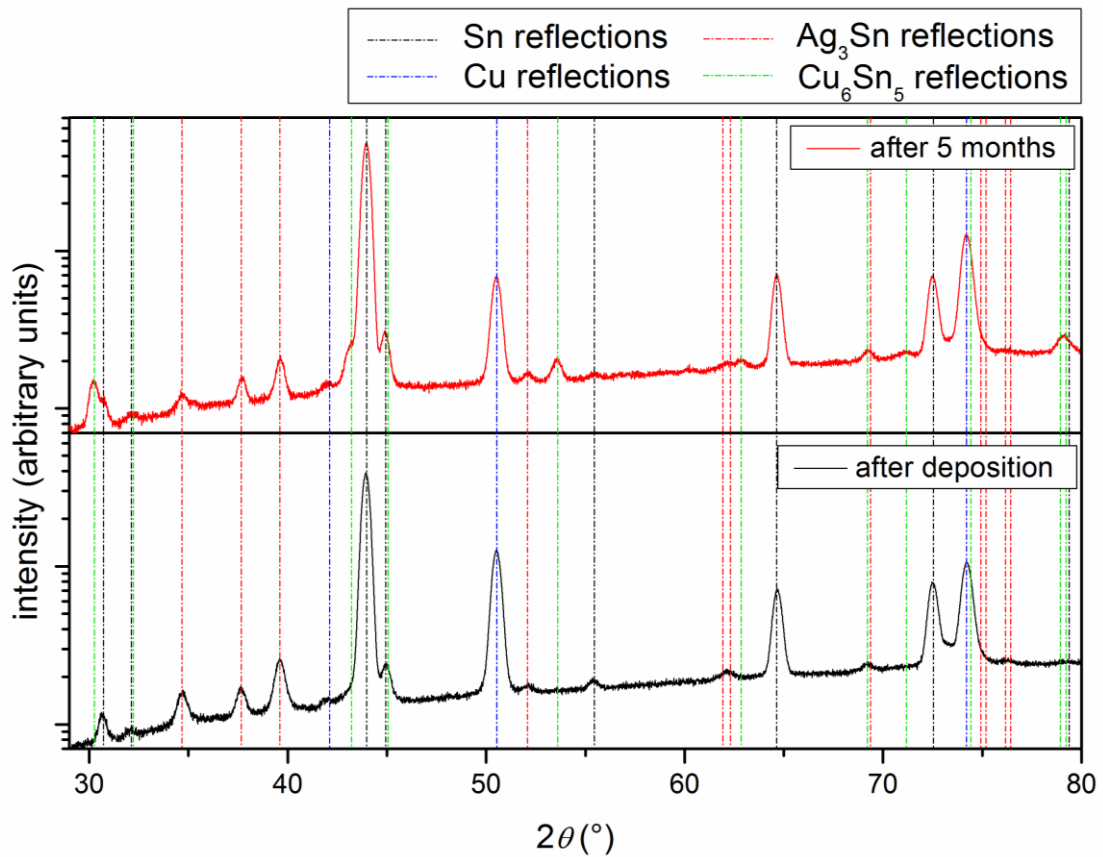
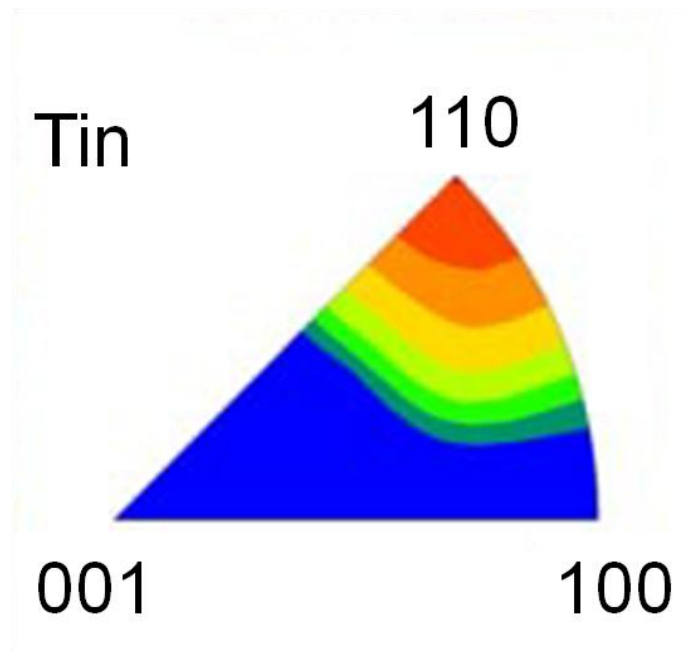


Fig. 3-1: XRD diffractograms (survey scans) recorded from Sn,Ag/Cu specimens directly after electro-deposition (bottom) and after 5 months of room temperature storage (top). All reflections can be assigned to the phases: Sn, Ag,  $\text{Cu}_6\text{Sn}_5$  and Cu, on the basis of comparison with reference patterns [31] (dashed lines).

Thus, the galvanic co-deposition of Sn and Ag leads to a different Sn film microstructure as compared to the microstructure of whiskering, predominantly columnar pure Sn films deposited on Cu substrates: The whiskering Sn/Cu specimens, as used here as reference specimens (Sn whiskers start to grow usually after a few days of aging at room temperature), are of the same type as used in an earlier work of our group (Ref. [19]), i.e. the pure Sn films were produced applying the same electrolyte (see section 3.3.2) under the same plating conditions. A representative microstructure of these Sn/Cu specimens, exhibiting predominantly columnar Sn grains (i.e. most Sn grain boundaries are oriented perpendicular normal to the specimen surface - see also Ref. [19] for a more detailed description), is shown in Fig. 3-4 a). In contrast to the Sn,Ag films, horizontally oriented grain boundaries in these pure Sn films with

predominantly columnar microstructure can only be found sporadically. The initial, lateral grain size of the pure Sn films is larger than that of the Sn,Ag films (typical lateral Sn grain sizes in the pure Sn films are between  $\sim 3 \mu\text{m}$  and  $\sim 5 \mu\text{m}$ ). The pure Sn films show a  $\{321\}$  texture [19].

The initial, rotationally symmetric, biaxial residual stress state of the Sn,Ag film (cf. section 3.4.2) is found to be of tensile nature but with a stress value close to zero ( $\sim 1.0 \pm 0.8 \text{ MPa}$ ), i.e. the film is nearly stress free.



*Fig. 3-2: Surface-normal inverse pole figure derived by applying the EBSD-technique on the surface (area of several tens of  $\mu\text{m}^2$ ) of a Sn,Ag film electro-deposited on Cu substrate indicating the orientation-distribution (i.e. texture) of the Sn grains parallel to the surface. Red to yellow colors indicates a high density of Sn grains and blue to green colors indicates a low density of grains. It can be seen that most Sn grains have an orientation close to one with a  $\{110\}$  plane parallel to the surface.*

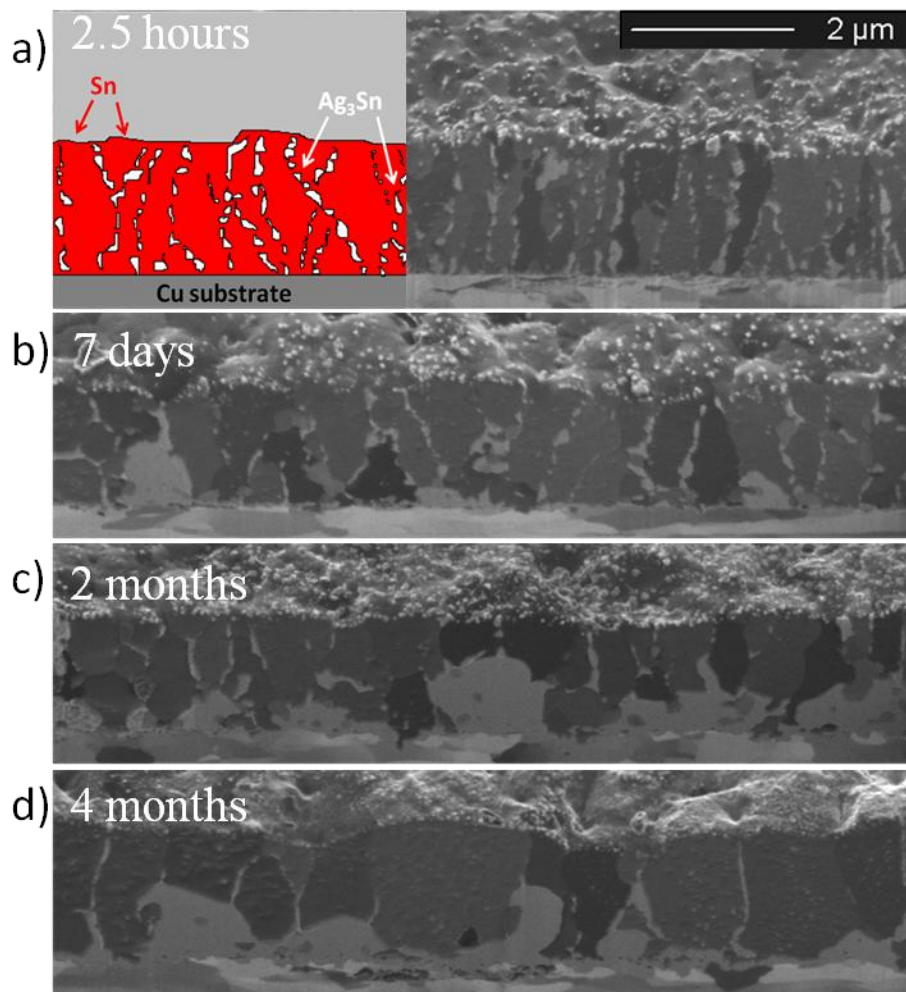


*Fig. 3-3: FIB images of cross-sections prepared applying FIB milling at different aging times of Sn,Ag/Cu specimens. A fine-grained Sn film microstructure, with isolated  $\text{Ag}_3\text{Sn}$  grains, along the grain boundaries, develops upon electro-deposition of the Sn,Ag film (see also the sketch in the top image). Irregular  $\text{Cu}_6\text{Sn}_5$  formation takes place in the Sn film at the film/substrate interface during room temperature storage. Extensive (lateral) Sn grain growth results in a coarsened microstructure after pronounced aging of the specimen at room temperature.*

### 3.4.2 Microstructural evolution during room temperature aging

The Sn,Ag films of this study do not show any Sn whisker or hillock formation during room temperature aging, even after several months of storage. The evolution of the Sn,Ag film microstructure during room temperature storage is revealed by Figs. 3-3 b) to d).  $\text{Cu}_6\text{Sn}_5$  forms at the Sn/Cu interface during aging of Sn/Cu couples at room temperature [11-14]. IMC's, such as  $\text{Cu}_6\text{Sn}_5$  (and also  $\text{Ag}_3\text{Sn}$ ), appear in light grey (in contrast to the dark-grey Sn grains) in the FIB cross-sections. Consequently, the growth

of the  $\text{Cu}_6\text{Sn}_5$  can be observed and tracked in Fig. 3-3 (i.e. an increase of the light grey area, rising from the Sn/Cu interface, can be observed). The growth of  $\text{Cu}_6\text{Sn}_5$  is consistent with the emergence of additional peaks in the XRD survey diffractogram, recorded from a Sn,Ag/Cu specimen after 5 months of storage (see the green marked reflections in Fig. 3-1, top). The kinetics of the growth of  $\text{Cu}_6\text{Sn}_5$  can be characterized by XRD peak-area measurements of a  $\text{Cu}_6\text{Sn}_5$  reflection during room temperature aging (see Fig. 3-5), provided no texture changes occur (the  $\text{Cu}_6\text{Sn}_5$  phase grows indeed nearly untextured, which was checked by XRD pole-figure measurements at several aging stages).

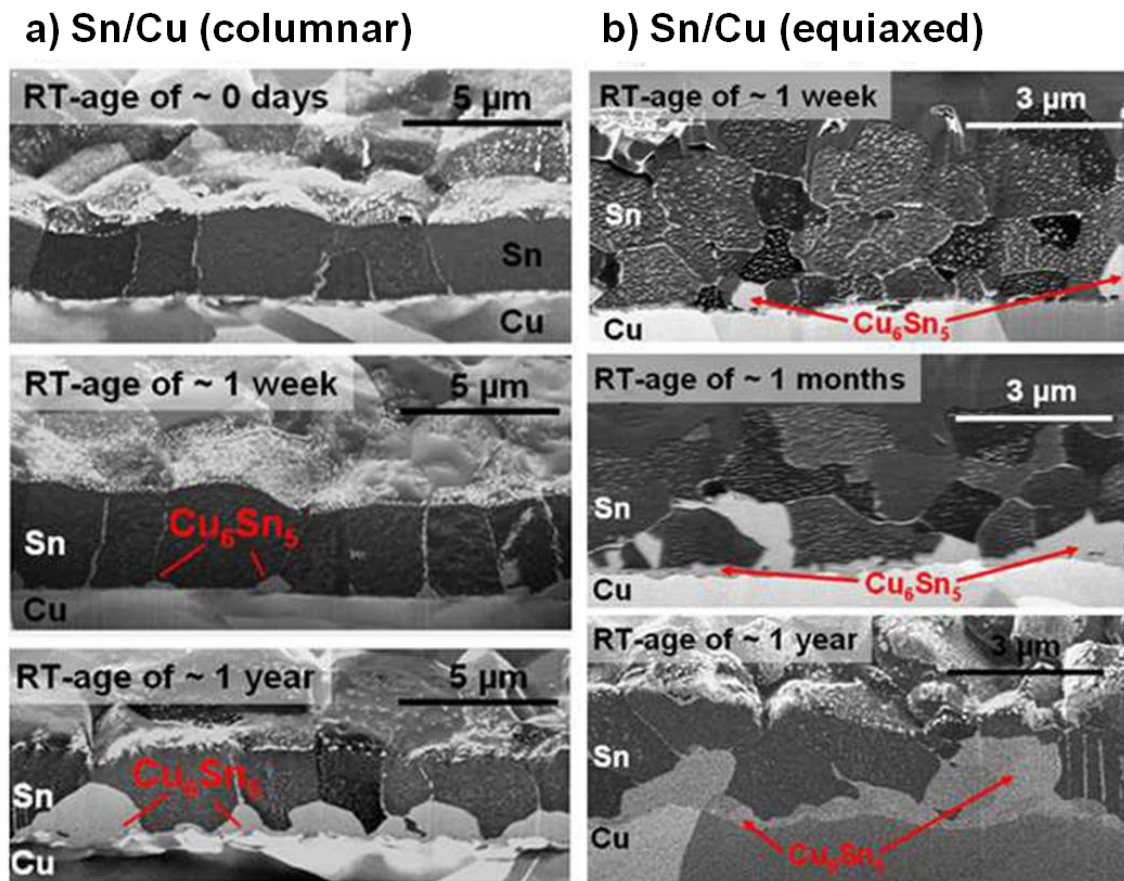


Fig. 3-4: FIB images showing microstructures of pure Sn/Cu specimens as function of room temperature storage time for a film with a) predominantly columnar Sn grain morphology (this type is used as reference specimens in this work) and b) equiaxed Sn grain morphology. Images were taken from a previous work of our group [19].

Diffusion controlled growth is often associated with a parabolic dependence on time of layer thickness or phase volume [41]. A plot of the squared value of the

integrated intensity (peak area) of the 24-1 reflection of  $\text{Cu}_6\text{Sn}_5$  vs. aging time at room temperature is shown in Fig. 3-5. Apparently, the growth behavior of  $\text{Cu}_6\text{Sn}_5$  can be divided into two stages: After an initial stage of relatively fast growth, a second stage occurs that shows parabolic growth. This finding can be explained with reference to the FIB images shown in Fig. 3-3:  $\text{Cu}_6\text{Sn}_5$  forms with an irregular microstructure, i.e. preferentially along the Sn/Sn grain boundaries intersecting the Cu substrate, during the first days of storage. At the same time also a thin planar layer of IMC forms at the Sn/Cu interface. Once this thin layer is fully closed, further  $\text{Cu}_6\text{Sn}_5$  formation is slowed down as Cu diffusion in the IMC is hindered as compared to diffusion in Sn. Thus, a second (less fast) growth stage is reached (cf. Fig. 3-3 b and Fig. 3-5) likely controlled by diffusion of Cu through the IMC. (The scatter of the data points in Fig. 3-5, owing to limited counting statistical accuracy corresponding to the restricted time of each measurement, appears relatively pronounced since the *square* of the integrated intensity of the reflection has been plotted in this graph).

Similar peak-area measurements of the same  $\text{Cu}_6\text{Sn}_5$  reflection were carried out for a pure Sn/Cu specimen of the same film thickness. These results are also shown in Fig. 3-5. Since the growth morphology of  $\text{Cu}_6\text{Sn}_5$  is similar (i.e. growth starting from the film/substrate interface towards the surface, mainly along the Sn/Sn grain boundaries and also along the Sn/Cu interface, see Fig. 3-4) in both, the pure Sn/Cu and the Sn,Ag/Cu specimens, differences in absorption of incident and diffracted X-rays, due to a possible positional difference of the  $\text{Cu}_6\text{Sn}_5$  phase inside the films, can be neglected and it thus follows from Fig. 3-5 that equal amounts of  $\text{Cu}_6\text{Sn}_5$  form in both films during aging at room temperature.

It is clearly visible in Fig. 3-3 that, besides  $\text{Cu}_6\text{Sn}_5$  growth, extensive lateral Sn grain growth occurs upon aging at room-temperature. Further, the initially more or less homogeneous distribution of  $\text{Ag}_3\text{Sn}$  IMC grains along the Sn/Sn grain boundaries (cf. section 3.4.1), is not maintained at later stages of aging (cf. Figs. 3-3 c and d): A change of location of the  $\text{Ag}_3\text{Sn}$  grains (at the Sn grain boundaries, cf. section 3.4.1) to the bottom part of the Sn layer, as a consequence of the extensive lateral Sn grain growth (see discussion in next section), has occurred, where the  $\text{Ag}_3\text{Sn}$  and the  $\text{Cu}_6\text{Sn}_5$  IMCs then agglomerate upon aging at room temperature.

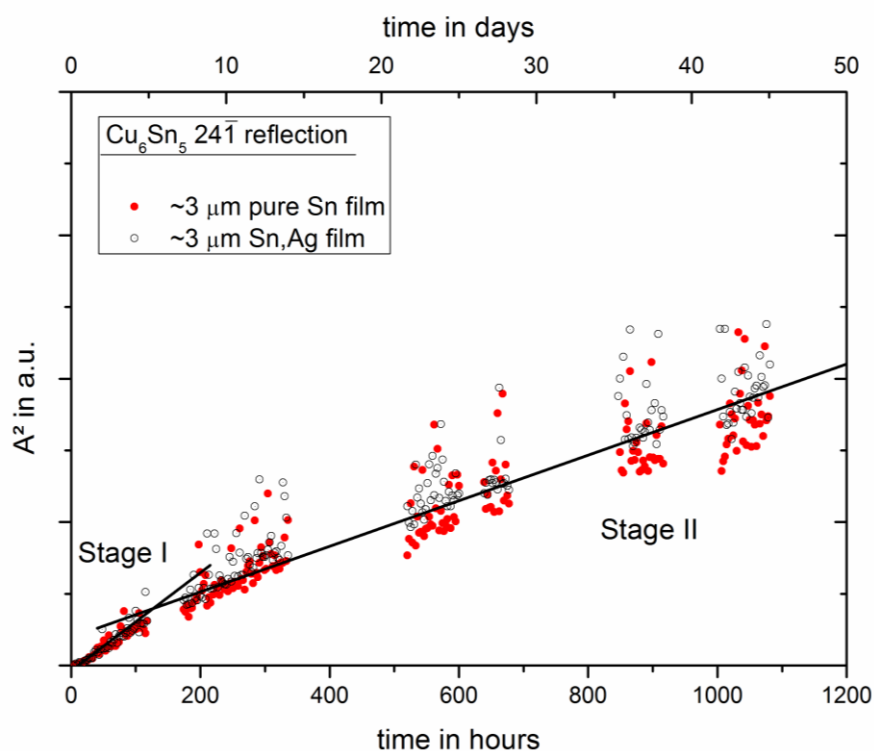


Fig. 3-5: The squared XRD integrated intensity (peak area  $A$ ), as recorded for the  $\text{Cu}_6\text{Sn}_5$  24-1 reflection of  $\sim 3 \mu\text{m}$  pure Sn/Cu (red dots) and  $\sim 3 \mu\text{m}$  Sn,Ag/Cu (black open dots) thin film specimens during storage at room temperature. The growth behavior can be divided into two stages. Stage I: Rapid growth due to irregular  $\text{Cu}_6\text{Sn}_5$  formation, especially at the Sn grain boundaries intersecting the Cu substrate. Stage II: A closed, planar layer at the film/substrate interface has formed, further  $\text{Cu}_6\text{Sn}_5$  formation is slowed down as Cu diffusion in the IMC is hindered as compared to diffusion in Sn.

The occurrence of a relocation process of the  $\text{Ag}_3\text{Sn}$  phase is consistent with the integrated intensity (peak-area) measurements of three different  $\text{Ag}_3\text{Sn}$  reflections (i.e. the  $\text{Ag}_3\text{Sn}$  201, 020 and 211 reflections) as function of room temperature storage time (see Fig. 3-6): an overall decrease of peak-area is observed upon aging for all three reflections due to an increase of absorption of the incident and diffracted X-rays. (The rapid increase of the peak-area of the  $\text{Ag}_3\text{Sn}$  020 reflection and the rapid decreases of the peak-areas of the  $\text{Ag}_3\text{Sn}$  201 and 211 reflections during only the first day of aging are ascribed to a change of crystallographic texture).



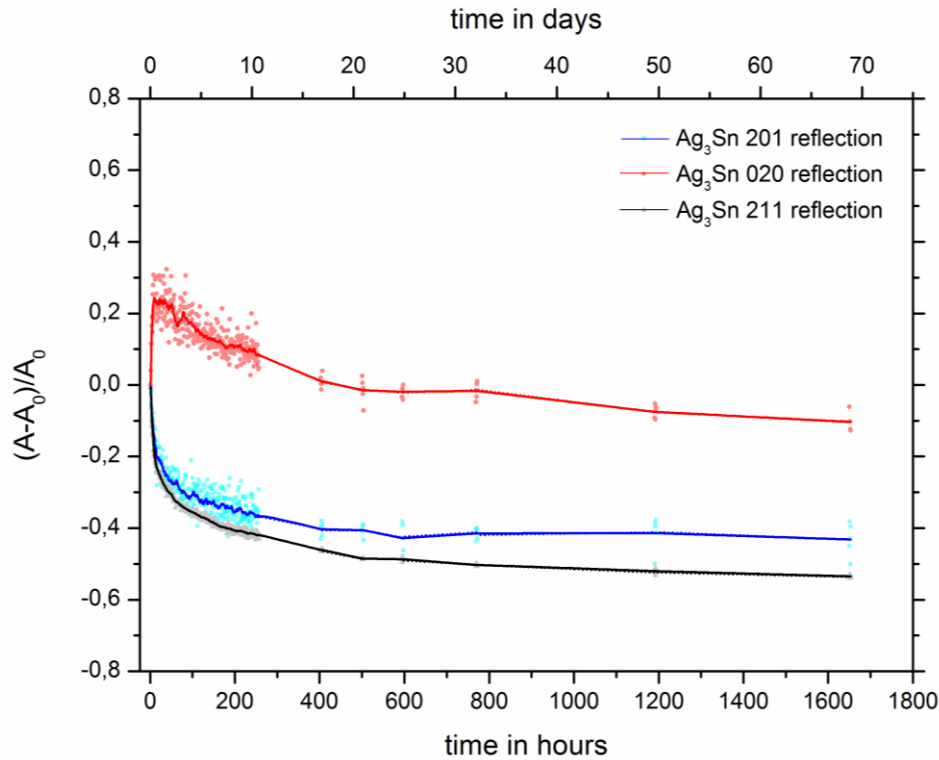
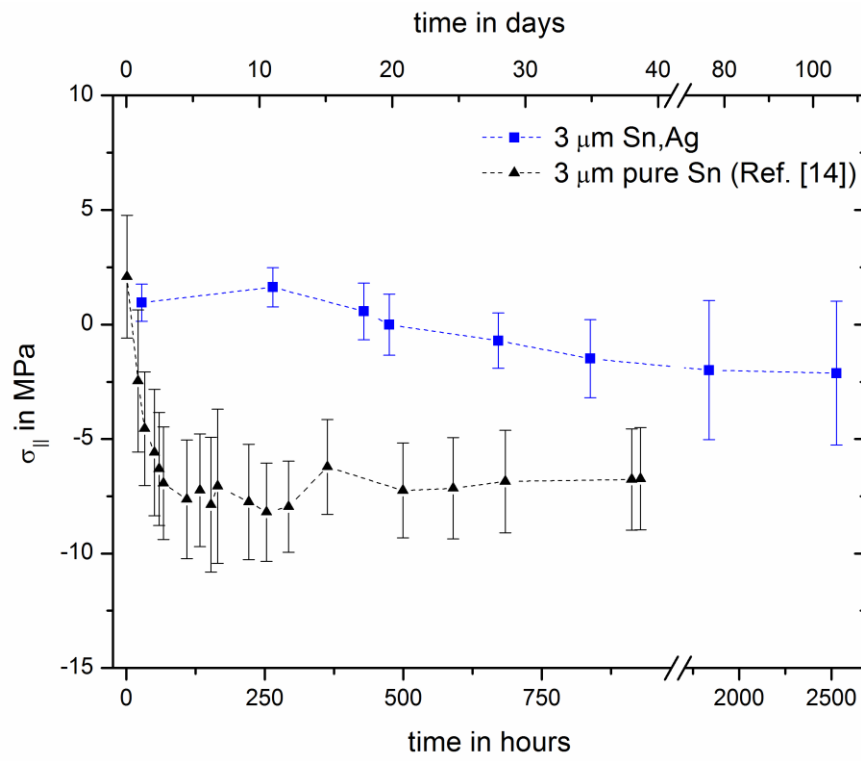


Fig. 3-6: Time-resolved XRD integrated intensity (peak area  $A$ ) measurements for three  $\text{Ag}_3\text{Sn}$  reflections, as measured for a  $\text{Sn,Ag/Cu}$  specimen during storage at room temperature ( $A_0$  represents the initial, measured peak area). An overall decrease of peak-area is observed upon aging for all three reflections (The rapid increase of the peak-area of the  $\text{Ag}_3\text{Sn}$  020 reflection and the rapid decreases of the peak-areas of the  $\text{Ag}_3\text{Sn}$  201 and 211 reflections during only the first day of aging are ascribed to a change of crystallographic texture)

For the case of a transport of the  $\text{Ag}_3\text{Sn}$  phase to lower regions of the Sn film, the maximum possible  $\text{Ag}_3\text{Sn}$  intensity decrease due to the correspondingly increased absorption of the diffracted X-rays was calculated by considering two limiting cases: (i) an initially homogeneous distribution of  $\text{Ag}_3\text{Sn}$  inside the Sn film (representing the initial stage) and (ii) a planar layer of (the same amount of)  $\text{Ag}_3\text{Sn}$  at the bottom of the Sn film (representing a stage of pronounced aging at room-temperature - see Appendix). It was found that an  $\text{Ag}_3\text{Sn}$  intensity decrease up to  $\sim 85\%$  can be explained by such an absorption effect. The smaller magnitude of the experimentally observed intensity change ( $\sim 35\%$ ) can then be understood recognizing that after pronounced aging (see Fig. 3-3 d),  $\text{Ag}_3\text{Sn}$  cannot be present as a genuinely planar layer at the Sn/Cu interface as considered in the calculation, already only owing to the presence of the irregularly grown  $\text{Cu}_6\text{Sn}_5$  IMC. Also, in rare cases, some  $\text{Ag}_3\text{Sn}$  grains can be detected at the

surface (revealed by EBSD phase maps taken from the Sn surface) after pronounced aging times.



*Fig. 3-7: The rotationally symmetric, biaxial stress parallel to the surface ( $\sigma_{||}$ ) in the Sn film as a function of aging time at room temperature as measured for the  $\sim 3 \mu\text{m}$  pure Sn (black triangles, data taken from Ref. [19]) and Sn,Ag (blue rectangles) films electroplated on Cu substrates.*

Time resolved XRD stress measurements on Sn reflections of the Sn,Ag film reveal that in the Sn film initially present slightly tensile stress parallel to the surface ( $\sim 1.0 \pm 0.8$  MPa, cf. section 3.4.1) transforms to a slightly compressive stress parallel to the surface ( $\sim -2.1 \pm 3.1$  MPa) after approximately 2500 hours of aging (see Fig. 3-7). A pronounced built up of compressive stress, as occurring in pure Sn films on Cu (see black triangles in Fig. 3-7, see also Ref. [19]) evidently does not occur for the Sn,Ag films studied (discussion in next section).

### 3.5 General discussion

The simultaneous deposition of Sn and Ag leads to the development of a fine-grained Sn microstructure with partially columnar and partially equiaxed grains, as well as  $\text{Ag}_3\text{Sn}$  precipitates distributed homogeneously along Sn grain boundaries (cf. section 3.4.1). Upon room temperature storage,  $\text{Cu}_6\text{Sn}_5$  formation takes place in the Sn,Ag films, at the film/substrate interface, with irregular morphology, (see Figs. 3-1 and 3-3) with an equal rate of formation as observed for (whiskering) pure Sn/Cu specimens (see Fig. 3-5 and discussion in section 3.4.2). In contrast with Sn,Pb films, where a more planar IMC layer at the Sn/Cu interface develops (see Ref. [19]), the morphology of the developing  $\text{Cu}_6\text{Sn}_5$  phase appears not to be influenced by the presence of the alloying element inside the Sn,Ag films. Irregular formation of  $\text{Cu}_6\text{Sn}_5$  is known to be responsible in pure Sn films (with columnar microstructure, see Fig. 3-4 a)) for the build-up of an overall compressive planar stress state (see black triangles in Fig. 3-7) in association with the development of a negative stress-depth gradient providing the driving force for Sn diffusion, from the bottom to the top of the layer, along grain boundaries, thus initiating and supporting Sn whisker formation and growth on the surface of the Sn film at locations at the surface where grain boundaries inclined with respect to the surface occur [19]. Yet, Sn whiskers are not found on the surface of the Sn,Ag films of the present study, even after pronounced aging times. This can be understood as follows.

Even though irregular  $\text{Cu}_6\text{Sn}_5$  formation in Sn,Ag/Cu specimens takes place during storage of the specimens at room temperature, built up of a (steady, pronounced) compressive stress state does not take place (see Fig. 3-7) and thus no development of a steady, pronounced (negative) stress-depth gradient occurs. The absence of distinct, steady (negative) stress-gradient development is the consequence of the Sn grain morphology. In the initial microstructure of the as-deposited Sn,Ag films, next to columnar grains, a substantial fraction of equiaxed grains occurs. Equiaxed Sn film microstructures are much less prone to the formation of Sn whiskers as compared to columnar Sn film microstructures. Inclined (with respect to the specimen surface) grain boundaries of equiaxed grains in the film are subjected to shear stresses, due to the macroscopic *planar* state of stress, and stress relaxation then can take place by grain-

shape changes due to Sn diffusion along their grain boundaries, i.e. Coble creep, at many sites inside the Sn film, in association with grain-boundary sliding as a natural mechanism to maintain the massive nature of the specimen upon this Coble-type creep [19, 43].

These dynamic processes in the microstructure, take place globally, i.e. at many places within the Sn,Ag film. In the overwhelmingly columnar pure Sn films, stress relief can only occur locally at a few places where at the surface of the film inclined grain boundaries occur, which thus give rise to whisker formation at these isolated locations.

The positional change of the  $\text{Ag}_3\text{Sn}$  phase (predominantly) towards lower regions of Sn,Ag films of the present study can be explained by taking into account that the above described stress relaxation and grain-shape change is accompanied by grain coarsening (see Fig. 3-3): extensive Sn grain growth of mainly equiaxed grains at the surface, with inclined grain boundaries with respect to the surface takes place upon aging at room temperature. Such (pronounced) grain coarsening can take place/is supported by i) a high driving force due to the presence of a high amount of grain boundary area and/or ii) high grain boundary mobility. It was already shown in a previous work by our group (Ref. [19]) that the microstructure of a pure Sn film with equiaxed grains (and thus with high driving force for grain coarsening) does not show (significant) grain coarsening after 1 month (only a slight increase of the lateral Sn grain sizes can be seen after very long aging times at room temperature, see FIB-image in Fig. 3-4 b) after 1 year of aging). Since pronounced grain coarsening of the Sn grains in the Sn,Ag films takes place already during the first week of aging at room temperature and continues during the first months of aging (see Fig. 3-3), we conclude that (not only the presence of a high driving force but also) an enhanced Sn grain-boundary mobility in Sn,Ag films must be responsible for the observation of grain coarsening.

The segregation of Ag at the Sn grain boundaries in the deposited films, can be responsible for this increase in grain-boundary mobility, similar as observed for Pb in Sn,Pb films [19].

### 3.6 Conclusions

The electro co-deposition of Sn and Ag on Cu substrates leads to an as-deposited film microstructure with partially columnar and partially equiaxed Sn grains and isolated  $\text{Ag}_3\text{Sn}$  precipitates along the Sn/Sn grain boundaries.

The microstructural changes upon room temperature storage can be summarized as follows:

- i)  $\text{Cu}_6\text{Sn}_5$  formation takes place at the film/substrate interface in an irregular manner with a similar formation rate as observed in whiskering pure Sn/Cu specimens. However, Sn whisker growth does not occur on top of the Sn,Ag films studied.
- ii) Inclined (with respect to the specimen surface) grain boundaries of equiaxed grains are found at many locations within the as-deposited Sn,Ag film. These inclined grain boundaries are subjected to shear stresses, due to the macroscopic planar state of stress, which leads to a *global* stress relaxation mechanism since grain-shape changes due to Sn diffusion along their grain boundaries, i.e. Coble creep, in association with grain-boundary sliding (a natural mechanism to maintain the massive nature of the specimen upon this Coble-type creep) can take place at many sites within the film. This is in contrast to pure Sn films with overwhelmingly columnar microstructures where stress relaxation can only take place *locally* (i.e. at a few locations) at the surface where inclined grain boundaries occur, which results in Sn whisker growth.
- iii) The grain-shape change and the grain-boundary sliding is accompanied with coarsening (extensive lateral grain growth), in contrast with pure Sn films. This is a consequence of enhanced grain-boundary mobility due to segregated Ag.
- iv) A side effect of the extensive lateral Sn grain growth is that the initial, more or less homogeneous, distribution of  $\text{Ag}_3\text{Sn}$  along the Sn grain boundaries cannot be maintained upon aging. The extensive Sn grain growth of mainly equiaxed grains at the surface, with inclined grain boundaries with respect to the surface,

is connected with grain-boundary movement of these inclined grain boundaries towards the Sn/Cu interface. It follows that a relocation of the Ag<sub>3</sub>Sn phase, situated along the grain boundaries, towards lower regions of the Sn,Ag films, occurs.

### 3.7 Appendix

For the assessment of the intensity decrease of Ag<sub>3</sub>Sn reflections due to absorption of the incident and diffracted X-rays, two limiting cases are considered.

For case (i), a completely homogeneous distribution of the Ag<sub>3</sub>Sn phase in the as-deposited Sn film is assumed. The integrated intensity (of a Ag<sub>3</sub>Sn reflection)  $I^{(i)}$  for case (i) is then given by

$$I^{(i)} = I_0 \cdot \int_0^{d_0} dz \cdot \rho_0 \cdot \exp\left(-\frac{z}{\tau_{Sn}}\right) \quad (3.1)$$

where  $I_0$  is the incident intensity,  $d_0$  is the Sn film thickness,  $z$  is the depth beneath the surface of the Sn film and  $dz \cdot \rho_0$  is the fraction of intensity diffracted by a depth element  $dz$  ( $\rho_0$  is proportional with the volume fraction of Ag<sub>3</sub>Sn) [42].

$\tau$  is given by

$$\tau_{Sn} = \frac{\sin \Theta \cdot \cos \psi}{2 \cdot \mu_{Sn}} \quad (3.2)$$

$\tau$  is a function of the linear absorption coefficient  $\mu$  which can be obtained from the NIST physical constants database [44] (for the sake of simplicity, considering that the layer consists predominantly of Sn, the linear absorption coefficient of pure Sn has been used).

For case (ii), the same amount of phase Ag<sub>3</sub>Sn as for case (i) now is present as a planar layer of Ag<sub>3</sub>Sn at the bottom of the Sn film. The integrated intensity  $I^{(ii)}$  is now given by

$$I^{(ii)} = I_0 \cdot \exp\left(-\frac{d_0 - d_{Ag_3Sn}}{\tau_{Sn}}\right) \cdot \int_0^{d_{Ag_3Sn}} dz \cdot \rho \cdot \exp\left(-\frac{z}{\tau_{Ag_3Sn}}\right) \quad (3.3)$$

with

$$\rho = \rho_0 \cdot \frac{d_0}{d_{Ag_3Sn}}. \quad (3.4)$$

Finally the ratio  $R$  of the integrated diffracted intensities for cases (i) and (ii) by is obtained from Eqs. (3.1) and (3.3):

$$R = \frac{I^{(i)}}{I^{(ii)}} = \frac{\tau_{Sn} \cdot \left(1 - \exp\left(\frac{-d_0}{\tau_{Sn}}\right)\right)}{\exp\left(-\frac{d_0 - d_{Ag_3Sn}}{\tau_{Sn}}\right) \cdot \frac{d_0}{d_{Ag_3Sn}} \cdot \tau_{Ag_3Sn} \cdot \left(1 - \exp\left(\frac{-d_{Ag_3Sn}}{\tau_{Ag_3Sn}}\right)\right)} \quad (3.5)$$

Taking  $d_0$  and  $d_{Ag_3Sn}$  as 3  $\mu\text{m}$  and 0.13  $\mu\text{m}$  (calculated on the basis of the film composition), respectively, an intensity decrease up to ~85 % would occur upon concentrating all  $Ag_3Sn$ , originally distributed homogeneously, at the bottom of the film.

### 3.8 Supplementary material

The “*Philips (now: PANalytical) MRD Pro*” diffractometer was employed with a parallel-beam geometry and Cu  $K_\alpha$  radiation with a beam size of 4×4 mm<sup>2</sup> (the X-ray source was operated at 45kV/ 40 mA). The diffractometer was equipped with a conventional, sealed Cu tube (operated at 45kV/ 40 mA) as X-ray source, a polycapillary X-ray lens, needed for parallelization of the X-rays, an Eulerian cradle (four-circle goniometer) which allows rotating and tilting of the specimen, a parallel foils collimator and a flat graphite monochromator as secondary optics to select  $K_\alpha$  radiation, as well as a proportional counter. The diffractometer was operated with the Philips data collector software.

The “*Bruker AXS D8 Discover*” diffractometer was applied using Cu- $K_\alpha$  radiation. The X-ray source of this diffractometer is a “TXS Superspeed” rotating anode

(50 kV / 20 mA) with a filament size of  $0.1 \times 1$  mm point focus. A 2D- collimating mirror (“Xenocs Fox 2D”) is used for parallelizing as well as for monochromatization of the X-rays. The diffractometer is additionally equipped with a “Huber” 1/4-circle Eulerian cradle, which allows variations of all Eulerian angles. The diffracted X-rays were detected using an energy dispersive detector (“Bruker AXS Sol-X”) with a geometrical acceptance window of approximately  $4 \times 15$  mm<sup>2</sup>. Specimen alignment was performed with help of a justified laser and video camera system. The diffractometer chamber is air-conditioned in order to maintain a constant temperature ( $\approx 22$  °C). A spinner was used which rotates the specimen around the specimen normal to enhance crystallite statistics. The diffractometer was operated using the Bruker “XRD commander” software.



### 3.9 References

- [1] K.G. Compton, A.A. Mendizza, S.M. Arnold, *Corrosion* 7, 327-334 (1951).
- [2] G.T. Galyon, *IEEE Trans. Electron. Packag. Manuf.* 28, 94-122 (2005).
- [3] C. Herring, J.K. Galt, *Phys. Rev.* 85, 1060-1061 (1952).
- [4] S. Donald, M. Joseph, R.P. Grant, B. McKenzie, W.G. Yelton, *Met. Mat. Trans* 44A, 1485-1496 (2013).
- [5] V. K. Glazunova, N. T. Kudryavtsev, *Zh. Prikl. Khim.* 36, 543-550 (1963).
- [6] NASA, Whisker Failures: <http://nepp.nasa.gov/whisker/failures/index.htm>.
- [7] W.J. Boettinger, C.E. Johnson, L.A. Bendersky, K.W. Moon, M.E. Williams, G.R. Stafford, *Acta Mater.* 53, 5033-5050 (2005).
- [8] Y. Fukuda, M. Osterman, M. Pecht, *Electron. Pack. Manuf. IEEE* 30, 36-40 (2007).
- [9] K.N. Tu, R.D. Thompson, *Acta Metall.* 30, 947-952 (1982).
- [10] B.F. Dyson, T.R. Anthony, D. Turnbull, *J. Appl. Phys.* 38, 3408 (1967).
- [11] B.Z. Lee, D.N. Lee, *Acta Mater.* 46, 3701-3714 (1998).
- [12] M. Sobiech, C. Krueger, U. Welzel, J.Y. Wang, E.J. Mittemeijer, W. Huegel, *J. Mater. Res.* 26, 1482-1493 (2011).
- [13] K.S. Kumar, *J. Mater. Res.* 23, 2916–2934 (2008).
- [14] E. Chason, N. Jadhav, W. L. Chan, L. Reinbold, K. S. Kumar, *Appl. Phys. Lett.* 92, 171901 (2008).
- [15] G.T. Galyon, L. Palmer, *IEEE Trans. Electron. Packag. Manuf.* 28, 17-30 (2005).
- [16] M. Sobiech, M. Wohlschloegel, U. Welzel, E.J. Mittemeijer, W. Huegel, A. Seekamp, W. Liu, G.E. Ice, *Appl. Phys. Lett.* 94, 221901 (2009).
- [17] M. Sobiech, U. Welzel, E.J. Mittemeijer, W. Huegel, A. Seekamp, *Appl. Phys. Lett.* 93, 011906 (2008).
- [18] R.L. Coble, *J. Appl. Phys.* 34, 1679 (1963).
- [19] M. Sobiech, J. Teufel, U. Welzel, E.J. Mittemeijer, W. Huegel, *J. Electron. Mater.* 40, 2300-2313 (2011).
- [20] R.R. Hasiguti, *Acta Metall.* 3, 200-201 (1955).
- [21] U. Lindborg, *Acta Metall.* 24, 181-186 (1976).
- [22] W.J. Choi, T.Y. Lee, K.N. Tu, N. Tamura, R.S. Celestre, A.A. MacDowell, Y.Y. Bong, L. Nguyen, *Acta. Mater.* 51, 6253–6261 (2003).
- [23] M.E. Williams, K.-W. Moon, W.J. Boettinger, D. Josell, A.D. Deal, *J. Electron. Mater.* 36, 214-219 (2007).
- [24] S.E. Koonce, S.M. Arnold, *J. Appl. Phys.* 25, 134-135 (1954).
- [25] J.B. LeBret, M.G. Norton, *J. Mater. Res.* 18, 585-293 (2003).
- [26] N. Jadhav, E. Buchovecky, E. Chason, A. Bower, *JOM* 62, 30-37 (2010).
- [27] J. Cheng, S. Chen, P. Vianco, J.C.M. Li, *Proc. of the 58th Electronic Components & Technology Conference*, 472-477 (2008).
- [28] A.E. Pedigo, C.A. Handwerker, J.E. Blendell, *Proc. of the 58th Electron. Comp. Techn. Conf.*, 1498-1504 (2008).
- [29] A. Baated, K. Hamasaki, S.S. Kim, K.S. Kim, K. Sugauma, *J. Electron. Mater.* 40, 2278-2289 (2011).

- [30] P. Sarabol, A.E. Pedigo, P. Su, J.E. Blendell, C.A. Handwerker, IEEE Trans. Electron. Packag. Manuf. 33, 159-164 (2010).
- [31] I. Yanada, IPC Printed Circ. Expo '98, Proc. of the Techn. Conf., 1-7 (1998).
- [32] R. Schetty, W. Sepp, Proc. of the 11th Electron. Packag. Techn.Conf., 225-234 (2009).
- [33] S.M. Arnold, Proceedings of the IEEE Electro. Comp. Techn.Conf., 75-82 (1959).
- [34] N. Jadhav, J. Wasserman, F. Pei, E. Chason, J. Electron. Mater. 41, 588-595 (2012).
- [35] T. Asai, T. Kiga, Y. Taniguchi, H. Morikawa, K. Sumiyama, J. Jpn. Inst. Met. 73, 823-832 (2009).
- [36] PDF-2, International Center for Diffraction Data (ICDD) Version 2.1 (2002).
- [37] U. Welzel, J. Ligot, P. Lamparter, A.C. Vermeulen, E.J. Mittemeijer, J. Appl. Crystallogr. 38, 1-29 (2005).
- [38] A. Kumar, U. Welzel, E.J. Mittemeijer, J. Appl. Crystallogr. 39, 633-646 (2006).
- [39] C.J. Smithells, E.A. Brandes, Metal Reference Book (Butterworths London, 1976), pp. 975-980.
- [40] I. Karakaya, W.T. Thompson, Bull. Alloy Phase Diagrams 8, 340-347 (1987).
- [41] P.G. Shewmon, Diffusion in Solids (John Wiley & Sons, McGraw-Hill, 2010), pp. 246.
- [42] R. Delhez, Th.H. de Keijser, E.J. Mittemeijer, Surf. Eng. 3, 331-342 (1987).
- [43] E. Sandnes, M. E. Williams, M. D. Vaudin. G.R. Stafford, J. Electron. Mater 37, 490-497 (2008)
- [44] NIST, Physical constants database:  
<http://physics.nist.gov/PhysRefData/FFast/html/form.html>.

## Chapter 4

### 4 *Microstructural development and possible whiskering behavior of thin Sn films electro-deposited on Cu(Zn)-substrates*

J. Stein<sup>1,2</sup>, C. A. Cordova Tineo<sup>3</sup>, U. Welzel<sup>1</sup>, W. Huegel<sup>2</sup>, and E. J. Mittemeijer<sup>1,3</sup>

<sup>1</sup> Max Planck Institute for Intelligent Systems (formerly Max Planck Institute for Metals Research), Heisenbergstr. 3, 70569 Stuttgart (Germany)

<sup>2</sup> Robert Bosch GmbH, Automotive Electronics / Engineering Assembly Interconnection Technology (AE/EAI2), Robert-Bosch-Str. 2, 71701 Schwieberdingen (Germany)

<sup>3</sup> University of Stuttgart, Institute for Materials Science, Pfaffenwaldring 55, 70569 Stuttgart (Germany)

Keywords: Sn whisker, brass, whisker mitigation, X-ray diffraction, residual stresses

#### **4.1 Abstract**

The aging behavior at room temperature of thin Sn films, electro-deposited on top of Cu(Zn) substrates containing 15 and 36 wt.% Zn, was investigated, using focused ion beam microscopy and X-ray diffraction analysis to evaluate the microstructural- and (residual) stress development in the specimens. For comparison, parallel experiments and similar analyses were performed with Sn films electro-deposited on pure Cu substrates. Whereas Sn whiskering was observed for the Sn films deposited on the Cu substrates, such whiskering was not observed for the Sn films deposited on the Cu(Zn) substrates. It was found that alloying the Cu substrates with Zn strongly slows down the formation rate of the intermetallic compound  $\text{Cu}_6\text{Sn}_5$  at the Sn/Cu(alloy) interface. The Sn films on the Cu(Zn) substrates remain whisker free for the entire time of investigation even though an overall compressive state of stress has developed after several weeks of aging. It was concluded that a homogeneous, compressive stress in the

Sn film does not lead to whisker formation: the presence of negative stress gradients is essential for Sn whisker growth.

## **4.2 Introduction**

To understand the origin(s) of the formation of metallic whiskers, fundamental research has been performed since, say, the 1950s [1]. Filamentary single crystals [2] (typical diameters between 0.5 and 5  $\mu\text{m}$ ) can grow up to millimeters [3], on top of surfaces, from metal substrates with a low melting point, such as Cd, Zn and Sn [4-6]. From an engineering point of view, whisker formation is a severe reliability issue in the microelectronics industry, since electro-deposited, thin Sn (based) films on lead frame material (often Cu-based alloys) are frequently used in many electronic applications (e.g. electronic control units). Growing Sn whiskers in electronic devices are able to bridge the fine pitches between electronic conductors which often results in a failure of the device [1, 7].

Upon aging of Sn film/Cu substrate systems, a compressive stress is induced inside the Sn film (which usually shows a columnar microstructure (naturally) developing during the deposition process) due to the irregular formation, i.e. in a pyramidal geometry, of the intermetallic compound (IMC)  $\text{Cu}_6\text{Sn}_5$  at the junction of Sn grain boundaries with the Cu substrate during room temperature storage, as the IMC formation is associated with a pronounced increase in volume on the film side [8, 9]. It has been thought for a long time that the compressive nature of this stress is the essential condition for whiskering (see e.g. [10, 11]). However, in recent work it has been shown that the development of (negative) stress *gradients* inside the Sn film, in- and out of plane with respect to the specimen surface, is the crucial condition for Sn whisker formation (see e.g. [12, 13]). As suggested and discussed in Ref. [14], stress-gradient driven [15], long range [16] (Sn) diffusion takes place via a Coble creep type mechanism [17] towards the Sn surface and thus stress gradients act as the driving force for Sn whisker growth [12-14].

A well known Sn whisker mitigation strategy for Sn on Cu specimens is the so-called post-bake treatment, carried out, for example, at 150  $^{\circ}\text{C}$  ( $\approx 423$  K) for 1 h after

the deposition of the film. The enhanced diffusion of Cu from the substrate during the post-bake, triggered by the elevated temperature, leads to the formation of a planar, closed IMC layer at the Cu/Sn interface, consisting of  $\text{Cu}_6\text{Sn}_5$  and  $\text{Cu}_3\text{Sn}$ , which acts as a diffusion barrier and therefore drastically obstructs further continued Cu diffusion into the Sn film (see [18]).

It has been claimed in the literature, on the other hand, that Sn films electro-deposited on Cu(Zn) substrates do not show Sn whisker growth [19], i.e. mitigate Sn whisker formation, and, on the other hand, it has also been stated that a high density of (long) Sn whiskers grow from Sn on brass substrates [3, 20-25].

Against the above background, the present paper presents an analysis of the microstructural development of pure Sn films electro-deposited on Cu(Zn) specimens with a Zn content of 15 and 36 wt.% during room temperature storage in order to analyze the impact on Sn whiskering of alloying the Cu-substrate with Zn. Time-resolved phase analysis and residual stress measurements, by application of X-ray diffraction methods [26, 27], and focused ion beam microscopy were carried out as a function of aging time at room temperature. The results obtained were compared with those obtained in this same project from experiments, performed in parallel fashion and conducted in the same manner, on similar Sn films deposited on pure Cu substrates.

## ***4.3 Experimental***

### **4.3.1 Specimen preparation**

Pure Sn films were electro-deposited on Cu(Zn) substrates as well as on pure Cu substrates applying the same electrolyte and subject to the same conditions. The Sn deposition was carried out using an industrial electrolyte on basis of methasulfonic acid, with organic additives and dissolved metal ions by employing a laboratory setup applying a current density of  $1,5 \text{ A/dm}^2$  at room temperature. Prior to the electro-deposition process, the substrates were ultrasonically cleaned in acetone and deionized water as well as surface activated by dipping in  $10\%-(\text{H}_2\text{SO}_4)_{\text{aq}}$  for a few minutes.

For the Cu(Zn) substrates, two types of commercial brass' were used with a Zn content of either 15 wt.% (Wieland M15: UNF#: C2300, EN#: CW512L) or 36 wt.% (Wieland M36: UNF#: C26800, EN#: CW507L). The pure Cu substrates were the same used before by our group (Wieland K32: UNS# C11000, EN# CW004A) (see e.g. [12,18]). All substrates were cut to strips with dimensions: 2.5 cm × 1.5 cm × 1 mm.

### 4.3.2 Microscopy and electron back scatter diffraction

Cross-sectional microscopical analyses were carried out using a focused ion beam (FIB) microscope ("FEI FIB 200"), operated with an acceleration voltage of 30 kV and beam currents between 11 and 1000 pA for imaging, cleaning and cutting.

The Sn film surfaces were imaged employing a "LEO 145 VP" scanning electron microscope (SEM). This instrument is additionally equipped with an electron backscatter diffraction (EBSD)-system ("TSL/EDAX, Inc."). The EBSD-data obtained were analyzed using the "Orientation imaging microscopy (OIM) 4.5" software.

### 4.3.3 X-ray diffraction (XRD) methods

Phase analyses, pole-figure measurements and diffraction-line measurements (determination of integrated intensities of specific reflections (peak areas)) as a function of aging time at room temperature were performed using a "Philips" (now: "PANalytical") Materials Research and Development (MRD) Pro diffractometer employing parallel-beam geometry and Cu  $K_{\alpha}$  radiation with a beam size of 4×4 mm<sup>2</sup>. The diffractometer was equipped with a conventional, sealed Cu tube (operated at 45kV/ 40 mA) as X-ray source, a polycapillary X-ray lens, realizing parallelization of the X-rays, an Eulerian cradle (four-circle goniometer) which allows rotating and tilting of the specimen, a parallel foils collimator and a flat graphite monochromator as secondary optics to select  $K_{\alpha}$  radiation, as well as a proportional counter. The diffractometer was operated with the "Philips" data collector software.

The phase evolution was traced by comparing the positions of diffraction maxima, in survey scans of specimens recorded at different aging times, with reference

patterns of the respective phases from the literature [28]. The integrated intensity of the  $\text{Cu}_6\text{Sn}_5$  24-1 reflection (peak area) was determined by fitting the peak with a pseudo-Voigt function using the TOPAS (“Bruker AXS”) software (this reflection is of significant intensity and does not suffer from distinct overlap with other reflections).

The reflections were recorded at different aging times with the same step size and time per step. Thus the phase evolution (i.e. an increase or a decrease of phase volume) could be traced as a function of time.

Residual stress measurements [26] were performed without control of the penetration depth [29] on a “Bruker AXS D8 Discover” diffractometer using  $\text{Cu-K}\alpha$  radiation. The X-ray source of this diffractometer is a “Turbo X-Ray source (TXS) Superspeed” rotating anode (50 kV / 20 mA) with a filament size of  $0.1 \times 1$  mm point focus. A two-dimensional (2D) collimating mirror (“Xenocs Fox 2D”) is used for parallelizing as well as for monochromatization of the X-rays. The diffractometer is additionally equipped with a “Huber” 1/4-circle Eulerian cradle, which allows variations of all Eulerian angles. The diffracted X-rays were detected using an energy dispersive detector (“Bruker AXS Sol-X”) with a geometrical acceptance window of approximately  $4 \times 15$  mm<sup>2</sup>. Specimen alignment was performed with help of a justified laser and video camera system. The diffractometer chamber is air-conditioned in order to maintain a constant temperature (approximately  $22$  °C  $\approx$  293K). A spinner was used, which rotates the specimen around the specimen normal, to enhance crystallite statistics. The diffractometer was operated using the “Bruker AXS X-ray diffraction (XRD) commander” software.

Residual stresses of the film material were calculated from the peak positions of the Sn 321-reflection, as recorded at various angles of the specimen tilt,  $\psi$  ( $\psi$ =angle between specimen-surface normal and diffraction vector), by employing the  $\sin^2\psi$ -method [26] and by assuming quasi-isotropy of the Sn film. It was experimentally verified that the stress states of the films in the initial, as deposited state, were planar (parallel to the surface) and rotationally symmetric ( $\sigma_{//} = \sigma_{11} = \sigma_{22}$ ,  $\sigma_{33} = 0$ , no stress in the out-of plane direction). The  $hkl$ -dependent diffraction elastic constants were derived from the single crystal elastic constants [30] adopting the Neerfeld-Hill model [26].

## 4.4 Results

### 4.4.1 Phase and microstructural analysis of the as-deposited state

The diffractograms recorded from both brass substrates (with 15 and 36 wt.% Zn, cf. section 4.3.1) showed that both brass substrates consist of a solid solution of Cu and Zn, i.e.  $\alpha$ -Cu(Zn): the Cu-matrix reflections originating from the Cu(Zn<sub>15 wt.%</sub>) and Cu(Zn<sub>36 wt.%</sub>) solid solutions occur at diffraction-angles,  $2\theta$ , lower than those recorded from the pure Cu substrates as a consequence of the lattice parameter of the Cu matrix being increased upon incorporation of Zn atoms (see Fig. 4-1). The  $\beta$ -phase (CsCl-type [31]), i.e. the intermetallic compound CuZn, was not detected upon aging at room temperature. In view of the compositions of the alloys and the temperatures applied (at  $\sim 101,3$  kPa), these observations are fully consistent with the binary phase diagram of the Cu - Zn system (at  $\sim 101,3$  kPa) [32].

The as-deposited Sn film microstructures of the Sn/Cu(Zn<sub>15 wt.%</sub>) and Sn/Cu(Zn<sub>36 wt.%</sub>) specimens are shown in Fig. 4-2. The FIB images of cross-sections for both specimen types shown in Figs. 4-2 a) and d) have been obtained directly after electro-deposition. The as-deposited Sn film microstructure is predominantly columnar (for both specimen types) with a lateral grain size for both Sn/Cu(Zn) specimens (typically) in the range of  $\sim 1$  to  $\sim 5$   $\mu\text{m}$ . Thus, the Sn grain morphology of both as-deposited Sn films is very similar to the grain morphology of a Sn film, as electro-deposited on a pure Cu substrate, (see Fig. 4-2 in Ref. [14]).<sup>3</sup>

---

<sup>3</sup> It should be noted that the Sn grain boundaries in Figs. 5-2 a) and d) are highlighted as a result of the FIB preparation of the cross-sections: Cu atoms in the gas phase, removed from the substrate material during the sputtering procedure, redeposit preferentially along the Sn grain boundaries once the Ga<sup>+</sup>-beam is switched off. Thus, a smooth film (most likely Cu<sub>6</sub>Sn<sub>5</sub>) appears in bright grey along the Sn grain boundaries which, however, thus is an artifact of the preparation procedure, (see [14] for further details). At this point of time, a significant amount of Cu<sub>6</sub>Sn<sub>5</sub> could not have formed already at the Sn grain boundaries or at the film/substrate interface (see what follows in section 4.4.2).



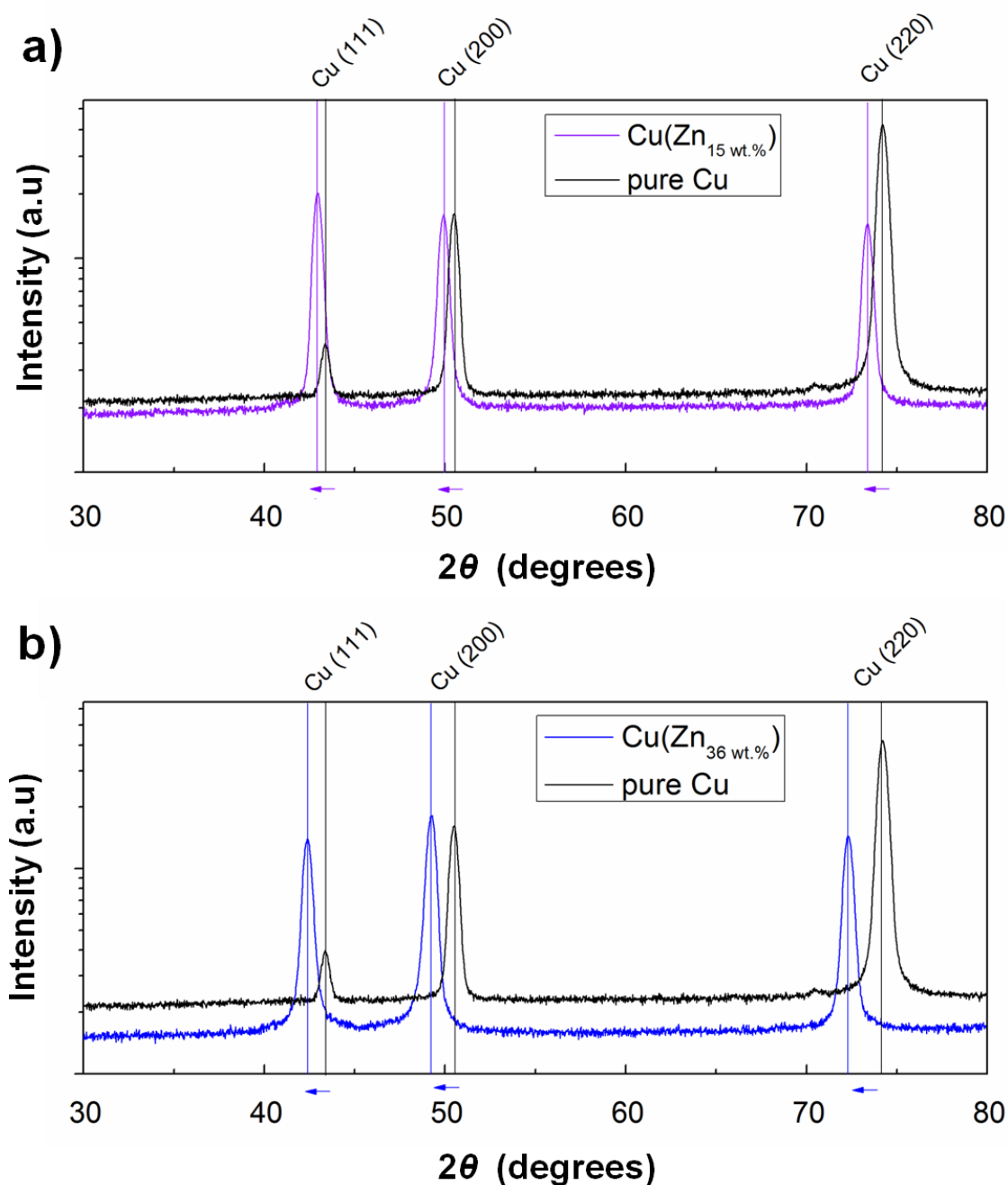
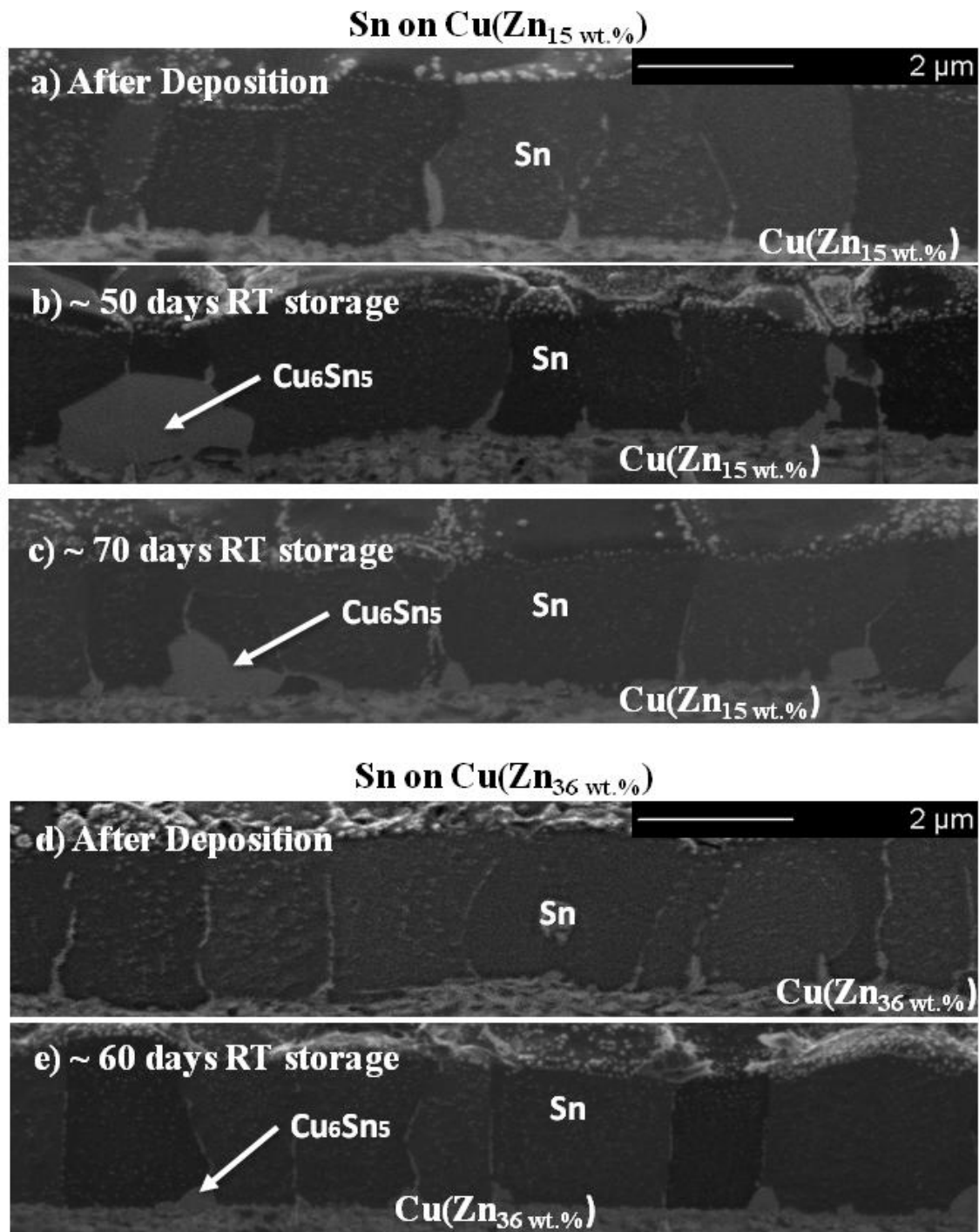


Fig. 4-1: a) XRD diffractogram (survey scan) recorded from a Cu(Zn) substrate with 15 wt.% Zn (purple line) in comparison to the XRD diffractogram recorded from a pure Cu substrate (black line). b) XRD diffractogram recorded from a Cu(Zn) substrate with 36 wt.% Zn (blue line) in comparison to the XRD diffractogram recorded from a pure Cu substrate (black line). The Cu-matrix reflections obtained from the survey scans of the Cu(Zn<sub>15 wt.%</sub>) and Cu(Zn<sub>36 wt.%</sub>) specimens are shifted to lower diffraction-angles,  $2\theta$ , as compared to the corresponding Cu reflections obtained from the pure Cu specimens/substrates, since the lattice parameter of the Cu(Zn) matrix (solid solution) is increased (compared to pure Cu) upon incorporation of Zn atoms.



*Fig. 4-2: FIB microscopy images of cross-sections of Sn/Cu(Zn<sub>15</sub> wt.%) specimens (a), (b) and (c)) and of Sn/Cu(Zn<sub>36</sub> wt.%) specimens (d) and (e)). Directly after deposition (a) and (d)) and after several weeks of storage at room temperature (b), (c) and (e)). The Sn grains appear in dark grey, whereas the Cu<sub>6</sub>Sn<sub>5</sub> phase appears in bright grey. The Cu(Zn) substrate, located at the bottom part of each image, shows a very fine grained microstructure.*

EBSD applied to the surface of the specimens (cf. section 4.3.2), scanning several tens of grains, revealed that the Sn films of the Sn/Cu(Zn<sub>15 wt.%</sub>) and Sn/Cu(Zn<sub>36 wt.%</sub>) specimens exhibit a (weak) Sn {001} fibre texture (see Fig. 4-3). XRD pole-figure measurements revealed that a (weak) Sn {321} fibre texture occurs for the Sn film similarly electro-deposited (cf. section 4.3.1) on pure Cu substrates (see Fig. 4-4 and Ref. [18]). No textural changes were found upon aging at room temperature.

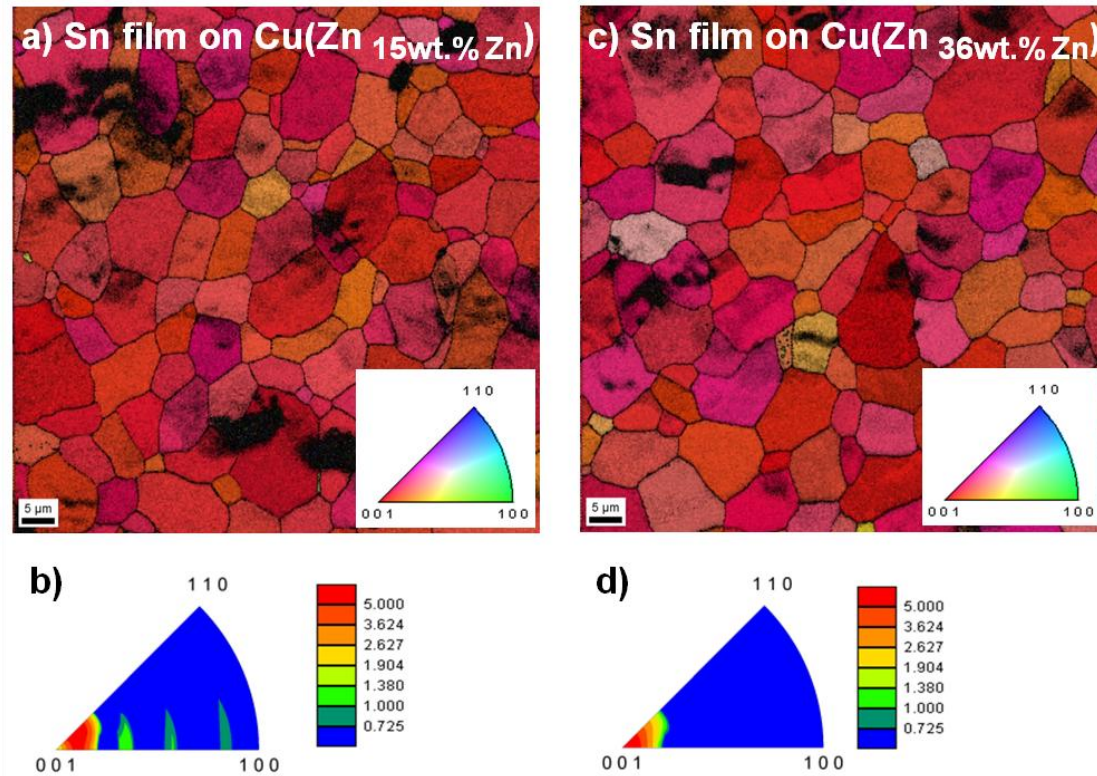
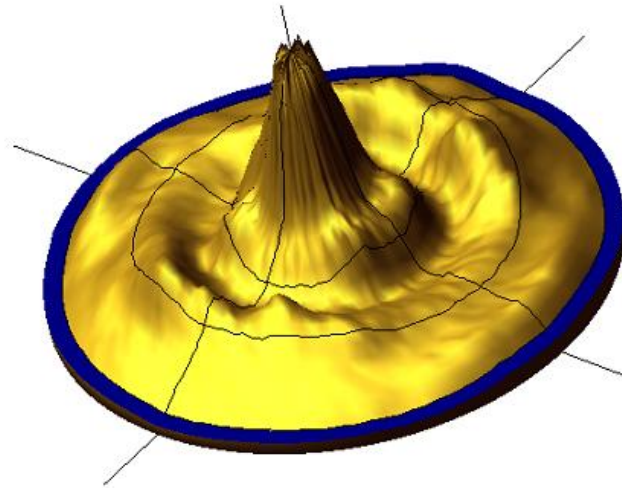


Fig. 4-3: Orientation maps (a) and c)) and surface-normal inverse pole-figures (b) and d)) derived from EBSD measurements on the surface of the Sn films electro-deposited on Cu(Zn) substrates with either 15 wt.% Zn (a) and b)) or 36 wt.% Zn (c) and d)). Both Sn films show a {001} texture. The green areas in the surface-normal inverse pole-figure in b) are due to measurement errors likely caused by shadowing effects since the surface of the Sn film was not completely flat (see also the black areas in the orientation map in a)).



*Fig. 4-4: Three-dimensional plot of a XRD pole-figure derived from a measurement utilizing the Sn 321 reflection, showing the {321} fibre texture of the Sn film (Image taken from an earlier work [18]).*

#### 4.4.2 Stress evolution and microstructural development upon aging at room temperature

The microstructures of the Sn/Cu(Zn<sub>15</sub> wt.%) and Sn/Cu(Zn<sub>36</sub> wt.%) specimens, imaged by FIB microscopy of cross-sections, as obtained after several weeks of storage at room temperature, are presented in Figs. 4-2 b), c) and e).

Upon aging at room temperature the intermetallic compound IMC (Cu<sub>6</sub>Sn<sub>5</sub> appearing in bright grey) starts to form in the Sn film at the interface with the substrate. After 50 days at room temperature, Cu<sub>6</sub>Sn<sub>5</sub> grains, but only sporadically, have grown very substantially, i.e. at some places to a lateral size exceeding half of the Sn film thickness (see the bright grey grain on the left-hand side in Fig. 4-2 b)). However, generally even after several weeks of storage at room temperature, ranges along the Sn/substrate interface stay nearly free of IMC (small pyramidal structures of IMC form at locations where grain boundaries in the Sn film intersect the interface with the substrate). In particular in case of the Sn/Cu(Zn<sub>36</sub> wt.%) specimen, only the small pyramidal Cu<sub>6</sub>Sn<sub>5</sub> grains are observed; evidently, no pronouncedly grown IMC grains can be observed (see Fig. 4-2 e)). In contrast, pronounced Cu<sub>6</sub>Sn<sub>5</sub> grains have formed, after several months of aging at room temperature, at practically all junctions of grain boundaries with the film/substrate interface in Sn/Cu specimens (see Fig. 4-5)) [18].

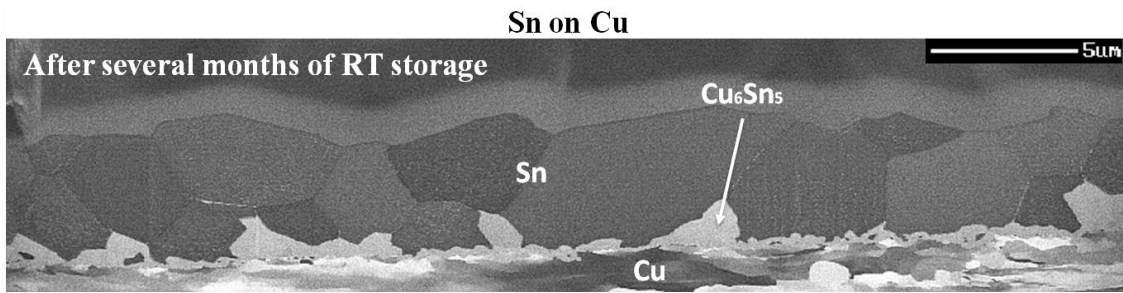


Fig. 4-5: FIB microscopy image of a cross-section of a Sn/pure Cu specimen after several months of storage at room temperature (RT). Image was taken from an earlier work [18].

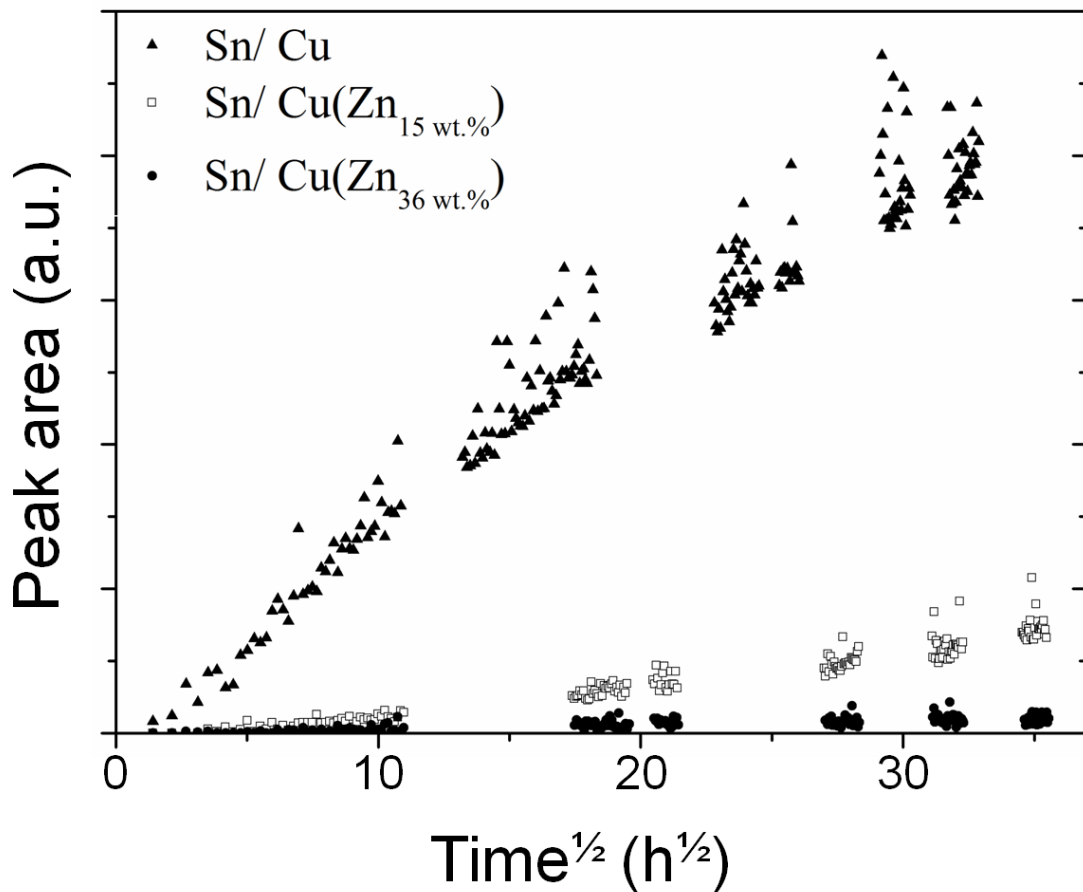


Fig. 4-6: XRD integrated intensity (peak-area) of the Cu<sub>6</sub>Sn<sub>5</sub> 24-1 reflection as a function of aging time at room temperature of a Sn/Cu(Zn<sub>15</sub> wt.%), a Sn/Cu(Zn<sub>36</sub> wt.%) and a Sn/pure Cu specimen. It follows (see text) that the Cu<sub>6</sub>Sn<sub>5</sub> formation is (very) much slower in the Sn/Cu(Zn) specimens as compared to the Sn/pure Cu specimen.

The kinetics of the  $\text{Cu}_6\text{Sn}_5$  growth (for the specimens stored at room temperature) can be traced by measuring the integrated intensity (peak area) of the  $\text{Cu}_6\text{Sn}_5$  24-1 reflection as a function of storage time at room temperature (cf. section 4.3.3). Such results, as obtained from the Sn/Cu(Zn) specimens with 15 and 36 wt.% Zn and from a Sn/pure Cu specimen are shown in Fig. 4-6.

The change of a ( $\text{Cu}_6\text{Sn}_5$ ) peak area is, in general, proportional with the change of ( $\text{Cu}_6\text{Sn}_5$ ) phase volume, provided no texture change occurs as well. Pole-figure measurements performed in this project have shown that the  $\text{Cu}_6\text{Sn}_5$  phase grows nearly untextured. Since the growth morphology of  $\text{Cu}_6\text{Sn}_5$ , as developing in the Sn films, is similar for these different specimen types (i.e. the growth starts at the film/substrate interface and proceeds towards the surface, mainly along the Sn/Sn grain boundaries; cf. above discussion), differences in absorption of incident and diffracted X-rays, due to a possible positional difference of the  $\text{Cu}_6\text{Sn}_5$  phase inside the Sn films for these different specimens, can be neglected. The above discussion leads to the conclusion that the differences in the change of integrated intensity as function of aging time for the Sn films of the three different specimens can be interpreted in terms of differences in  $\text{Cu}_6\text{Sn}_5$  phase volume development.

Hence it is concluded from Fig. 4-6 that the  $\text{Cu}_6\text{Sn}_5$ -phase volume in Sn/Cu(Zn<sub>15 wt.%</sub>) specimen increases very much slower over time than in the Sn/pure Cu specimen; the  $\text{Cu}_6\text{Sn}_5$ -phase volume in Sn/Cu(Zn<sub>36 wt.%</sub>) increases even much more slowly than in the Sn/Cu(Zn<sub>15wt.%</sub>) specimen: it remains close to zero for the investigated period of time.

The stress  $\sigma_{\parallel}$  of the Sn films on the Sn/Cu(Zn) substrates and of the Sn film on the Cu substrate, determined as described in section 4.3.3, is shown as function of aging time at room temperature in Fig. 4-7.

The stress  $\sigma_{\parallel}$  of the Sn film on the Cu substrate changes from a slightly tensile value to compressive values within a few days of aging at room temperature. After approximately 100 h of aging at room temperature, the stress remains more or less constant, i.e. a compressive stress plateau has been reached (see Fig. 4-7 and see also Ref. [14]).

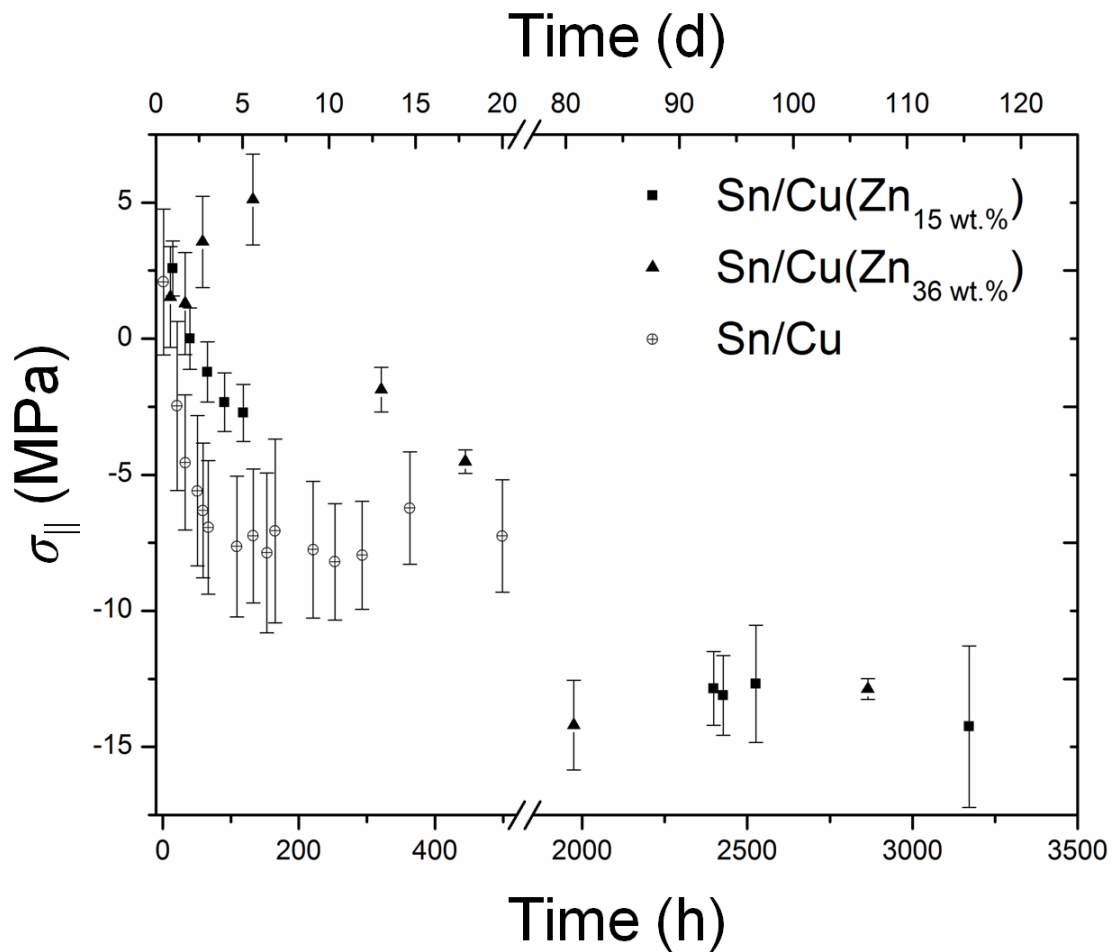


Fig. 4-7: (Biaxial) Stress ( $\sigma_{||}$ ) evolution in the Sn films of both Sn/Cu(Zn) specimen types (with 15 or 36 wt.% Zn in the substrate) and of a Sn/pure Cu specimen (data taken from an earlier work [14]) as function of storage time at room temperature. The build-up of compressive stress in the Sn film of the Sn/Cu(Zn) specimens is much slower than in the Sn film of the Sn/Cu specimen. Upon pronounced aging a compressive stress plateau occurs, also very much later for the Sn/Cu(Zn) specimens than for the Sn/Cu specimens.

A change of  $\sigma_{||}$  from tensile to compressive character is also visible for the Sn film on the Cu(Zn<sub>15 wt.%</sub>) substrate. However, the build-up of compressive stress inside this Sn film is clearly much slower than for the Sn film on the pure Cu substrate.

In case of the Sn/Cu(Zn<sub>36 wt.%</sub>) specimen, the stress  $\sigma_{||}$  becomes more tensile in the initial stage of aging at room temperature. Most likely, processes, such as annealing of defects (= free volume), which can develop during electro-deposition of the Sn film, can be responsible for this effect. This becomes visible only in the Sn/Cu(Zn<sub>36 wt.%</sub>)

specimen since the observed stress evolution consist of a superposition of tensile stress contributions (due to annealing of defects; see above) and compressive stress contributions due to  $\text{Cu}_6\text{Sn}_5$  formation. For the Sn/Cu( $\text{Zn}_{36}$  wt.%) specimen, the build-up of compressive stresses due to  $\text{Cu}_6\text{Sn}_5$  formation is very slow and thus tensile stresses dominate the stress evolution initially. Eventually, that is after a long time of aging at room temperature (cf. Fig. 4-6), the stress in the Sn film on also the Cu( $\text{Zn}_{36}$  wt.%) substrate has been become compressive as well.

FIB surface analysis of the of the Sn/Cu( $\text{Zn}_{15}$  wt.%) and Sn/Cu( $\text{Zn}_{36}$  wt.%) specimens, carried out frequently during storage at room-temperature after deposition, revealed that for the Sn films on the Cu(Zn) substrates, no whisker formation occurred during the entire time of the investigation (i.e. for several months), whereas for the Sn films on the pure Cu substrates pronounced whisker formation occurred already after a few days of aging (see also Ref. [14]). These observations will be discussed in the following.

## 4.5 Discussion

Sn whisker growth is generally thought to be related to the development of stress inside the Sn film [8, 33]. Stress generation inside the Sn film of Sn/Cu(-alloy) specimens during aging at room temperature is (predominantly) determined by the rate of formation and the morphological development of the IMC  $\text{Cu}_6\text{Sn}_5$  phase [14, 18, 34].

Sn whisker growth on top of Sn films, electro-deposited on the pure Cu substrates, under conditions identical to those used for the Sn/Cu( $\text{Zn}_{15}$  wt.%) and Sn/Cu( $\text{Zn}_{36}$  wt.%) substrates, starts after a few days of aging (cf. section 4.4.2), due to the (continuous) formation of IMC of irregular morphology at the Sn/Cu interface [14]. A typical density of whiskers (including hillocks), which develops on top of the surface of such pure Sn/Cu specimens, is  $\sim 400$  whiskers/ $\text{mm}^2$  [35].

Obviously, the  $\text{Cu}_6\text{Sn}_5$  formation *rate* during storage at room temperature at the Sn/Cu( $\text{Zn}_{15}$  wt.%) and Sn/Cu( $\text{Zn}_{36}$  wt.%) interfaces differs strongly from the  $\text{Cu}_6\text{Sn}_5$  formation rate at the Sn/Cu interfaces (see Fig. 4-6 and section 4.4.2). It was shown in [34] that the  $\text{Cu}_6\text{Sn}_5$  formation rate varies with the lateral Sn grain size. For the present



case, the same Sn electrolyte under the same plating conditions was used for the electro-deposition of all Sn films. Thus, it was found that the lateral Sn grain size are also comparable (typical lateral diameters are between 2 and 5  $\mu\text{m}$ ). The main difference between the specimens is however the Zn content in the substrate: Zn dissolved in the Cu substrate pronouncedly slows down the  $\text{Cu}_6\text{Sn}_5$  formation rate at the Sn/Cu(Zn) interface. This observation is consistent with findings in the literature (see also Refs. [19] and [33] albeit pertaining to investigations at elevated temperatures ( $150\text{ }^\circ\text{C} \approx 423\text{ K}$ )). The morphological appearance of the  $\text{Cu}_6\text{Sn}_5$  phase, i.e. the formation of irregular, pyramidal grains, is practically similar in all Sn films considered here. Thus, the relatively slow rate of  $\text{Cu}_6\text{Sn}_5$  formation in the Sn/Cu(Zn) specimens can be understood as follows.

Alloying of pure Cu with Zn (i.e. here formation of the solid solution Cu(Zn)), in general, lowers the chemical potential of Cu in the Cu-Zn solid solution and thus the driving force for Cu diffusion into Sn (or  $\text{Cu}_6\text{Sn}_5$ , respectively, after a continuous layer of  $\text{Cu}_6\text{Sn}_5$  has formed), as the chemical potential of a component in an (ideal) solid solution is proportional to the logarithm of the concentration of that component. Indeed the growth rate is slowest for the substrate with the highest Zn content.

Apart from a generally lower driving force for the  $\text{Cu}_6\text{Sn}_5$  formation (as indicated directly above), a further effect contributing to slowing down the growth rate of the  $\text{Cu}_6\text{Sn}_5$  phase in the specimen with Cu(Zn) substrates may be the occurrence of a local Zn enrichment in the substrate upon formation of  $\text{Cu}_6\text{Sn}_5$  at the substrate/film interface, recognizing that the solubility of Zn in Sn is very low according to the phase diagram [32], which, in accordance with the above discussion, enhances the retardation of  $\text{Cu}_6\text{Sn}_5$  formation.

It may be argued that Zn from the substrate might be incorporated in the IMC. However, the  $\text{Cu}_6\text{Sn}_5$  phase can contain only Zn up to 7.2 at% at  $150\text{ }^\circ\text{C}$  [36]. No thermodynamic data for the solubility of zinc in  $\text{Cu}_6\text{Sn}_5$  at room temperature are available. However, it is likely that at room temperature the solubility of Zn in  $\text{Cu}_6\text{Sn}_5$  must be much smaller than 7.2 at% (pertaining to  $150\text{ }^\circ\text{C}$ ).

The consequence of the (very) slow formation rate of IMC at the film/substrate interfaces of Sn/Cu(Zn) specimens, as compared to Sn/pure Cu specimens, as revealed in this study, for the development of the state of stress in the Sn film during room temperature storage, is discussed next.

In case of a whiskering Sn/pure Cu specimen, the macroscopic stress in the film parallel to the surface attains a compressive stress plateau after only a few days of aging at room temperature (cf. [14, 37] and see Fig. 4-7) in combination with the development of negative stress-depth gradients, which build the driving force for Sn diffusion from the bottom part to the top part of the Sn layer [12, 13]. As can be seen from Fig. 4-7 (cf. also section 4.4.2), build-up of compressive stress takes place very slowly in the Sn films of the Sn/Cu(Zn) systems and a compressive stress plateau is attained only after a couple of months, due to the very slow formation rate of the IMC.

Stress relaxation in the Sn film occurs by Coble creep [9,11,14,38], possibly leading to whisker formation at locations at the surface where grains occur which are bordered by grain boundaries inclined with respect to the surface. At such inclined grain boundaries, shear stresses act due to the planar state of stress in the Sn film which enables grain boundary sliding at these locations, i.e. a surface grain with tilted grain boundaries can grow in the outward (i.e. unconstrained) direction of the film as long as transport of Sn atoms takes place to the root of the whisker [14]. Now, the very slow formation of IMC in case of the Sn/Cu(Zn) systems allows substantial relaxation of the stress in the Sn films (as induced by IMC formation) such that, as compared to the Sn/Cu system, development of substantial stress-depth gradients is counteracted. Thus, no distinct transport of Sn from the bottom part to the top part of the Sn film is induced and, hence, no whisker formation occurs, even though an overall (but more or less homogeneous) state of compressive stress prevails.

The occurrence of a stress plateau, upon continued aging, is the consequence of balancing stress-development and stress-relaxation processes. The, as measured (weighted) depth-averaged, smaller, apparent value of the resulting compressive stress plateau for the Sn films on the pure Cu substrates, as compared to that for the Sn films on the Cu(Zn) substrates, is the consequence of the presence of a stress-depth profile in the Sn films on the pure Cu substrates (the stress varies from a possibly tensile value, at

the surface of the Sn film, to a distinctly compressive value in the bottom region of the Sn film [13]), whereas the stress in the Sn films on the Cu(Zn) substrates is expected to be more or less constant throughout the film, so that its as measured (weighted) depth-averaged value is more representative of the occurring compressive state of stress. This is likely related to the much slower IMC growth at the film/substrate interface in case of the Cu(Zn) substrates as compared to the pure Cu substrates (cf. section 4.4.2).

## ***4.6 Conclusions***

- The rate of IMC formation in Sn/Cu(Zn) specimens is very much slowed down compared to Sn/pure Cu specimens due to a smaller driving force for the  $\text{Cu}_6\text{Sn}_5$  formation at the film/substrate interface, because the difference of the chemical potential of Cu between substrate and film is reduced in Sn/Cu(Zn) specimens (and no or only a marginal amount of Zn can dissolve in Sn and  $\text{Cu}_6\text{Sn}_5$ ).
- The very slow rate of formation of IMC in case of the Sn/Cu(Zn) systems allows substantial relaxation of the overall stress in the Sn films (by Coble creep) before pronounced stress-depth gradients can develop.
- Due to the absence of pronounced stress-depth gradients, no distinct net transport of Sn from the bottom part to the top part of the Sn film is induced and no whisker formation occurs, even though an overall (but more or less homogeneous) state of compressive stress prevails upon pronounced aging of Sn/Cu(Zn) at room temperature.

## ***4.7 Acknowledgment***

The authors would like to thank Dr. A. Leineweber and Dr. S. Meka (both Max Planck Institute for Intelligent Systems (formerly Max Planck Institute for Metals Research)) for helpful discussion.

## 4.8 References

- [1] G.T. Galyon, IEEE Trans. Electron. Packag. Manuf. 28, 94 (2005).
- [2] C. Herring and J.K. Galt, Phys. Rev. 85, 1060 (1952).
- [3] V.K. Glazunova and N.T. Kudryavtsev, Zh. Prikl. Khim. 36, 543 (1963).
- [4] K.G. Compton, A.A. Mendizza, and S.M. Arnold, Corrosion 7, 327 (1951).
- [5] W.C. Ellis, Trans. Met. Soc. AIME 236,872 (1966).
- [6] H.L. Cobb. Mon. Rev. Am. Electroplaters Soc. 33, 28 (1946).
- [7] NASA, Whisker Failures: <http://nepp.nasa.gov/whisker/failures/index.htm>.
- [8] B.Z. Lee and D.N. Lee, Acta Mater. 46, 3701 (1998).
- [9] W.J. Boettinger, C.E. Johnson, L.A. Bendersky, K.W. Moon, M.E. Williams, and G.R. Stafford, Acta Mater. 53, 5033 (2005).
- [10] G. Galyon, L.Palmer and R. Gedney, Glob. SMT & Packag. 5, 10 (2005)
- [11] J. Smetana, IEEE Trans. Electron. Packag. Manuf. 30, 11 (2007).
- [12] M. Sobiech, M. Wohlschloegel, U. Welzel, E.J. Mittemeijer, W. Huegel, A. Seekamp, W. Liu, and G.E. Ice, Appl. Phys. Lett. 94, 221901 (2009).
- [13] M. Sobiech, U. Welzel, E.J. Mittemeijer, W. Huegel, and A. Seekamp, Appl. Phys. Lett. 93, 011906 (2008).
- [14] M. Sobiech, J. Teufel, U. Welzel, E.J. Mittemeijer, and W. Huegel, J. Electron. Mater. 40, 2300 (2011).
- [15] R.M. Fisher, L.S. Darken, and K.G. Carroll, Acta Metall. 2, 368 (1954).
- [16] P.L. Key, Proc. of the IEEE Electron. Comp. Techn. Conf., 155-157 (1970).
- [17] R.L. Coble, J. Appl. Phys. 34, 1679 (1963).
- [18] M. Sobiech, U. Welzel, R. Schuster, E.J. Mittemeijer, W. Huegel, A. Seekamp, V. Mueller, Proc. of the 57th Electro. Comp. Techn. Conf., 192-197 (2007).
- [19] S.M. Miller, U. Sahaym, M.G. Norton, Metall. Mater. Trans. A-Phys. Metall. Mater. Sci. 41A, 3386 (2010).
- [20] Y. Fukuda, M. Osterman, and M. Pecht, IEEE Trans. Electron. Packag. Manuf. 30, 36 (2007).
- [21] R. Schetty, Circuit World 27, 17 (2001).
- [22] S. Mathew, M. Osterman, M. Pecht, F. Dunlevey. Circuit World 35, 3 (2009).
- [23] S.C. Britton, M. Clarke, Proc. of the 6th Int.Metal Finish. Conf., 205-211 (1964).
- [24] C.L. Rodekohr, G.T. Flowers, J.C. Suhling, M.J. Bozack. Proc. of the IEEE Holm Conf. Electric. Contacts, 245-248 (2008).
- [25] K. Fujiwara, R. Kawanaka, J. Appl. Phys.51, 6231 (1980).
- [26] U. Welzel, J. Ligot, P. Lamparter, A.C. Vermeulen, and E.J. Mittemeijer, J. Appl. Crystallogr. 38, 1 (2005).
- [27] E.J. Mittemeijer and U. Welzel, Modern Diffraction Methods, (Wiley-VCH Weinheim, 2012).
- [28] PDF-2, International Center for Diffraction Data (ICDD) Version 2.1 (2002).
- [29] A. Kumar, U. Welzel, and E.J. Mittemeijer, J. Appl. Crystallogr. 39, 633 (2006).
- [30] C.J. Smithells and E.A. Brandes, Metal Reference Book (Butterworths London, 1976), pp. 975–980.
- [31] A.R. West, Basic solid state chemistry (John Wiley and Sons Ltd., Weinheim, 1992)

- [32] Z. Moser, J. Dutkiewicz, W. Gasior, J. Salawa. *Bull. Alloy Phase Diagr.* 6, 330 (1985).
- [33] C.Y. Yu, K.J. Wang, J.G. Duh. *J. Electron. Mater.* 39, 230 (2010).
- [34] E. Chason, N. Jadhav, F. Pei, E. Buchovecky, A. Bower, *Progr. Surf. Sci.* 88, 103 (2013)
- [35] J. Stein, U. Welzel, W. Huegel, S. Blatt, E. J. Mittemeijer, *J. Appl. Cryst.* 46, 1645 (2013).
- [36] C.Y. Chou, S.W. Chen. *Acta Mater.* 54, 2393 (2006).
- [37] E. Chason, N. Jadhav, W.L. Chan, L. Reinbold, K.S. Kumar. *Appl. Phys. Lett.* 92, 171901 (2008).
- [38] P. Sarobol, J.E. Blendell, C.A. Handwerker. *Acta Mater.* 61, 1991 (2013)



## Chapter 5

### 5 *Imposition of defined states of stress on thin films by a wafer-curvature method; validation and application to aging Sn films*

J. Stein<sup>1,2</sup>, M. Pascher<sup>3</sup>, U. Welzel<sup>1</sup>, W. Huegel<sup>2</sup>, and E.J. Mittemeijer<sup>1,3</sup>

<sup>1</sup> Max Planck Institute for Intelligent Systems (formerly Max Planck Institute for Metals Research), Heisenbergstr. 3, 70569 Stuttgart (Germany)

<sup>2</sup> Robert Bosch GmbH, Automotive Electronics / Engineering Assembly and Interconnect Technology (AE/EAI2), Robert-Bosch-Str. 2, 71701 Schwieberdingen (Germany)

<sup>3</sup> Institute for Materials Science, University of Stuttgart, Pfaffenwaldring 55, 70569 Stuttgart (Germany)

Keywords: X-ray diffraction, Stress analysis, Wafer bending, Wafer curvature method, Tin whiskers

#### 5.1 *Abstract*

A wafer-curvature method has been developed to subject thin films, deposited on (Si) substrates, to well defined and controllable loads in a contact-free manner. To this end, a custom-made glass pan (i.e. a roof-less cylinder with a connection piece for vacuum tubes) connected to a needle valve, a vacuum pump and a pressure gauge have been used as experimental setup. By fixing the coated Si wafer on top of the glass cylinder and evacuating the glass cylinder to a defined low-pressure, a state of stress is imposed in the thin film due to bending of the wafer. It has been shown that the (initial) stress state of a film and its change, due to its bending with help of the wafer-curvature method, can be analyzed accurately close to the wafer center by application of one of two independent X-ray diffraction techniques: i) conventional X-ray diffraction stress analysis (i.e. application of the well known  $\sin^2\psi$ -method) to reflections originating from the *film* and ii) determination of the radii of curvature by rocking curve

measurements utilizing reflections originating from the *substrate*. The validation of this stress-imposition method has been carried out with a tungsten film of 500 nm thickness, since tungsten is known to be (practically) intrinsically elastically isotropic. Further, the method has been applied to an electro-deposited, potentially whiskering, aging Sn film of 3  $\mu\text{m}$  thickness where a combination of both stress-measurement techniques is essential for the determination of initial and (by wafer bending) imposed stresses. The results of the aging experiment of the Sn film under load have been discussed with respect to the current whisker-growth model.

## 5.2 Introduction

The interrelation of stress and diffusion in solids is a topic of great scientific and practical, engineering interest:

Apart from the role of a hydrostatic state of stress [1], no experimentally validated generally applicable theory is available. For example, the theory as developed by Cahn and Larche [2,3] for so called “network solids” could hitherto not be rigorously tested experimentally, also because the constraints of the theory could not be satisfied in the experiment. Yet, detailed experiments on stress development in interdiffusing systems have been performed, especially considering thin film systems (e.g. see [4-6])

States of stress in thin film systems (usually of planar, not hydrostatic (see above) nature) can have great impact on practical applications of, for example, electronic devices. An outspoken example is provided by the occurrence of whiskering on the surface of Sn films, present on, usually Cu substrates [7-10]. This phenomenon has commonly been ascribed to the presence of compressive stress in the Sn film (but see what follows in this paper).

Research on the effect of stress on diffusion (and vice versa) until now focused on interdiffusion studies in thin film systems without control of the state of stress. Hence, in particular against the above stated background, it appears desirable to develop a device that allows the external application of a local, state of stress to the thin film system, and its maintenance, in a controllable and quantitative manner.



In the following, a method is presented that makes possible: i) the introduction of a defined state of stress in a thin film system with a surface contact-free method, i.e. without damaging the film surface, and ii) the application of X-ray diffraction (XRD) techniques to detailedly and non-destructively determine and follow the lattice strain in the externally stressed film. This stress-imposition method is validated by measurements on a tungsten film and applied to (potentially whiskering) tin films.

## 5.3 Experimental

### 5.3.1 Experimental setup for stress imposition and specimen preparation

The experimental setup, developed for the current study, is schematically shown in Fig. 5-1a). A thin film coated Si wafer is fixed on top of a custom-made “glass pan” (i.e. a roof-less glass cylinder (diameter = 0.07 m), provided with a connection piece for vacuum tubes. The pressure inside the glass pan can be adjusted with the help of a vacuum pump, a needle valve and a pressure gauge. The Si wafer and thus the film can be bent by evacuating the glass pan to a defined low pressure. Corresponding with the bending, an externally applied load acts on the thin film, leading to compression of the film material in case the film was (previously) deposited on the topside of the Si wafer (cf. Fig. 5-1a) and b)). The glass pan (including the Si-wafer fixed on top) can be mounted on the specimen stage inside the X-ray diffractometer chamber for X-ray diffraction analyses.

Thin W (tungsten) and Sn (tin) films, deposited on top of commercial {100} oriented Si-wafers (diameters = 4 inch  $\approx$  0.1 m, covered with 50 nm SiO<sub>2</sub> (silicon dioxide) layers), were used as specimens for investigation in this work. The W (body centered cubic, space group:  $Im\bar{3}m$ , with lattice parameters  $a = b = c = 3.17 \text{ \AA}$  [11]) coating, with thickness of 500 nm, was deposited applying magnetron sputtering (base pressure of about  $5 \cdot 10^{-8}$  mbar) with Ar (argon) as sputtering gas at  $\sim 4.7 \cdot 10^{-3}$  mbar. The substrate was rotated during the deposition procedure.

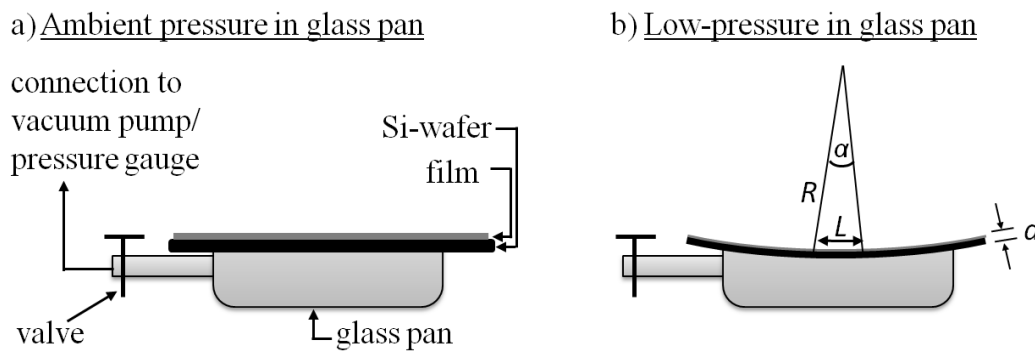


Fig. 5-1: Sketch of the experimental setup used in the current study. A custom-made glass pan (i.e. a roof-less cylinder with a connection piece for vacuum tubes) is connected by a valve to a vacuum pump and a pressure gauge. a): Glass pan and coated Si wafer (the film is deposited on the topside of the wafer) in the initial (i.e. unbent) state at ambient pressure. b): The coated Si wafer, fixed on top of the glass pan, is bent due to evacuation of the glass cylinder to a defined low-pressure. Due to the bending, a compressive state of stress is imposed in the film. The symbols  $d$ ,  $R$  and  $L$  indicate the wafer thickness, the radius of curvature and the arc length, respectively.  $\alpha$  denotes the angle spanning the arc length given by the bent surface of the film.

The Sn film, with a thickness of  $\sim 3 \mu\text{m}$ , was electro-deposited using an industrial pure, “matte” Sn electrolyte on the basis of methanesulfonic acid with organic additives and dissolved metal ions by employing a laboratory setup and a current density of  $1,5 \text{ A/dm}^2$  at room temperature [12]. Prior to the Sn deposition process, two very thin layers, a titanium (Ti) on top of a very thin nickel (Ni) layer (both 20 nm thickness), were deposited on top of the Si wafer, via sputtering, to ensure adhesion of the Sn film on the substrate. The Sn (tetragonal, space group:  $I4_1/amd$ , with lattice parameters  $a = b = 5.83 \text{ \AA}$  and  $c = 3.18 \text{ \AA}$  [13]) film showed a  $\{321\}$  fibre texture (cf. pole-figure in Fig. 5-2).

For the bending experiments, different low pressures were realized in the glass pan ( $\sim 850$  and  $\sim 900$  mbar), in order to impose similar strain distributions in both coating materials (cf. section 5.4.1), since the curvatures in the initial (unloaded) states of the coated Si wafers differ (due to the presence of different residual stresses in the film materials and different curvatures of the Si substrates in uncoated condition).

Cross-sectional and surface analyses of the Sn film were done using a focused ion beam (FIB) microscope (FEI FIB 200), which was operated with an acceleration

voltage of 30 kV and beam currents between 11 and 1000 pA for imaging, cleaning and cutting.

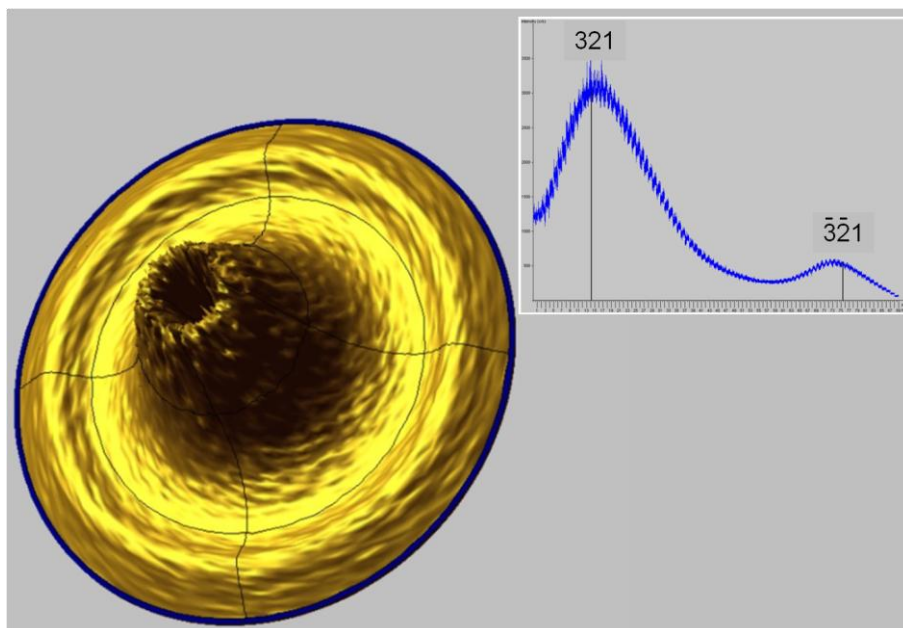


*Fig. 5-2: Three-dimensional plot of a XRD pole-figure derived from a measurement utilizing the Sn 220 reflection and a section through the pole-figure (inlay plot), showing the {321} fibre texture of the  $\sim 3 \mu\text{m}$  Sn film.*

### 5.3.2 X-ray diffraction analyses

X-ray diffraction analyses were carried out applying a “Bruker AXS D8 Discover diffractometer” operated with  $\text{Cu-K}\alpha$  radiation. The X-ray source of this diffractometer is a “TXS Superspeed” rotating anode (50 kV / 20 mA) with a filament size of  $0.1 \times 1$  mm point focus. A 2D- collimating mirror (“Xenocs Fox 2D”) is used for parallelizing as well as for monochromatization of the X-rays. The diffractometer is additionally equipped with a “Huber” 1/4-circle Eulerian cradle, which allows tilting and rotating of the specimen stage. The diffracted X-rays were detected using an energy dispersive detector (Bruker AXS Sol-X) with a geometrical acceptance window of approximately  $4 \times 15 \text{ mm}^2$ . Specimen alignment was realized with help of a justified laser and a video camera system. The diffractometer chamber was air-conditioned in order to maintain a constant temperature. The diffractometer was operated via the Bruker “XRD commander” software.

Analyses of residual and (by wafer bending) imposed strains/stresses in the film material were performed applying two different approaches: (i) conventional XRD stress analysis, by scanning reflections originating from the film material at different orientations of the diffraction vector with respect to the surface of the film, and, (ii) analysis and calculation of imposed stresses from radii of curvature measurements applying rocking curve scans on reflections originating from the substrate material.

Ad (i): Conventional XRD stress analysis was carried out applying the  $\sin^2\psi$  - method utilizing W 110 and Sn 321 reflections, recognizing the intrinsic elastic anisotropy while adopting macroscopic isotropy (i.e. quasi-isotropy [14]) of the polycrystalline film materials, i.e. X-ray elastic constants were employed for relating measured lattice strain and mechanical stress (see e.g. [14]). It was verified that the stress states of the films in the initial, as deposited state, were planar and rotationally symmetric. The Cartesian specimen frame of reference is defined such that the  $S_3$  axis is oriented perpendicular to the specimen surface. The axes  $S_1$  and  $S_2$  are parallel to the specimen surface (and perpendicular to each other). For the case of a rotationally symmetric ( $\sigma_{\parallel} = \sigma_{11} = \sigma_{22}$ ), biaxial (i.e. planar) stress state ( $\sigma_{33} = 0$ , no stress in the out-of plane direction), the biaxial stress in the film  $\sigma_{\parallel}$  is independent of the direction parallel to the surface. The acting stress in the film then obeys [14]

$$\varepsilon_{\psi}^{hkl} = \left( 2S_1^{hkl} + \frac{1}{2} S_2^{hkl} \sin^2 \psi \right) \sigma_{\parallel} \quad (5.1)$$

and is determined by measuring the strain  $\varepsilon_{\psi}^{hkl}$  at different tilt angles  $\psi$  of the diffraction vector for the hkl reflection with respect to the specimen surface ( $\psi$  is thus given by the angle between the normal of the specimen surface, and the normal of the set of diffracting lattice planes). Hence,  $\sigma_{\parallel}$  follows from the slope of the straight line fitted to the experimental data in a plot of  $\sin^2\psi$  vs.  $\varepsilon_{\psi}^{hkl}$  [14]. The hkl-dependent diffraction elastic constants  $S_1^{hkl}$  and  $S_2^{hkl}$  were derived from single crystal data [15] adopting the Neerfeld-Hill model [14].

To enhance the crystallite statistics in case of the  $\sin^2\psi$  - analysis of the Sn film (exhibiting a relatively large grain size of typically 1 to 5  $\mu\text{m}$  – cf. section 5.4.2 and

Fig. 5-3), the Sn coated wafer had to be removed from the glass pan and mounted on a spinner, which rotates the specimen around the surface normal (The spinner cannot be used in combination with the glass pan due to geometrical constraints). Conventional XRD stress analysis, i.e. application of the  $\sin^2\psi$  method, on the Sn film could therefore only be performed in the unbent, unloaded state of the Sn coated wafer.

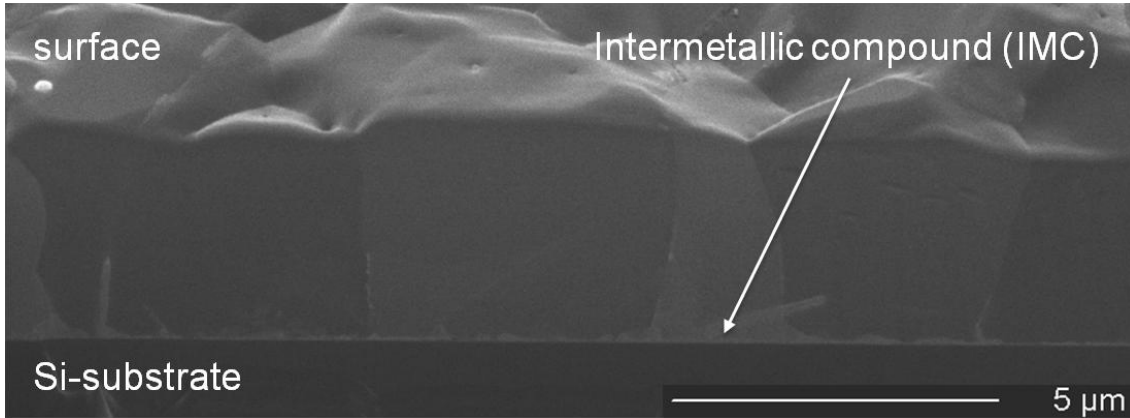


*Fig. 5-3: Microstructure of the predominantly columnar Sn film of  $\sim 3 \mu\text{m}$  thickness, as electro-deposited on a Si-substrate, as revealed by focused ion beam (FIB) microscopy. Prior to electro-deposition of the Sn film, very thin Ti and Ni layers were deposited by sputtering on the wafer in order to ensure adhesion of the Sn-film on the substrate. The Sn film exhibits typical (lateral) grain sizes between 1 and  $5 \mu\text{m}$ . A relatively small amount of an intermetallic compound (IMC) has formed at the film-substrate interface as a result of an interfacial reaction between Sn and the thin Ni-adhesion layer.*

Ad (ii): The substrate curvature was determined by measuring rocking curves (scans made with variable angle of incidence,  $\omega$ , with respect to the film surface on the specimen at fixed diffraction angle,  $2\theta$  (as set by the detector position), for the Si 400 reflection. The rocking curves were recorded at different positions,  $x_i$ , on the film surface. The radius of curvature,  $R$ , of the investigated surface (=top of the wafer in Fig. 5-1) for the range  $\Delta x$  between two locations  $x_1$  and  $x_2$  on the film surface can be calculated from the difference in  $\omega$  of the peak maxima of the rocking curves measured at  $x_2$  and  $x_1$ ,  $\Delta\omega$ , applying [16,17]

$$R = \frac{\Delta x}{2 \sin\left(\frac{\Delta\omega}{2}\right)}. \quad (5.2)$$

If a wafer of thickness  $d$  is bent over an arc length  $L^{Top}$  at the topside of the wafer with a radius of curvature  $R$ , it holds

$$L^{Top} = \alpha \cdot R. \quad (5.3)$$

where  $\alpha$  denotes the angle spanning the arc length at the topside of the wafer (i.e. at the bent surface of the film (of negligible thickness as compared to the thickness of the wafer); cf. Fig. 5-1b). The arc length of the neutral (stress-free) axis in the wafer parallel to the surface thus is

$$L^0 = \alpha \cdot \left(R + \frac{d}{2}\right). \quad (5.4)$$

The strain, imposed on the film at the topside of the wafer, as induced by the wafer bending, can be calculated from  $L^{Top}$  and  $L^0$  according to

$$\varepsilon_{\parallel} = \frac{L^{Top} - L^0}{L^0} = \frac{-d}{2R + d}. \quad (5.5)$$

This result presupposes that the wafer is initially completely flat. In case of an initially bent wafer (e.g. from the manufacturing procedure or due to presence of residual stresses in the film), the imposed strain is obtained by subtracting the strain value measured before evacuation of the glass pan from that measured after evacuation. Imposed stresses were derived by application of Hooke's law for the case of a biaxial stress state (i.e.  $\delta_{\parallel} = \frac{E}{1-\nu} \cdot \varepsilon_{\parallel}$ ) using literature data [15] for the biaxial modulus

( $M = \frac{E}{1-\nu}$ ) of W and Sn.

## 5.4 Results and discussion

### 5.4.1 Characterization of the imposed state of strain/stress

The strain  $\varepsilon_{\parallel}$  imposed by evacuation of the glass pan, as determined from radii of curvature measurements, performed before and after bending (cf. text below Eq. (5)) of a W/Si wafer and of a Sn/Si wafer is shown in Fig. 5-4 as function of the distance,  $x$ , to the centre of the wafer. The curvature measurements, shown in Fig. 5-4, were

performed along a straight line from the wafer center to the wafer edge. The measurement was repeated after rotating the wafer around an axis parallel to the specimen-surface normal. The calculated data points derived from such measurements along different directions on the Sn/ Si wafer, indicated by the angle of rotation,  $\varphi$ , around the surface normal, have been added in Fig. 5-4. Evidently, the bending imposed by the partial evacuation of the glass pan leads to a radially symmetric strain distribution over the film surface (cf. Fig. 5-1). It should be noted that radii of curvatures were determined for distance ranges between two spots on the wafer (cf. section 5.3.2), e.g. between 0.005 m and 0.01 m, and that the thus determined strain values have been assigned to the midpoints of these consecutive ranges.

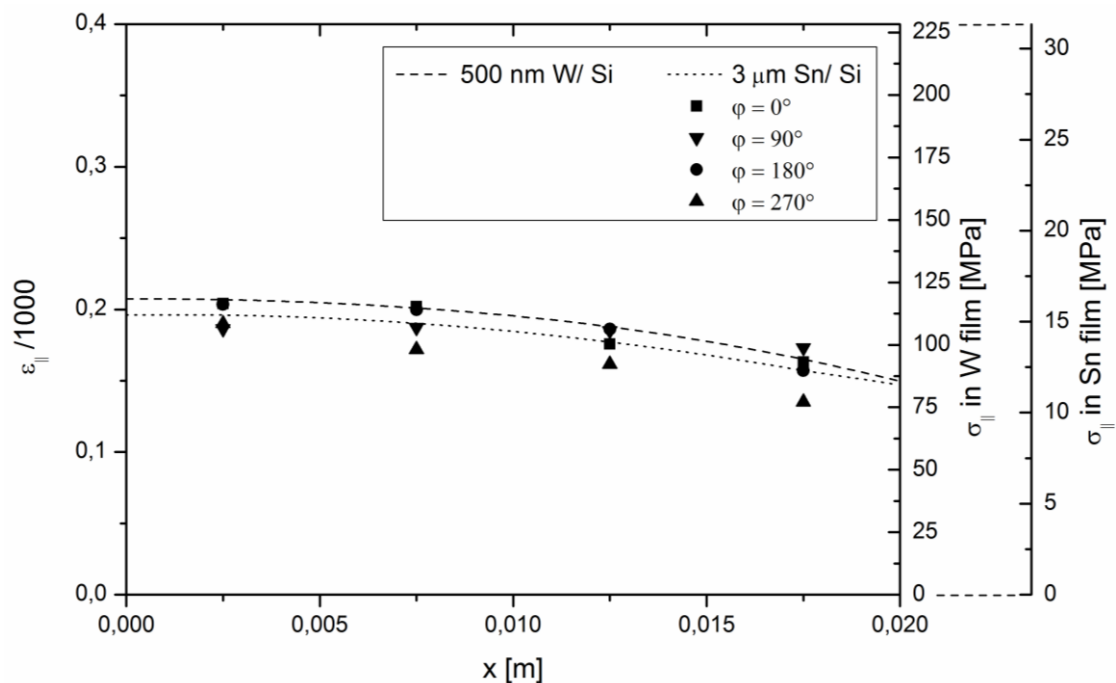


Fig. 5-4: Imposed states of strain ( $\varepsilon_{||}$ )/stress ( $\sigma_{||}$ ) as function of distance to the wafer center ( $x$ ) as determined from radii of curvature measurements on W/Si and Sn/Si specimens. Different low pressures were adjusted in the glass pan ( $\sim 850$  and  $\sim 900$  mbar, respectively) in order to impose similar strain distributions in both films, since the curvatures in the initial (unbent) states of the coated Si wafers differ. Curvature measurements were performed along straight lines starting from the wafer center towards the wafer edge: the data points derived from measurements along different directions on the Sn/ Si wafer (indicated by the angle of rotation,  $\varphi$ , around the surface normal) have been indicated. The dashed lines indicate polynomial fits through the data points.

For the “ideal” case that the wafer would deform upon evacuation to the surface of a sphere, a constant strain state, i.e. independent of position on the surface, would result. Such “ideality” can only be observed close to the wafer center, (i.e., say, for  $|x| \leq 0.01$  m). Upon increasing distance to the wafer center (i.e. for  $|x| > 0.01$  m)  $\varepsilon_{//}$  decreases, most pronouncedly, close to the contact area of wafer and glass pan (not shown in Fig. 5-4) due to the non-rotationally symmetric stress state induced by the presence of the contact area between the wafer and the glass pan (note that no force/pressure acts on the outer perimeter of the wafer protruding over the contact area with the glass pan, see Fig. 5-1 and section 5.3.1).

A comparison of the stress values in the loaded (=bent) W film, as obtained by (i) the radii of curvature measurements and (ii) conventional XRD stress analysis (cf. section 5.3.2), is provided by Fig. 5-5. A tungsten film has been chosen for this comparison because W is practically intrinsically elastically isotropic and therefore effects of texture and grain interactions, which in general can complicate the conventional diffraction stress analysis on the basis of the  $\sin^2\psi$ -method [18, 19], do not occur here. Further, stress relaxation processes in tungsten films cannot occur at room temperature, in view of its relatively high melting point.

The conventional XRD stress analysis applied to the W/Si specimen reveals that in the initial, as prepared state, a (relatively) high compressive residual stress ( $\sim -1.7$  GPa) is present with a minor lateral gradient of less than  $-0.004$  GPa/mm from the centre of the wafer towards the edge of the wafer. The *additional*, imposed stress by bending/evacuation was determined at five different spots on the W film by subtracting the stress measured before bending from that measured after bending. These results are shown in Fig. 5-5. Clearly, the imposed stress values, determined by XRD stress analysis and by XRD radii of curvature measurements are in good agreement. Imposed (compressive) stresses of approximately  $\sigma_{//} \approx 120$  MPa were determined in the area around the wafer centre (see the three data points in Fig. 5-5 for  $|x| < 0.01$  m) independent of the applied stress measurement method.

Close to the contact area of wafer and glass cylinder an inhomogeneous/non-ideal strain/stress state occurs (see above). This leads to differences between results



obtained by both independent XRD techniques in these surface regions as the measurement areas for both techniques are not identical.

It can be concluded from Fig. 5-5 that the bending imposed stresses can be well determined by both XRD techniques (i.e. conventional XRD stress analysis and radii of curvature measurements) at the film surface close to the wafer centre.

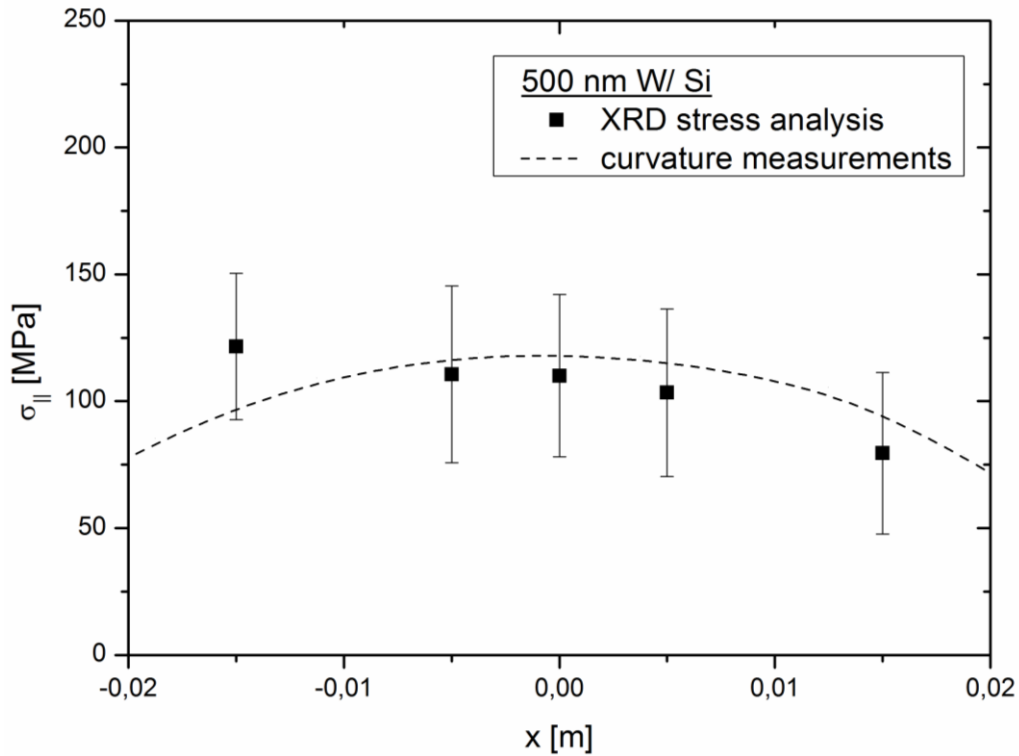


Fig. 5-5: Imposed stress ( $\sigma_{||}$ ) in the W film as function of (lateral) position on the wafer ( $x$ ) determined by application of conventional XRD stress analysis (squares) and XRD curvature measurements (dashed line).

#### 5.4.2 Application to aging Sn film in a state of stress

The wafer-curvature method was applied to a Sn film of 3  $\mu\text{m}$  thickness (cf. section 5.3.1). The microstructure of the as electro-deposited Sn film is shown in the FIB micrograph presented in Fig. 5-2. A relatively small amount of an intermetallic compound (IMC) is present at the film/substrate interface as a result of an interfacial reaction between Sn and the thin Ni adhesion layer underneath (cf. section 5.3.1). The Sn film exhibits a predominantly columnar Sn microstructure of relatively large (lateral) grain size between typically 1 and 5  $\mu\text{m}$ . Such Sn films with predominantly columnar

Sn grains are known to be prone to Sn whisker formation upon stress introduction (see [12] and references therein).

Tin (Sn) whisker growth, i.e. the spontaneous formation of filamentary single crystals [20,21] on top of the Sn (film) surface by a solid state process, is known to be a stress relief process in the film and thus the occurrence (and rate) of whisker growth is closely related to the state of stress prevailing in such films [9,10,12,22,23].

Results of the XRD stress analyses obtained from the Sn/Si specimen during aging for 3 weeks at room temperature in a state of stress (imposed by the wafer curvature method) are shown in Fig. 5-6.

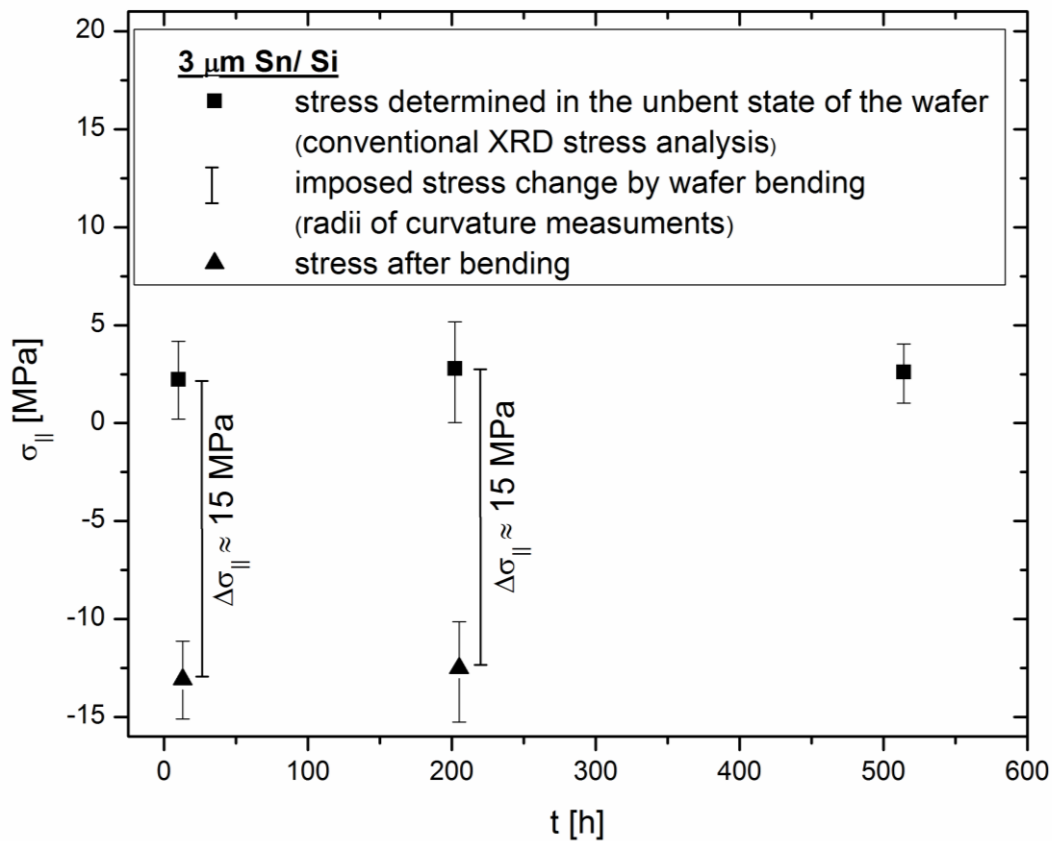


Fig. 5-6: Residual stresses ( $\sigma_{||}$ ) in the Sn film with  $3 \mu\text{m}$  thickness, determined at the surface close to the wafer center in the unbent state of the wafer (squares) and the (by wafer bending) imposed stress change ( $\Delta\sigma_{||}$ ), as function of aging time at room temperature.

The initial state of stress in the Sn film, i.e. before application of an external load by bending, was determined by conventional XRD stress analysis after the Sn/Si specimen had been stored for a few weeks under ambient conditions subsequent to the electro-deposition process. Significant changes of the intrinsic stress state due to stress-relaxation processes, triggered by e.g. the existence of a non-equilibrium state of the film which could have developed during manufacturing or by chemical reactions of the Sn film with the substrate material, especially with the very thin adhesion layers (see above), i.e. intermetallic compound formation, cannot occur at this point of time. In fact, an (over time) constant residual, initial tensile stress,  $\sigma_{||}$ , of about 2.5 MPa (cf. Fig. 5-6) was determined by application of the  $\sin^2\psi$ -method. The reported values of stress in the Sn film were determined exclusively close to the wafer centre, but measurements yielded identical results at several locations within a few millimeters from the wafer center.

Applying the wafer-curvature method developed in this project, the Sn/Si wafer was subjected (by evacuation of the glass pan; cf. Fig. 5-4) to an additional compressive stress of about -15 MPa (in the central region of the Sn film). Since slight tensile stresses (of ~2.5 MPa – see above) were present initially, an overall compressive stress close to the yield limit of Sn (see e.g. [24,25] was imposed by bending of the wafer (see the radii of curvature measurements indicated with triangles in Fig. 5-6; see also section 5.3.2).

Imposition of the compressive stress to the Sn coated Si wafer by the wafer-curvature method was maintained for a total of ~500 hours (~3 weeks). A short interruption of the bending experiment (i.e. venting of the glass pan and removing of the wafer from the glass pan) was made after approximately 200 hours of aging under load, in order to carry out a conventional XRD stress analysis. Subsequently, the load by bending was re-applied by evacuating of the glass pan and the Sn film was aged under compressive stress for an additional ~300 hours. After release of the load after an overall aging time of 500 hours, the state of stress in the Sn film was determined applying conventional XRD stress analysis (see Fig. 5-6).

The results of the conventional XRD stress analyses show that, once the acting load was released from the Sn film (i.e. the glass pan was vented), the initial tensile

stress of approximately 2.5 MPa in the Sn film occurred again (see the three data points, squares, in Fig. 5-6). Extensive FIB investigation of the Sn surface, carried out after the ultimate aging time of ~500 hours under the applied compressive load, revealed that whisker (or hillock) nucleation and growth had not occurred at all. This finding is discussed in the following.

It is usually claimed that Sn whisker growth on thin Sn films can occur as a response of the Sn film upon compressive stress introduction (see e.g. [16, 26-29]). However, recent research [9,10] has shown that, instead, the presence of negative stress gradients, in- and out-of plane with respect to the surface, as they develop during irregular, intermetallic compound formation in Sn/Cu specimens with columnar Sn grain morphology, build the driving force for Sn diffusion along grain boundaries and are essential for Sn whisker growth. Thus, even in the presence of tensile stress whisker formation can occur and has been observed (see discussion in [12]).

Only minor stress gradients in the in-plane direction (as can be seen from Fig. 5-4) as well as in out-of-plane direction, with respect to the surface, were introduced upon bending of the wafer: The in-plane stress gradient develops due to the inhomogeneous bending of the wafer as discussed in section 5.4.1, and the out-of-plane stress gradient develops because in principle, the imposed stress in the film material increases with increasing distance to the neutral axis of the Si wafer (c.f. section 5.4.1). However, these minor stress gradients, imposed in the Sn film by application of the wafer-curvature method, are negligible as compared to stress gradients developing in Sn films of whiskering Sn/Cu specimens (e.g.  $\sim 0.01$  MPa/ $\mu\text{m}$  versus  $\sim 10$  MPa/ $\mu\text{m}$  in the out-of-plane direction – cf. [9,12]), since the wafer thickness is much larger than the Sn film thickness.

The absence of whisker growth on the Sn film of the current study upon compressive stress introduction, due to bending of the Sn coated wafer, confirms that: (i) a compressive nature of the stress in the Sn film does not necessarily lead to whisker formation and (ii) in the absence of distinct (negative) stress gradients, no whisker formation takes place.

## 5.5 Conclusions

The wafer-curvature method provides an easy and controllable way for imposition of defined strain/stress states in thin films, deposited on (Si-)wafer substrates, by wafer bending. The experimental setup, consisting of a custom-made glass cylinder provided with a connection piece for vacuum tubes, a needle valve, a vacuum pump and a pressure gauge, allows the application of (in-situ) X-ray diffraction (XRD) techniques for detailed and non-destructive determination and tracing of the lattice strain in the externally stressed film.

Two independent X-ray diffraction techniques can be employed for the analysis of the (residual and) imposed stresses in the loaded thin films: i) conventional X-ray diffraction stress analysis (i.e. application of the well know  $\sin^2\psi$  method) utilizing reflections originating from the film material and ii) radii of curvature measurements applying rocking curve scans for reflections originating from the substrate material.

The wafer-curvature method was validated by application to a W film of 500 nm thickness. It was demonstrated that both, independent XRD techniques provide the same values for the state of imposed stress in the film. A minor stress gradient occurs parallel to the film surface, at distances remote from the centre of the wafer.

Application of the wafer-curvature method on a potentially whiskering Sn film of 3  $\mu\text{m}$  thickness, exhibiting a predominantly columnar microstructure, during aging at room temperature for three weeks under a defined load, inducing a pronounced, homogeneous compressive stress in the Sn film, close to the yield limit of Sn, did not lead to any whisker (or hillock) formation, thereby confirming that (negative) stress gradients are essential for inducing whisker (and hillock) formation.

## 5.6 References

- [1] P.G. Shewmon, *Diffusion in Solids* (John Wiley & Sons, McGraw-Hill, 2010).
- [2] F. C. Larche, J. W. Cahn, *Acta Metall.* 30, 1835-1845 (1982).
- [3] F. C. Larche, J. W. Cahn, *Acta Metall.* 33, 331-357 (1985).
- [4] Y. Kuru, M. Wohlschlägel, U. Welzel, E.J. Mittemeijer, *Thin Solid Films* 516, 7615-7626 (2008).
- [5] J. Sheng, U. Welzel, E.J. Mittemeijer, *Z. Krist. Suppl.* 30, 247-252 (2009).
- [6] J. Chakraborty, U. Welzel, E. J. Mittemeijer, *J. Appl. Phys.* 103, 113512 – 113512-15 (2008).
- [7] G.T. Galyon, *IEEE Trans. Electron. Packag. Manuf.* 28, 94-122 (2005).
- [8] NASA, Whisker Failures: <http://nepp.nasa.gov/whisker/failures/index.htm>.
- [9] M. Sobiech, M. Wohlschloegel, U. Welzel, E.J. Mittemeijer, W. Huegel, A. Seekamp, W. Liu, G.E. Ice, *Appl. Phys. Lett.* 94, 221901 (2009).
- [10] M. Sobiech, U. Welzel, E.J. Mittemeijer, W. Huegel, A. Seekamp, *Appl. Phys. Lett.* 93, 011906 (2008).
- [11] Y. Waseda, K. Hirata, M. Ohtani, *High Temp. High Pressures* 7, 221-226 (1975).
- [12] M. Sobiech, J. Teufel, U. Welzel, E.J. Mittemeijer, W. Huegel, *J. Electron. Mater.* 40, 2300-2313 (2011).
- [13] V. T. Deshpande, D. B. Sirdeshmukh, *Acta Crystallogr.* 14, 355-356 (1961).
- [14] U. Welzel, J. Ligot, P. Lamparter, A. C. Vermeulen, E. J. Mittemeijer, *J. Appl. Crystallogr.* 38, 1-29 (2005).
- [15] C. J. Smithells, E. A. Brandes, *Metal reference book*, (Butterworths London, 1976).
- [16] K. J. Martinschitz, E. Eiper, S. Massl, H. Kostenbauer, R. Daniel, G. Fontalvo, C. Mitterer, J. Keckes, *J. Appl. Crystallogr.* 39, 777-783 (2006).
- [17] A. Segmueller, I. C. Noyan, V. S. Speriosu, *Prog. Cryst. Growth Charact. Mater.* 18, 21-66 (1989).
- [18] U. Welzel, E.J. Mittemeijer, *Z. Krist.* 222, 160-173 (2007).
- [19] E.J. Mittemeijer, U. Welzel (Eds.): *Modern Diffraction Methods*, (Wiley-VCH, Weinheim, 2012).
- [20] K.G. Compton, A. Mendizza, S. M. Arnold, *Corrosion* 7, 327–334 (1951).
- [21] C. Herring, J. K. Galt, *Phys. Rev.* 85, 1060-1061(1952).
- [22] R. R. Hasiguti, *Acta Metal.* 3, 200-201 (1955).
- [23] B. Z. Lee, D. N. Lee, *Acta Metal.* 46, 3701 –3714 (1998).
- [24] W. F. Gale, *Smithells Metals Reference Book*, (Butterworths, London, 2004).
- [25] L. Taylor, *Metals Handbook, Properties and Selection: Nonferrous Alloys and Special-Purpose Materials*, American Society for Metals, (Metals Park, Ohio, 1990).
- [26] G. Galyon, L.Palmer, R. Gedney, *Global SMT & Packaging*, 10-14 (2005).
- [27] S.-K. Lin, Y. Yorikado, J.-X. Jiang, K.-S. Kim, K. Suganuma, S.-W. Chen, M. Tsujimoto, I. Yanada, *J. Mater. Res.* 22, 1975-1986 (2007).
- [28] S.-K. Lin, Y. Yorikado, J.-X. Jiang, K.-S. Kim, K. Suganuma, S.-W. Chen, M. Tsujimoto, I. Yanada, *J. Electron. Mater.* 36, 1732-1734 (2007).
- [29] J. Liang, Z.-H. Xu, X. Li, *J. Mater. Sci.: Mater. Electron* 18, 599-604 (2007).

## Chapter 6

### 6 *The crystallographic growth directions of Sn whiskers*

J.Stein<sup>1,2</sup>, U. Welzel<sup>1</sup>, A. Leineweber<sup>1</sup>, W. Huegel<sup>2</sup> and E.J. Mittemeijer<sup>1,3</sup>

<sup>1</sup> Max Planck Institute for Intelligent Systems (formerly Max Planck Institute for Metals Research), Heisenbergstr. 3, 70569 Stuttgart (Germany)

<sup>2</sup> Robert Bosch GmbH, Automotive Electronics / Engineering Assembly Interconnection Technology (AE/EAI2), Robert-Bosch-Str. 2, 71701 Schwieberdingen (Germany)

<sup>3</sup> University of Stuttgart, Institute for Materials Science, Pfaffenwaldring 55, 70569 Stuttgart (Germany)

Key words: Sn whisker, electron back scattered diffraction, single crystal growth, crystallographic growth direction

#### **6.1 Abstract**

The growth directions of 55 Sn whiskers, i.e. the crystallographic orientation parallel to the whisker-growth axes, were determined using (i) a focused ion beam microscope for the determination of the physical growth angles of the whiskers with respect to a specimen (reference) coordinate system and (ii) an electron back scatter detector (EBSD) in a scanning electron microscope for the determination of the crystallographic orientation of the whiskers. The Sn whiskers were found to grow preferentially along low-index directions of the  $\beta$ -Sn crystal structure. The experimental findings of this study (and most of the results presented in the literature as well) were explained by applying, in a modified way, the Hartman-Perdok concept of periodic bond chains, i.e. chains of strong bonds running uninterruptedly through the structure, to the Sn whisker-growth phenomenon.

## 6.2 Introduction

The formation of Sn whiskers on top of thin Sn films has attracted great scientific interest for now more than 60 years [1,2]. It has been generally accepted that the growth of these filamentary, usually single-crystalline [3,4] Sn needles is related to acting (residual) stresses inside the film material (see e.g. [5-11]). Formation of intermetallic compounds inside the Sn at the film/substrate interface and/or with an alloying element at grain boundaries [5, 13-16] or by externally applied stresses [17-21] are probably the most frequently reported (stress-introduction) mechanisms known to induce Sn whisker growth. Further it has been reported that stresses induced by corrosion [22-24], intrinsic stresses originating from the deposition process [12] and imposed stresses (in the Sn film) during temperature cycling of specimens where film and substrate material show a large difference of the thermal expansion coefficients [25] can lead to the formation of Sn whiskers.

It has been often suggested that the presence of an *overall compressive* stress state inside the Sn film is a necessary condition for Sn whisker growth (see e.g. [26,27]). However, just recently, it was shown experimentally by investigations on electro-deposited pure Sn films, with a predominantly columnar microstructure, on copper substrates [7,8], that, in fact, the development of in-plane and out-of-plane stress *gradients* in the film, which can develop as a result of the irregular formation of  $\text{Cu}_6\text{Sn}_5$  during aging of the specimens at room temperature at the film/substrate interface [5, 13-15], are responsible for Sn whisker growth. These stress-gradients provide the basis, i.e. the driving force, for stress-driven Sn diffusion via a Coble type creep mechanism [28] towards the whisker root (for discussion see Ref. [29]).

Even though several Sn whisker-mitigation strategies have been developed (e.g. deposition of thin Ni-layers between Sn film and Cu substrate as Cu-diffusion barrier [30-32], the application of heat treatments after film deposition [5,33-34] or the usage of (lead-free) Sn-alloy films containing e.g. Ag or Bi, instead of pure Sn films [35-38]), the formation of Sn whiskers is still considered as a severe reliability issue in the microelectronics industry: Sn whiskers, which can grow up to several millimeters [39], are able to bridge the fine gaps of neighboring conductors of electronic components,



thereby possibly leading to failures in electronic applications (such as engine control units, etc...) [1,40].

In order to mitigate Sn whisker growth under all circumstances, a total understanding and corresponding model of the whisker-growth phenomenon is necessary. However, a large variety of parameters influencing Sn whisker growth has been demonstrated to exist and this situation so far has not led to such a complete model.

Against this background, this work focuses on the crystallographic growth directions of Sn whiskers, i.e. the directions parallel to the whisker axes, as representative of the growth mechanism. To this end Sn whiskers, which grow from the surface of pure Sn films electro-deposited on pure Cu substrates during room temperature storage, were investigated. Growth directions of Sn whiskers were previously determined in the literature applying e.g. transmission electron microscopy (TEM) or electron back scattered diffraction techniques, (EBSD; see [41,42] and references therein). However, a satisfactory explanation for the observed growth directions in the crystal frame of reference of  $\beta$ -tin (tetragonal, space group:  $I4_1/amd$ , with lattice parameters  $a = b = 5.82 \text{ \AA}$  and  $c = 3.18 \text{ \AA}$ ), has not been given until now. It will be shown in the following that the experimental findings of this study, and most of the results presented in the literature as well, can be well explained applying the concept of *periodic bond chains* (PBCs) in a modified way. The consideration of the role of chains of strong bonds, PBCs, running uninterruptedly through the crystal structure, was originally introduced by Hartman and Perdok [43,44], who applied these PBCs to estimate the surface energies for different  $hkl$  planes of the crystal and thus to determine the (emergence of specific) crystal faces upon its growth.

## ***6.3 Experimental***

### **6.3.1 Specimen preparation and analysis methods**

Pure thin Sn films, with a thickness of  $\sim 3 \mu\text{m}$  were electroplated on pure Cu substrates (dimensions:  $2.5 \text{ cm} \times 1.5 \text{ cm} \times 1 \text{ mm}$ ) at room temperature using a commercial “matte-

tin” electrolyte on the basis of methasulfonic acid with organic additives and dissolved metal ions applying a current density of 1.5 A/dm<sup>2</sup>. The substrates were ultrasonically cleaned in acetone and deionized water and surface activated prior to the deposition process by dipping in 10%-(H<sub>2</sub>SO<sub>4</sub>)<sub>aq</sub> for a few minutes. The thickness and microstructure of the Sn films were determined employing focused ion beam (FIB) microscopy images of cross sections prepared with a FEI Novo 600 NanoLab focused ion beam workstation using an acceleration voltage of 30 kV and beam currents between 11 and 1000 pA for cutting and imaging. The grain morphology of these films is predominantly columnar, i.e. most of the grain boundaries are oriented perpendicular to the surface of the film, with in-plane grain sizes between ~1 and 5 μm.

After Sn-film deposition the Sn/Cu specimens were stored at room temperature without controlling the ambient conditions. After several weeks of storage, numerous whiskers (and hillocks) with a large variety of lengths and appearances, i.e. straight, kinked and/or curled, had grown on top of the surface.

Pole figures were measured employing a Philips (now: PANalytical) MRD Pro diffractometer with parallel-beam geometry using Cu-K<sub>α</sub> radiation with a beam size of 4×4 mm<sup>2</sup>. The diffractometer was equipped with a conventional sealed Cu tube (operating at 45 kV/ 40 mA) as x-ray source, a polycapillary x-ray lens to realize parallelization of the x-rays, an Eulerian cradle (four-circle goniometer) which allows rotating and tilting of the specimen, a parallel foils collimator and a flat graphite monochromator as secondary optics, as well as a proportional counter for x-ray detection. The Sn films showed a predominant {321} fiber texture.

The whisker-growth directions in the specimen and crystallographic frames of reference were determined applying a focused ion beam microscope (see above) in combination with a scanning electron microscope (SEM), LEO 438 VP, which is additionally equipped with an electron backscatter diffraction (EBSD) system (TSL, EDAX, Inc.). The EBSD data were analyzed utilizing the OIM 4.5 software.

### 6.3.2 Approach for the analysis of the Sn whisker-growth directions

For the analysis of Sn whisker-growth directions, only straight whiskers with a constant periphery, i.e. without any broadenings, diminutions or kinks in the whisker, were used. The approach employed involved three steps:

(i) The orientation of the whisker was determined relative to a reference coordinate system (i.e. the specimen frame of reference) by evaluation of the growth angles  $\alpha$  and  $\beta$ :  $\alpha$  is the angle between the y-axis of the reference coordinate system and the projection of the whisker on the specimen surface (see Fig. 5-1 a);  $\beta$  is the angle between the z-axis of the reference coordinate system (i.e. the specimen-surface normal) and the whisker axis (see Fig. 5-1 a).

A FIB microscope was used for evaluation of the growth angles  $\alpha$  and  $\beta$  since the stage of this FIB microscope can be easily adjusted to the eucentric height, i.e. tilting of the stage then is possible without losing sight of the whisker in focus since the axis of tilting lies in the surface of the specimen. The reference coordinate system was marked with help of FIB marks, i.e. small trenches were cut by FIB milling; see blue lines in Fig. 5-1. The z-axis of the specimen (reference) coordinate system is parallel to the specimen normal and (in the initial configuration) parallel to the detector axis. In Fig. 5-1 a), the FIB frame of reference ( $x'$ ,  $y'$ ,  $z'$  -axes) coincides with the specimen frame of reference.

In order to determine the growth angle  $\alpha$ , the specimen stage (with the specimen on top) was rotated around the specimen normal (i.e. around the  $z=z'$ -axis - see Fig. 5-1 a) such that the whisker is oriented perpendicular to the tilting axis of the FIB stage ( $x'$ -axis in Fig 5-1 b). Subsequently, in order to determine the growth angle  $\beta$ , the specimen stage was tilted around the  $x'$ -axis, (see Fig. 5-1 b) such that the whisker growth axis (i.e. the whisker rod) becomes parallel to the detector axis ( $=z'$ -axis), i.e. only the whisker tip is then visible in the FIB image.

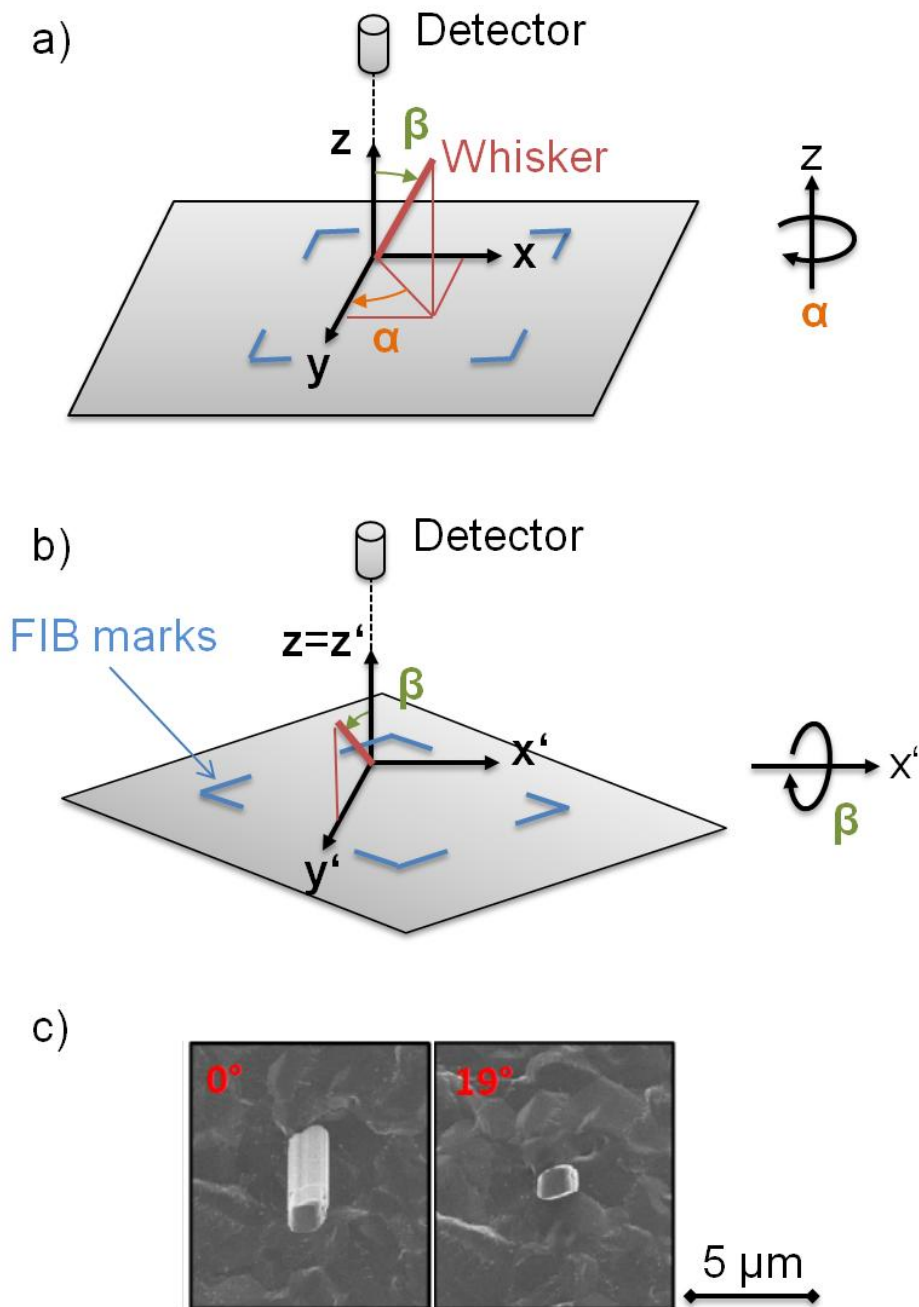


Fig. 5-1: Sketches in a) and b) indicate the approach for analysis of the physical growth angles  $\alpha$  and  $\beta$  of a whisker (indicated as red line) with respect to a specimen (reference) coordinate system,  $x/y/z$ , which was marked with help of FIB marks (blue lines) using a focused ion beam microscope (see text in section 6.3.2). In the initial configuration (a), the FIB coordinate system,  $x'/y'/z'$ , equals the specimen (reference) coordinate system. c) Exemplary FIB image of a whisker, after rotation around the specimen normal such that the whisker is oriented perpendicular to the tilting axis,  $x'$ , of the FIB stage at a tilting angle  $0^\circ$  (left hand image). Tilting the stage by a tilting angle of  $19^\circ$ , only the whisker tip is visible (right hand image), i.e. the whisker length-axis is then parallel to the detector axis.

Exemplary FIB images of a whisker after rotation around the specimen normal such that the whisker is oriented perpendicular to the tilting axis of the FIB stage is shown in Fig. 5-1 c (left hand image) with a tilt angle  $=0^\circ$ . After tilting of the specimen over  $19^\circ$  the whisker is parallel to the detector axis and only the whisker tip is then visible (see Fig. 5-1c, right hand image).

(ii) Subsequently, after moving the specimen on the specimen holder to the SEM, the crystallographic orientation of the whisker grain was determined by application of the EBSD method, i.e. the orientation of the crystal frame of reference of the whisker grain was determined relative to the chosen reference (specimen) coordinate system (see above).

(iii) Since the orientation of the whisker axis relative to the specimen frame of reference (see step (i)) as well as the orientation of the crystal coordinate system of the whisker grain relative to the specimen frame of reference (see step (ii)) now were known, the crystallographic orientation of the whisker-grain axis, i.e. the crystallographic whisker-growth direction, could be determined, i.e. the direction  $(\alpha, \beta)$  could now be defined in the crystal frame of reference. To this end, a rotation of the so-called orientation matrix (see e.g. Ref. [39] for a more detailed description) was performed applying the EBSD data software.

## **6.4 Results**

The whisker-axis directions of 55 whiskers were determined and indicated as black circles in the whisker-axis inverse pole-figure shown in Fig. 5-2. An accumulation of the data points in Fig. 5-2 occurs at a number of specific low-index directions: 26 whiskers show a whisker-axis direction close to  $\langle 100 \rangle$ , 12 whiskers close to  $\langle 101 \rangle$  and 8 whiskers close to  $\langle 111 \rangle$ . A few Sn whiskers were found with whisker-axis directions parallel (close) to  $\langle 201 \rangle$  and  $\langle 102 \rangle$  (see also Table 6-1). The growth directions of only 4 whiskers (also indicated in Fig. 5-2) could not be associated with any low-index direction.

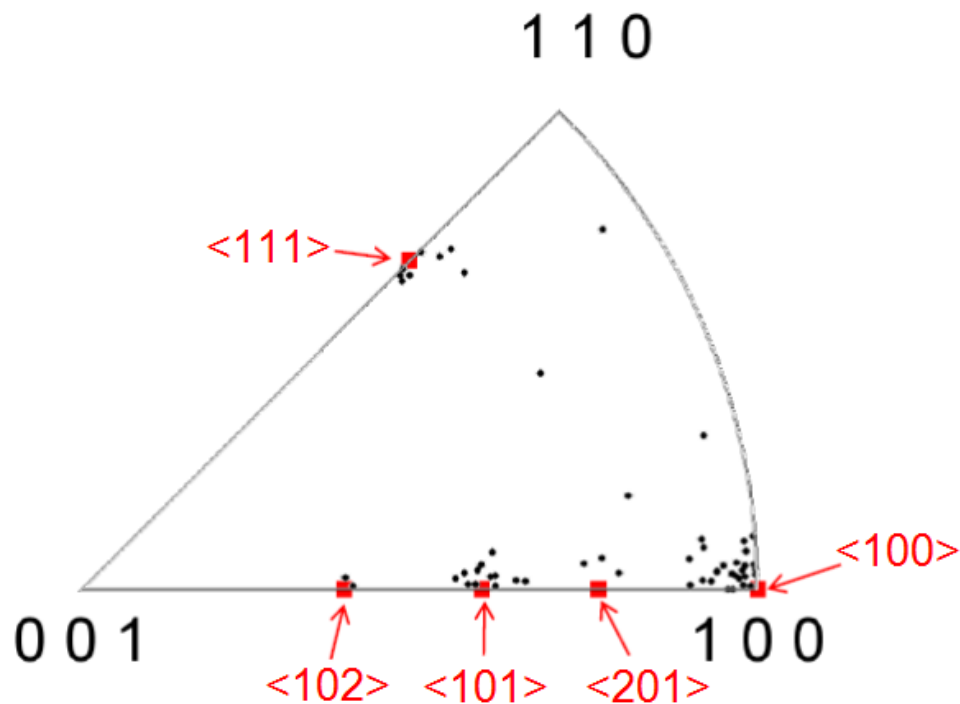


Fig. 5-2: Whisker-axis inverse pole figure of  $\beta$ -tin with the crystallographic orientations of the axes of the 55 evaluated whiskers, indicated as black circles. Most data points accumulate around low-index directions (red squares). The results are presented in the so-called stereographic triangle pertaining to the (001) stereographic projection for tetragonal ( $\beta$ -Sn) crystals.

Even though it is obvious from Fig. 5-2 that the data points accumulate at certain low-index directions (indicated with red squares in Fig. 5-1), scatter of data points around these directions occurs. This scatter is most likely due to experimental errors, such as measurement errors when determining the growth angles  $\alpha$  and  $\beta$  (see section 6.3.2) using the FIB microscope and/or alignment inaccuracy of the specimen stage in the frame of reference of the scanning electron microscope. Furthermore, execution of the marking of the specimen frame of reference via FIB milling (cf. section 6.3.2) and the (subsequent) determination of the crystal orientation of the whisker grain in the crystal frame of reference via the EBSD method could not be performed within the same day (usually 2-4 days were needed). Since it is known that Sn whiskers can rotate while growing [45, 46], thereby changing their orientation with respect to the specimen frame of reference, it appears possible that in a few cases the whisker-axis directions presented in the inverse pole figure are incorrect. This might explain the deviating

whisker-axis directions observed for the 4 whiskers which apparently do not comply with a low-indexed direction (see above).

Tab. 6-1: List of all non-equivalent translation vectors for the  $\beta$ -Sn crystal structure smaller than / approximately 15 Å, indicated by their crystallographic direction (u, v, w) and length (see column no. 1). Column no. 2: Numbers of strong bond vectors, necessary to build one building unit for a periodic bond chain, when considering only the “ $a/2 \pm c/4$ ” and/or “ $b/2 \pm c/4$ ” bonds as strong bonds. Column no. 3: Number of strong bond vectors, necessary to build one building unit for a periodic bond chain when considering the “ $a/2 \pm c/4$ ”, “ $b/2 \pm c/4$ ” bonds and/or the “c” bonds as strong bonds. The numbers of whiskers of specific growth directions, as determined experimentally in this study, have been given in column no. 4.

length [Å]	u	v	w	PBC vector	a/2±c/4 or b/2±c/4	a/2±c/4 or b/2±c/4	and c		experimentally determined in this work
					<201>	<201>	<001>	Total	
3.18	0	0	1	= <001>	4	0	1	1	
4.41	0.5	0.5	0.5	= 0.5 <111>	2	2	0	2	8
5.82	1	0	0	= <100>	2	2	0	2	26
6.3	0.5	0.5	1.5	= 0.5 <113>	6	2	1	3	
6.36	0	0	2	= 2 <001>	no new direction				
6.63	1	0	1	= <101>	4	2	1	3	12
8.23	1	1	0	= <110>	4	4	0	4	
8.62	1	0	2	= <102>	8	2	2	4	2
8.82	1	1	1	= <111>	no new direction				
8.95	0.5	0.5	2.5	= 0.5 <115>	10	2	2	4	
9.34	1.5	0.5	0.5	= 0.5 <311>	4	4	0	4	
10.37	1.5	0.5	1.5	= 0.5 <313>	8	4	1	5	
11.18	1	0	3	= <103>	14	2	3	5	
11.87	0.5	0.5	3.5	= 0.5 <117>	14	2	3	5	
12.07	2	0	1	= <201>	6	4	1	5	3
12.45	1.5	1.5	0.5	= 0.5 <221>	6	6	0	6	
13.99	1	0	4	= <104>	16	2	4	6	
15.15	1	1	4	= <114>	16	4	3	7	

## 6.5 Discussion

### 6.5.1 Relevance of periodic bond chains for whisker growth

The observation that Sn whiskers grow with their length axes preferentially along certain directions of the  $\beta$ -tin crystal structure (see section 6.4) is compatible with most literature reports (see Refs. [42, 47] and references therein). In particular, the  $\langle 100 \rangle$ ,  $\langle 101 \rangle$ ,  $\langle 111 \rangle$  directions have been determined in this work as preferential whisker-axes directions (in agreement with most literature reports), but also the  $\langle 001 \rangle$  direction has been identified as such (see e.g. [5,48-55]). A satisfying explanation/model for these findings has not been given yet.

It has been noted that (some of the) preferred whisker-axis directions are either glide directions ( $\langle 001 \rangle$ ,  $\langle 101 \rangle$ ) or second and third most densely packed directions ( $\langle 111 \rangle$ ,  $\langle 100 \rangle$ ) [47,56]. However, the present study (cf. section 6.4) and also other investigations [42,47] have shown that additional preferential whisker-axis directions occur as well.

Various mechanisms for whisker growth based on dislocations have been proposed (see e.g. [47] and references therein), all involving dislocations meeting the surface with a component of the Burgers vector normal to the surface. Thus, such mechanisms are in general able to explain the finding that Sn whiskers grow along certain directions. However, some of these proposed models were controversially discussed in the literature [47] since experimental observations (such as that whiskers grow from the base and not from the tip and the lack of experimental proof for the presence of dislocations inside the whisker) are incompatible with these models.

In this work, it is proposed to apply, in a modified way, the concept of periodic bond chains (PBCs) to the Sn whisker-growth phenomenon in order to explain the experimentally observed growth directions. PBCs are chains of strong bonds running uninterruptedly through the crystal structure. A chain of strong bonds can be subdivided in building units: a building unit represents the minimal amount of atoms/bonds necessary to build a repetition unit of the PBC; the starting and end points (e.g. an atom) of a building unit define the periodic bond chain vector.



The notion of PBCs was originally introduced by Hartman and Perdok [43,44]. They proposed to relate the crystal morphology with the crystal structure via PBCs to find out which crystal faces predominate the habitus of a (freely growing, single) crystal. These crystal faces are identified as so-called F(flat)-faces which contain at least two coplanar periodic bond chain vectors. The so-called S(steped)-faces, are faces containing one periodic bond chain vector, and the so-called K(kinked)-faces do not contain any periodic bond chain vector and are least important for controlling the crystal morphology: Hartman and Perdok consider the attachment energy of a crystal face, i.e. the energy released upon attaching a building unit (e.g. an atom) on a surface of the growing crystal as the indicating value for the importance of that crystal face for the crystal morphology. For the attachment of a building unit *on top* of an F-face (which is flat and would lead to the displacement of that face as a crystal face; see Fig. 2 in Ref. [43]) only attachment energy corresponding to extension of a PBC/PBCs with PBC vector(s) not lying in the plane of the F-face is released. Adding a building unit to the edge of a step of an S-face is associated with the formation of at least one more strong bond than in the case of an F-face and adding a building unit into a kink of a K-face is associated with the formation of at least one more strong bond than in the case of an S-face (see Fig. 2 in Ref. [43]). Hence, adding a building unit to S- or K-faces releases more attachment energy, as compared to adding a building unit to a flat F-face.

Now, adopting the notion that fastest growth occurs on those faces where most energy is released upon attachment of a building unit and recognizing that the crystal morphology is (eventually) controlled by the faces experiencing slowest growth on top of them, it follows that the F-faces will dominate the crystal morphology and that the K-faces are often not observed [43,44].

For the case of Sn-whisker growth, the Hartman and Perdok theory can only be applied partially. A Sn whisker grain, due to its solid-state growth mechanism, cannot grow freely in all three dimensions (as holds for a single crystal growing from the liquid during a solidification process by homogeneous nucleation, which is the case where the Hartman-Perdok theory has been applied most often): In the electro-deposited pure Sn films of this study, with a predominantly columnar Sn grain morphology (cf. section 6.3.1), so-called surface grains occur: relatively small grains located at the Sn film

surface having grain boundaries inclined with respect to the surface. From these surface grains Sn whiskers grow by solid-state diffusion. Due to acting stress gradients inside the Sn film, Sn diffusion, via a Coble type creep mechanism [19], takes place predominantly towards the surface in order to relieve stress, initiating and supporting Sn whisker formation and growth [29] (cf. section 6.2). It follows that Sn whiskers grow from the base, i.e. from the grain boundaries of the whiskering surface grain located inside the Sn film (see blue lines in Fig. 5-3, indicating inclined grain boundaries of a surface grain/whisker). Therefore, the morphology of the periphery of the whisker rod, (i.e. the (cross-)sectional area of the whisker when cut normal to the whisker growth axis) is determined by the neighboring grains of the whiskering surface grain. Hence, the whisker grain cannot grow freely in all dimensions provided the Sn grain boundaries inside the Sn film are immobile (see Fig. 5-3). Consequently, planar crystal faces, F-faces, bounding the whisker surface parallel to its length axis are not formed. If this would occur yet, then all crystal faces, bounding the whisker, would share one direction (=zone axis for these faces): The direction of the whisker axis, which is likely the direction of a PBC shared by all these F faces (which as F planes each would have at least a second PBC; see above). It is now proposed that upon whisker growth, albeit these bounding F-faces cannot form because of the constraining neighboring grains, the whisker axis yet does run in the direction of a PBC as a consequence of the strived for morphology.

The strong bonds of the PBCs in the  $\beta$ -Sn structure can be defined upon taking a close look at the coordination of the Sn atoms in its crystal structure (Fig. 5-4). One Sn atom has four nearest neighbor atoms: Each of these is located in a  $\langle 201 \rangle$  direction at a distance of 3.023 Å. These Sn-Sn bonds can be represented by interatomic vectors “ $\mathbf{a}/2 \pm \mathbf{c}/4$ ” or “ $\mathbf{b}/2 \pm \mathbf{c}/4$ ” connecting the pairs of nearest neighbors Sn atoms (centered atom and nearest neighbor atoms; see blue bonds in Fig. 5-4 and cf. Table 6-1). This Sn-Sn bond type is considered as the strongest bond in the  $\beta$ -Sn structure (Note that the chemical bonding of  $\beta$ -Sn has a partially covalent nature). The distance between neighboring Sn atoms in a  $\langle 001 \rangle$  direction (interatomic vector “ $\mathbf{c}$ ”) is only slightly longer: 3.18 Å. Therefore, the  $\langle 001 \rangle$  bonds have to be considered as strong bonds as well. The “ $\mathbf{c}$  bond” can be represented by a linear combination of “ $\mathbf{a}/2 \pm \mathbf{c}/4$ ” or “ $\mathbf{b}/2 \pm \mathbf{c}/4$ ” bonds (see below).

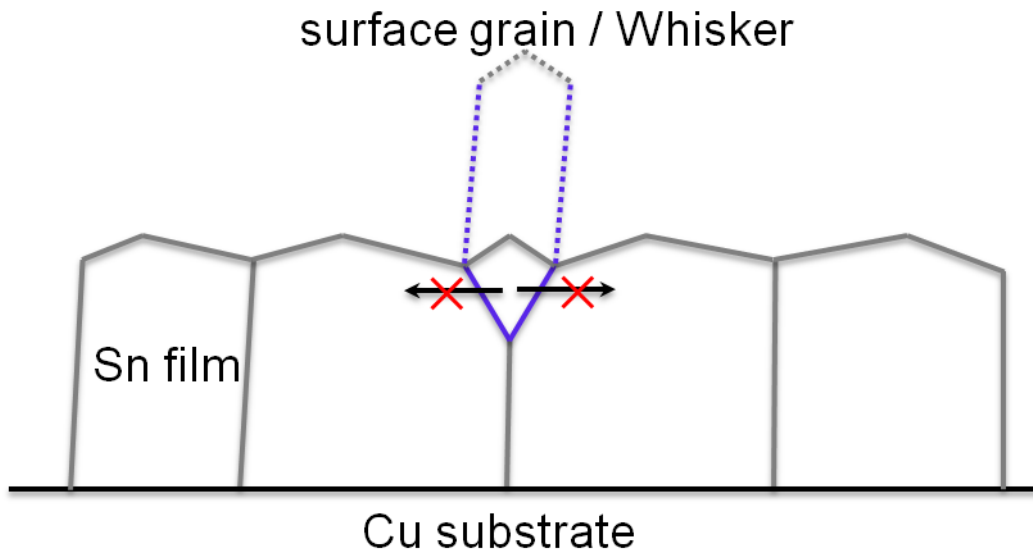


Fig. 5-3: 2D-sketch of a surface grain with inclined grain boundaries, with respect to the surface, (blue solid lines) which can grow to a Sn whisker (dotted lines). If the inclined grain boundaries of a surface grain in the Sn film are immobile, the morphology of the periphery of the whisker rod, (i.e. the (cross-)sectional area of the whisker when cut normal to the whisker growth axis) is determined by the neighboring grains of the whiskering surface grain.

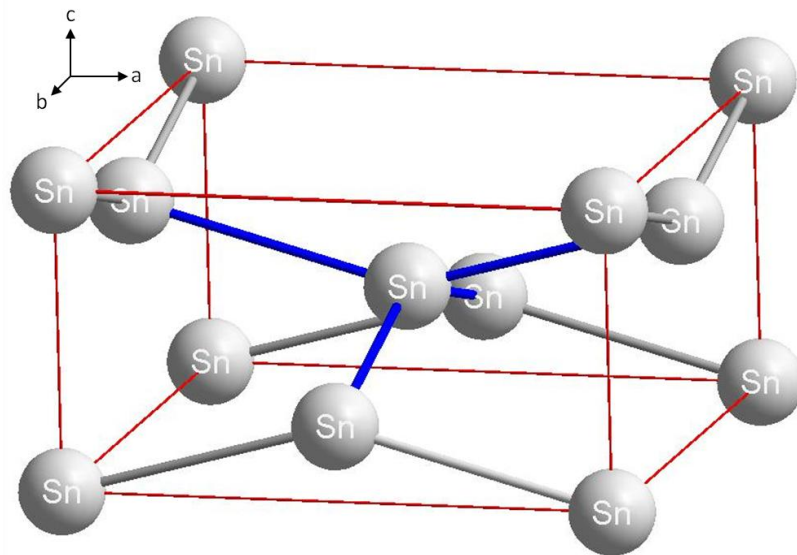


Fig. 5-4: Unit cell of the crystal structure of  $\beta$ -tin (tetragonal, space group:  $I4_1/amd$ , lattice parameters  $a=b=5.82 \text{ \AA}$  and  $c=3.18 \text{ \AA}$ ). One Sn atom is surrounded by four nearest neighbors, each located in a  $\langle 201 \rangle$  direction at a distance of  $3.023 \text{ \AA}$ . These “ $a/2 \pm c/4$ ” or “ $b/2 \pm c/4$ ” bonds (blue bonds) are the shortest pair bonds in the  $\beta$ -Sn structure.

A necessary condition for a periodic bond chain is that it runs uninterruptedly through the crystal structure. Thus, a repetition unit of a periodic bond chain (i.e. the sequence of strong bonds necessary for one period of a PBC) must correspond with a translation vector in the  $\beta$ -Sn crystal structure.

All non-equivalent translation vectors for the  $\beta$ -Sn crystal structure have been listed in Table 6-1 for vector lengths smaller than approximately 15 Å, with their crystallographic direction and length (column no. 1). All these translation vectors can be expressed as a linear combination of “ $\mathbf{a}/2 \pm \mathbf{c}/4$ ” or “ $\mathbf{b}/2 \pm \mathbf{c}/4$ ” strong bond vectors. The number of “ $\mathbf{a}/2 \pm \mathbf{c}/4$ ” and/or “ $\mathbf{b}/2 \pm \mathbf{c}/4$ ” bond vectors, necessary to build one repetition unit for a periodic bond chain, has been indicated, when considering only bonds of the Sn pairs separated by “ $\mathbf{a}/2 \pm \mathbf{c}/4$ ” and/or “ $\mathbf{b}/2 \pm \mathbf{c}/4$ ” as strong bonds in Table 6-1 (column no. 2). Some examples of these periodic bond chains (i.e. the repetition units) are shown in Figs. 5-5 and 5-6.

Similarly, the number of strong bonds, necessary to form a repetition unit for a periodic bond chain when considering additionally the bonds of Sn-Sn pairs separated by “ $\mathbf{c}$ ” bonds as strong bonds (see above), have been evaluated and indicated as well in Table 6-1 (column no. 3).

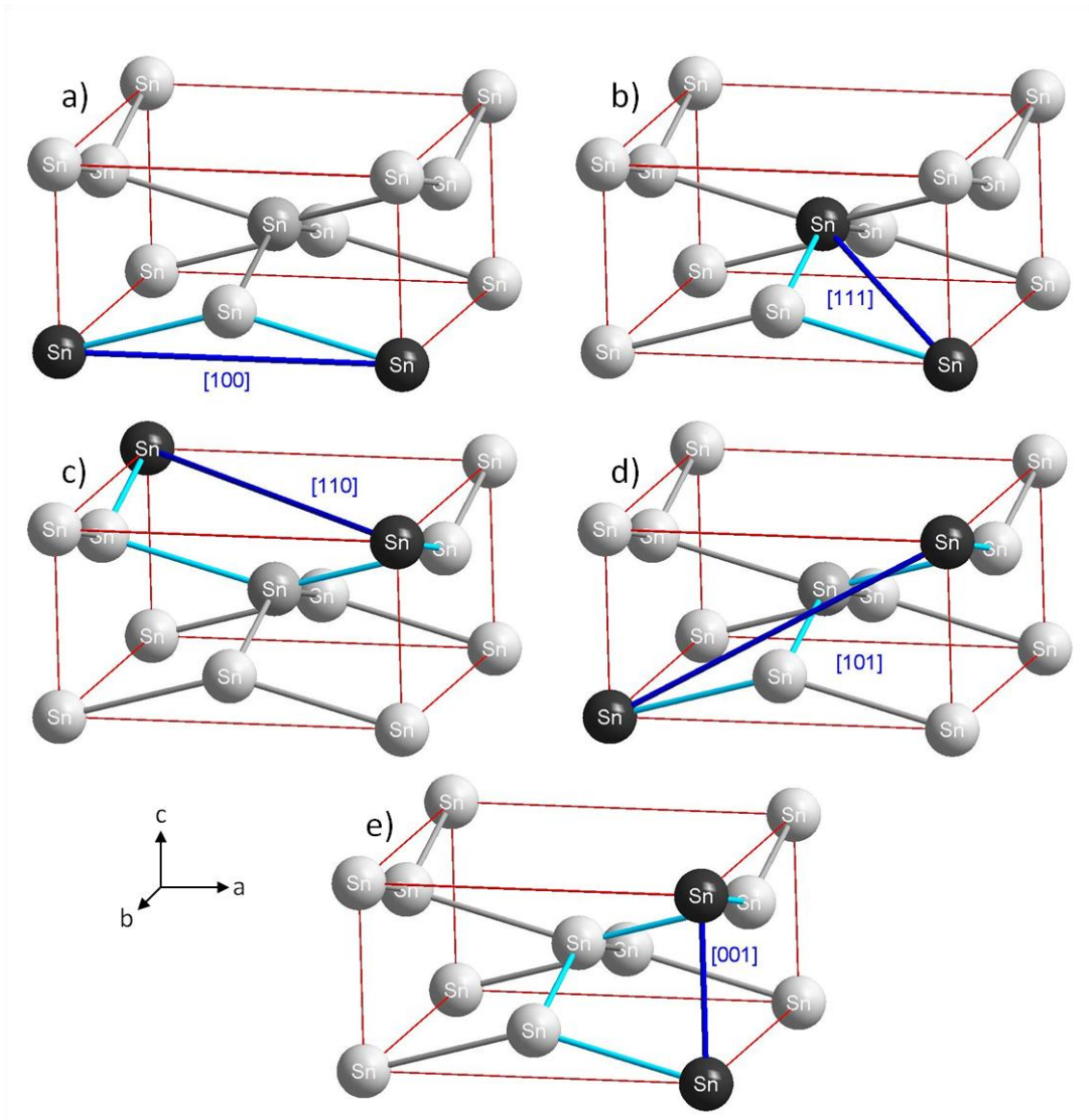


Fig. 5-5: Repetition units of periodic bond chains (see light blue bonds) along the (a) [100], (b) [111], (c) [110], (d) [101], and (e) [001] directions (dark blue lines represent the corresponding PBC vectors (translation vectors)) when considering only the " $a/2 \pm c/4$ " or " $b/2 \pm c/4$ " bonds as strong bonds.

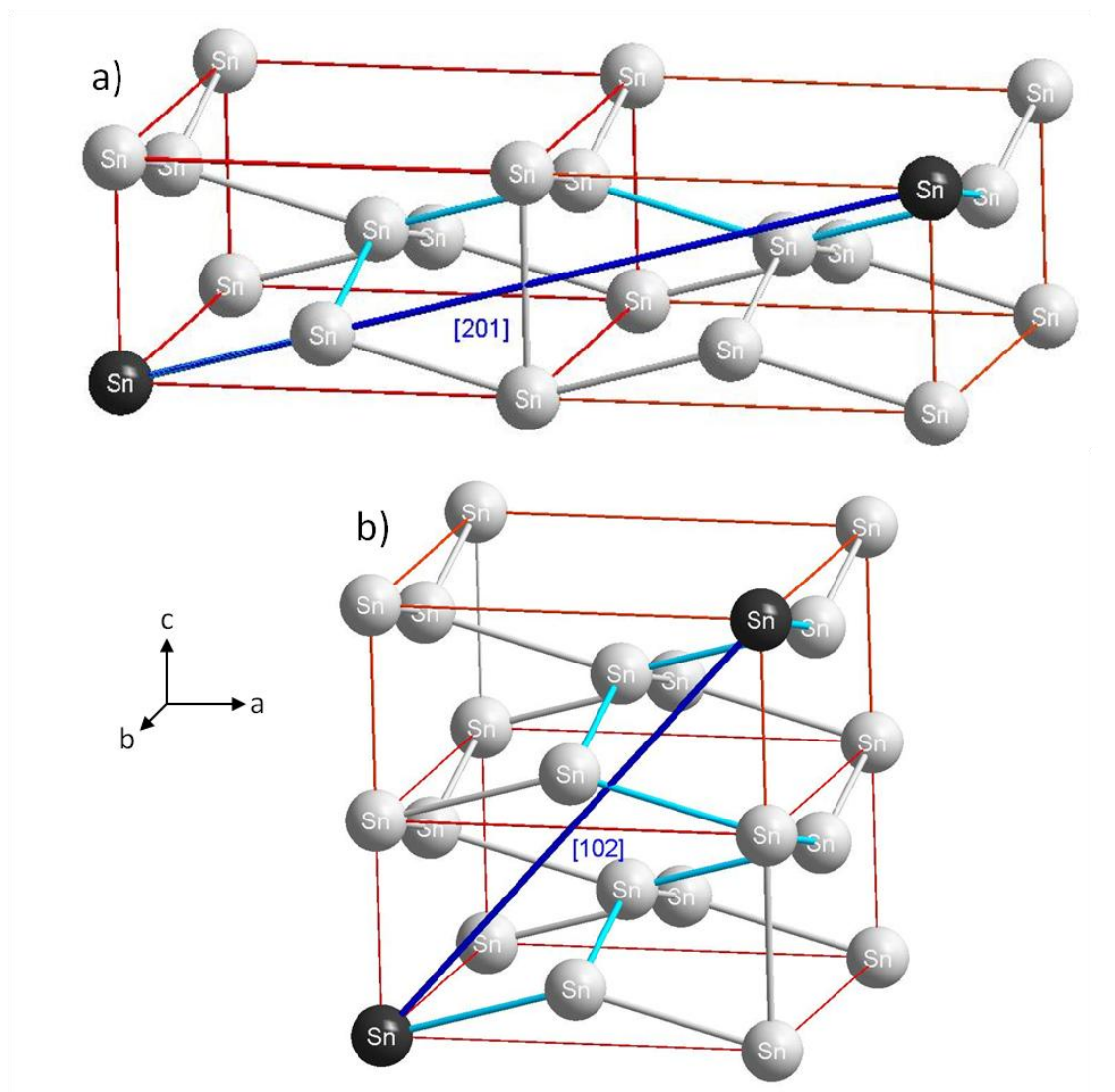


Fig. 5-6: Repetition units of periodic bond chains (see light blue bonds) along the (a) [102] and (b) [201] directions (dark blue lines represent the corresponding PBC vectors (translation vectors)) when considering only the “ $a/2 \pm c/4$ ” or “ $b/2 \pm c/4$ ” bonds as strong bonds.

### 6.5.2 Comparison with experimental results

All, but four, whisker-growth directions observed in this study, are parallel to periodic bond chain vectors (cf. section 6.4, Table 6-1). The numbers of strong bonds, necessary to build one building/repetition unit of the periodic bond chains, are different for the different PBCs, i.e. some PCBs require only a small amount of strong bonds, other PBCs require a relatively large number of strong bonds: The experimental results of this study show that the repetition units of the PBCs parallel to the very frequently found

growth directions (i.e. the  $\langle 100 \rangle$ ,  $\langle 101 \rangle$  and  $\langle 111 \rangle$  directions) consist of only a few (2 or 4) strong bonds. The repetition units of the PBCs along less often found whisker-growth directions (the  $\langle 201 \rangle$  and  $\langle 102 \rangle$  directions) consist of 6 or 8 such strong bonds.

It is proposed that the preference of PBCs with a relatively small number of strong bonds to form a repetition unit is a consequence of growth kinetics, as less complicated atomic arrangements are required to establish those PBCs.

A comparison can be made between the case that only the “ $\mathbf{a}/2\pm\mathbf{c}/4$ ” and/or “ $\mathbf{b}/2\pm\mathbf{c}/4$ ” bonds are considered as strong bonds and the case that additionally also the “ $\mathbf{c}$ ” bonds are considered as strong bonds. As follows from comparison of these two cases with the experimental results in Table 6-1, only considering the “ $\mathbf{a}/2\pm\mathbf{c}/4$ ” and/or “ $\mathbf{b}/2\pm\mathbf{c}/4$ ” as strong bonds provides the more outspoken distinction between observed and non-observed growth directions.

PBCs with repetition units comprising a small number of strong bonds ( $\leq 4$ ) which were not observed in this study are those along  $\langle 001 \rangle$  and  $\langle 110 \rangle$  directions. Strikingly, these whisker-growth directions have been observed in other work (see [42] for a comprehensive literature review). The non-observance of all possible whisker-growth directions in a single study, as this one, can be a consequence of limited statistics. Only straight Sn whiskers, within a certain range of lengths and growth angles (with respect to the surface), were selected, owing to experimental handling reasons (cf. also section 6.3.2). Furthermore, the film texture may influence the overall distribution of the Sn whisker-growth directions as well [42].

## 6.6 Conclusions

- The crystallographic growth directions of 55 straight growing Sn whiskers were determined employing a focused ion beam microscope, for the evaluation of the physical growth angles of a whisker with respect to a specimen frame of reference, and a scanning electron microscope equipped with a EBSD detector, for the evaluation of the orientation of the whisker grain with respect to the crystallographic frame of reference.

- The experimental findings of this study (and most of the results presented in the literature as well) can be explained applying the concept of periodic bond chains (PBCs; i.e. uninterrupted chains of strong bonds), originally proposed by Hartman and Perdok for relating the crystal structure and the crystal morphology, in a modified way: Even though in the case of whisker growth bounding F-planes (containing at least 2 PBC vectors) cannot be formed because of the constraining neighboring grains in the surface, it is proposed that the whisker axis, which is a zone axis for these F-planes, does run in the direction of a PBC vector, then shared by all these F-planes, as a consequence of the strived for morphology.
- The present experimental results and most of those presented in the literature show that Sn whiskers tend to grow along a direction parallel to a PBC vector. The smaller the number of strong bonds necessary to form a building unit for a PBC, the more frequently Sn whiskers grow along the corresponding PBC vector.
- Nonobservance of all possible whisker-growth directions (as given by PBC vectors comprising a small number (say  $\leq 4$ ) of strong bonds) in a single study can occur due to limited statistics and/or the presence of preferred orientation of the surface grains.

## ***6.7 Acknowledgment***

The authors would like to thank Dr. Ewald Bischof (Max Planck Institute for Intelligent Systems, formerly Max Planck Institute for Metals Research) for performing the EBSD measurements.



## 6.8 References

- [1] K.G. Compton, A.A. Mendizza, S.M. Arnold, *Corrosion* 7, 327-334 (1951).
- [2] G.T. Galyon, *IEEE Trans. Electron. Packag. Manuf.* 28, 94-122 (2005).
- [3] S. Donald, M. Joseph, R.P. Grant, B. McKenzie, W.G. Yelton, *Met. Mat. Trans* 44A, 1485-1496 (2013).
- [4] C. Herring, J.K. Galt, *Phys. Rev.* 85, 1060-1061 (1952).
- [5] B.Z. Lee, D.N. Lee, *Acta Mater.* 46, 3701-3714 (1998).
- [6] K.N. Tu, C. Chen, A.T. Wu, *J. Mater. Sci. – Mater. Electron.* 18, 269-281 (2007).
- [7] M. Sobiech, M. Wohlschloegel, U. Welzel, E.J. Mittemeijer, W. Huegel, A. Seekamp, W. Liu, G.E. Ice, *Appl. Phys. Lett.* 94, 221901 (2009).
- [8] M. Sobiech, U. Welzel, E.J. Mittemeijer, W. Huegel, A. Seekamp, *Appl. Phys. Lett.* 93, 011906 (2008).
- [9] R.R. Hasiguti, *Acta Metall.* 3, 200-201 (1955).
- [10] U. Lindborg, *Acta Metall.* 24, 181-186 (1976).
- [11] W.J. Choi, T.Y. Lee, K.N. Tu, N. Tamura, R.S. Celestre, A.A. MacDowell, Y.Y. Bong, L. Nguyen, *Acta Mater.* 51, 6253–6261 (2003).
- [12] M.E. Williams, K.-W. Moon, W.J. Boettinger, D. Josell, A.D. Deal, *J. Electron. Mater.* 36, 214-219 (2007).
- [13] M. Sobiech, C. Krueger, U. Welzel, J.Y. Wang, E.J. Mittemeijer, W. Huegel, *J. Mater. Res.* 26, 1482-1493 (2011).
- [14] K.S. Kumar, *J. Mater. Res.* 23, 2916–2934 (2008).
- [15] E. Chason, N. Jadhav, W. L. Chan, L. Reinbold, K. S. Kumar, *Appl. Phys. Lett.* 92, 171901 (2008).
- [16] A.E. Pedigo, C.A. Handwerker, J.E. Blendell, *Proc. of the 58th Electron. Comp. & Techn. Conf.*, 1498-1504 (2008).
- [17] V. K. Glazunova, *Sov. Phys. – Crystallogr. Sov. Phys.* 7, 761-766 (1962).
- [18] H. Moriuchi, Y. Tadokoro, M. Sato, T. Furusawa, N. Suzuki, *J. Electron. Mater.* 36, 220-225 (2007).
- [19] S. K. Lin, Y. Yorikado, J. X. Jiang, K. S. Kim, K. Saganuma, S. W. Chen, M. Tsujimoto, I. Yanada, *J. Mater. Res.* 22, 1975 (2007).
- [20] S. K. Lin, Y. Yorikado, J. X. Jiang, K. S. Kim, K. Saganuma, S. W. Chen, M. Tsujimoto, I. Yanada, *J. Electron. Mater.* 36, 1732-1734 (2007).
- [21] B. Horvaacuteth, G. Harsaacutenyi, *Proc. of 15th Intern.Symp. Design Techn. Electron. Pack.* 389 (2009).
- [22] J. W. Osenbach, J. M. DeLucca, B. D. Potteiger, A. Amin, R. L. Shook, F. A. Baiocchi, *IEEE Trans. Electron. Packag. Manuf.* 30, 23-35 (2007).
- [23] E.R. Crandall, G.T. Flowers, P. Lall, M.J. Bozack. *Proc. of the 57th IEEE Holm Conf. Electr. Contacts.* 49 (2011).
- [24] I. Balazs, H. Barbara, H. Gabor. *Surf. Coat. Technol.* 205, 2262 (2010).
- [25] K. Saganuma, A. Baated, K. S. Kim, K. Hamasaki, N. Nemoto, T. Nakagawa, T. Yamada, *Acta Mater.* 59, 7255-7267 (2011)
- [26] G. Galyon, L. Palmer and R. Gedney, *Glob. SMT & Packag.* 5, 10 (2005)
- [27] J. Smetana, *IEEE Trans. Electron. Packag. Manuf.* 30, 11 (2007).
- [28] R.L. Coble, *J. Appl. Phys.* 34, 1679 (1963).

- [29] M. Sobiech, J. Teufel, U. Welzel, E.J. Mittemeijer, W. Huegel, J. Electron. Mater. 40, 2300-2313 (2011).
- [30] K. Whitlaw, J. Crosby, Proc. of AESF SUR/FIN Conf., 289 (2003).
- [31] Britton S. C. Trans. Inst. Metal Finish. 52, 95-102 (1974).
- [32] C. Xu, Y. Zhang, C. Fan, J. A. Abys, CircuitTree 15, 94-105 (2002).
- [33] M. Sobiech, U. Welzel, R. Schuster, E.J. Mittemeijer, W. Huegel, A. Seekamp, V. Mueller, Proc. of IEEE 57th Electro. Comp. Techn. Conf., 192-197 (2007).
- [34] J. W. Osenbach, R. L. Shook, B. T. Vaccaro, B. D. Potteiger, A.N. Amin, K.N. Hooghan, P. Suratkar, P. Ruengsinsub, IEEE Trans. Electron. Packag. Manuf. 28, 36-62 (2005).
- [35] A. Baated, K. Hamasaki, S.S. Kim, K.S. Kim, K. Suganuma, J. Electron. Mater. 40, 2278-2289 (2011).
- [36] R. Schetty, W. Sepp, Proc. of the 11th Electron. Packag. Techn. Conf., 225-234 (2009).
- [37] N. Jadhav, M. Williams, F. Pei, G. Stafford, E. Chason, J. Electro. Mat. 42, 312-318 (2013).
- [38] J. Stein, S. Rehm, U. Welzel, W. Huegel, E.J. Mittemeijer. J. Electron. Mater. 43, 4308-4316 (2014).
- [39] V. K. Glazunova, N. T. Kudryavtsev, Zh. Prikl. Khim. 36, 543-550 (1963).
- [40] NASA, Whisker Failures: <http://nepp.nasa.gov/whisker/failures/index.htm>.
- [41] J.R. Michael, B.B. McKenzie, D.F. Susan, Microscop. Microanal. 18, 876-84 (2012).
- [42] D.F. Susan, J.R. Michael, W. Graham Yelton, B.B. McKenzie, R.P. Grant, J. Pillars, M.A. Rodriguez. Understanding and predicting metallic whisker growth and its effect on reliability: LDRD final report. (New Mexico/California, Sandia National Laboratories, 2012).
- [43] P. Hartman, W.G. Perdok, Acta Cryst 8, 49-52 (1955).
- [44] P. Hartman, W.G. Perdok, Acta Cryst 8, 521-524 (1955).
- [45] N. Jadhav, E. Buchovecky, E. Chason, A. Bower, JOM 62, 30-37 (2010).
- [46] J. Stein, U. Welzel, W. Huegel, S. Blatt, E.J. Mittemeijer, J. Appl. Cryst. 46, 1645-1653 (2013).
- [47] F.R.N. Nabarro, P.J. Jackson, Growth and Perfection of Crystals (John Wiley & Sons; Inc, New York, 1958).
- [48] R.G. Treuting, S.M. Arnold, Acta Met. 5, 598-598 (1957).
- [49] H.G. Smith, R.E. Rundle. J. Appl. Phys. 29, 679-683 (1958).
- [50] W. C. Ellis, D. F. Gibbons, R. C. Treuting, Growth and Perfection of Crystals (Wiley, New York, 1958).
- [51] W.C. Ellis, Trans. Met. Soc. AIME 236, 872-875 (1966).
- [52] R.B. Morris, W. Bonfield, Scripta Met. 8, 231-236 (1974).
- [53] B. Hutchinson, J. Oliver, M. Nysten, J. Hagstrom, Mat. Sci. Forum 467-470, 465-470 (2004).
- [54] A. Frye, G.T. Galyon, L. Palmer, IEEE Trans. Electron. Pack. Manuf. 30, 2-10 (2007).
- [55] T.C. Chiu, K.L. Lin, Scripta Mat. 60, 1121-1124 (2009).
- [56] E. Schmid, W. Boas. Kristallplastizität (Berlin, Julius Springer, 1935).

## Chapter 7

### 7 Summary

#### 7.1 Summary in English

The present thesis project deals with the build-up of stresses and stress relaxation mechanisms in thin Sn(-based) films electro-deposited on pure Cu or Cu-alloy substrates. In particular, the spontaneous formation of Sn whiskers, i.e. the growth of single crystalline, needle-like filaments on the Sn film surface, and its mitigation, is taken into focal point of this study. Thereby, new-developed and well-known methods and analysis techniques have been applied in order to investigate i) the specimen composition, ii) the film- and substrate microstructure and iii) the state of the film stress in the initial state as well as during storage at room temperature. Further, the crystallographic growth directions of Sn whiskers have been investigated and a model, on basis of the concept of periodic bond chains as proposed by Hartmann and Perdok, has been derived for explanation.

In *chapter 2*, an in-situ two-dimensional (2D) detector X-ray diffraction technique has been applied on aging pure Sn films electro-deposited on Cu substrates in order to trace local microstructural changes in residually stressed Sn films.

Changes of diffraction spots in the 2D-diffraction patterns (see Fig. 7-1) were observed, as e.g. emergences, disappearances or migrations as well as increases and/or decreases of intensities of diffraction spots. These diffraction spots on the 2D diffraction patterns originate from (usually) only single Sn grains located within the Sn film microstructure. All observed changes of diffraction spots have been assigned to local microstructure changes in the Sn film: Grain rotation, grain growth and grain dissolution processes could be observed during and even before the onset Sn whisker growth.

Grain rotation is generally exhibited by the abrupt appearance and disappearance of individual diffraction spots. Tangential migration of the diffraction spot along the diffraction circle/ellipse took place in case the orientation of the axis of grain rotation

was close to that of the incident beam. A slowly occurring, cyclic increase and decrease of intensity of the diffraction spot was observed in case the orientation of the axis of grain rotation is close to that of the diffraction vector. Furthermore, radial migration of the diffraction spot is caused by local changes of the internal stress state. Also, a gradual, monotonous increase or decrease of intensity of the diffraction spots was presented which could be associated to grain growth or grain dissolution of grains located in the Sn film.

The development of the intermetallic compound,  $\text{Cu}_6\text{Sn}_5$ , at the Sn layer/Cu substrate interface leading to the occurrence of stress-induced (Coble-type) creep is responsible for these exposed changes of the microstructure of the Sn films upon room temperature aging: In so-called post-baked specimens, where the built-up of stress-gradients does not take place, none of those (local) microstructural changes was observed.

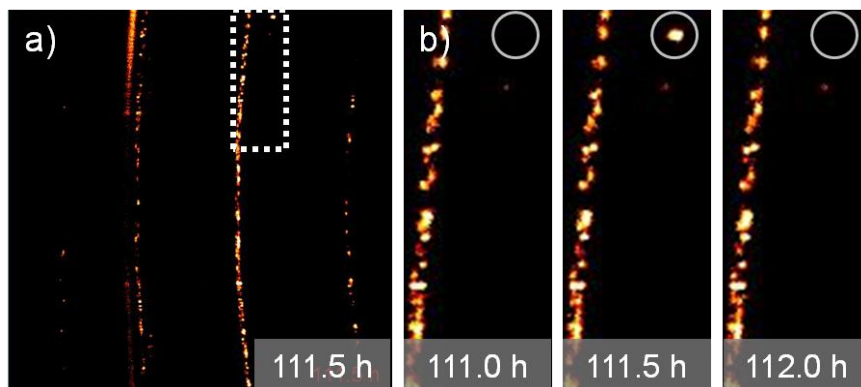


Fig. 7-1: Exemplary 2D diffraction pattern (a) and enlarged series of cutouts (b) indicating a change in the 2D diffraction pattern: An additional appearing and subsequently disappearing Sn diffraction spot (see white circle).

In chapter 3, the impact of alloying Ag to pure Sn films on the formation of Sn whiskers has been explained. In the as-deposited Sn,Ag films (containing silver of about 6 wt.%), a film microstructure with partially columnar and partially equiaxed Sn grains as well as isolated  $\text{Ag}_3\text{Sn}$  precipitates along the Sn/Sn grain boundaries have been observed (see Fig. 7-2).

During room temperature storage of these specimens, Sn whisker growth did not occur even though the formation of the IMC  $\text{Cu}_6\text{Sn}_5$  took place at the film/substrate

interface in an irregular manner with a similar growth rate as observed in whiskering pure Sn/Cu specimens.

The Sn,Ag film microstructure allows global stress relaxation since inclined, with respect to the specimen surface, grain boundaries of equiaxed grains are found at many locations within the film. The stress relaxation in the Sn,Ag films is accommodated by grain-shape changes and grain-boundary sliding processes and is accompanied by coarsening (extensive lateral grain growth) as a consequence of enhanced grain-boundary mobility due to segregated Ag. Thereby, the initial, more or less homogeneous, distribution of  $\text{Ag}_3\text{Sn}$  along the Sn grain boundaries has not been maintained upon aging.

In contrast to the Sn,Ag films, stress relaxation in pure Sn films with a predominantly columnar microstructures can only take place locally where at a few locations at the surface, inclined grain boundaries occur: Sn whiskers develop at these locations.

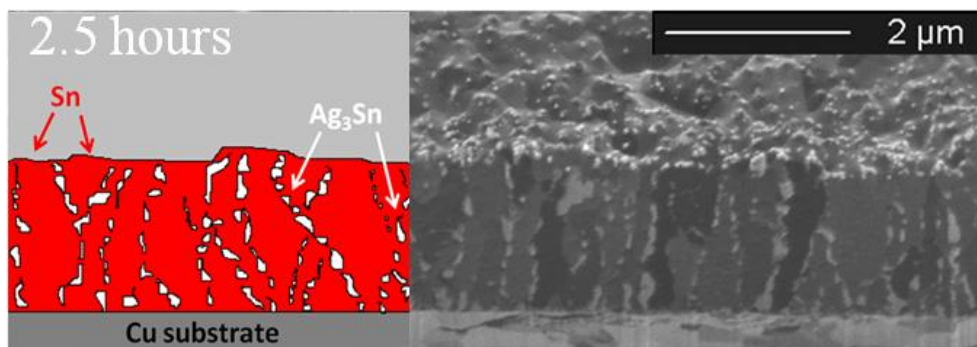


Fig. 7-2: FIB image of a cross-section prepared by FIB milling and sketch (left-hand side) showing a Sn,Ag/Cu specimen in the initial (i.e. as-deposited) state.

In chapter 4, pure Sn films electro-deposited on Cu substrates containing Zn as alloying element have been investigated. In particular, the impact of the Zn (content) in the substrate on the interfacial reaction between Cu and Sn and its consequences for the formation of Sn whiskers has been in focal point in this chapter.

The  $\text{Cu}_6\text{Sn}_5$  formation rate was greatly slowed down in Sn/Cu(Zn) specimens as compared to Sn/pure Cu specimens (see Fig. 7-3) since the driving force for the  $\text{Cu}_6\text{Sn}_5$

formation at the film/substrate interface was lower in the Sn/Cu-alloy specimens (as compared to Sn/pure Cu specimens): The difference of the chemical potential of Cu between substrate and film was reduced in Sn/Cu(Zn) specimens as the chemical potential of a component in an (ideal) solid solution is proportional to the logarithm of the concentration of that component.

Hence, substantial stress relaxation by Coble creep could occur before pronounced stress-depth gradients developed. Thus, significant transport of Sn from the bottom part to the top part of the Sn film did not take place and no Sn whiskers developed on top of the film surfaces.

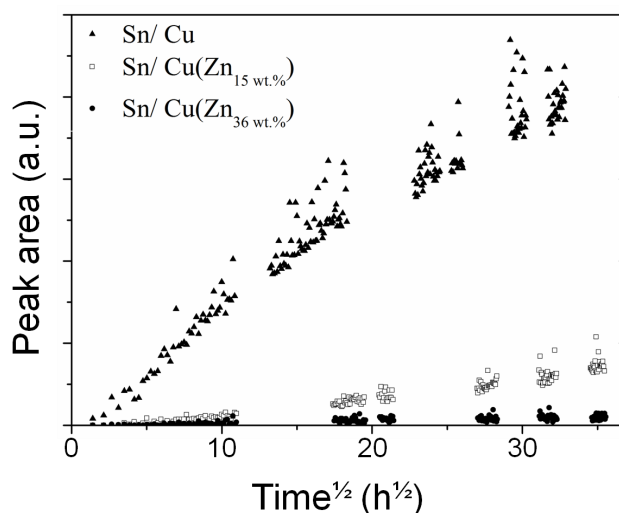


Fig. 7-3: Plot shows results of X-ray diffraction integrated intensity (peak-area) measurements of the  $\text{Cu}_6\text{Sn}_5$  24-1 reflection as a function of aging time at room temperature for Sn/Cu(Zn) and Sn/Cu specimens. The  $\text{Cu}_6\text{Sn}_5$  formation rate is greatly slowed down in the Sn/Cu(Zn) specimens as compared to the Sn/pure Cu specimen.

In chapter 5, two independent X-ray diffraction methods have been employed on specimens mounted on a newly developed device (see Fig. 7-4), consisting of a custom-made glass cylinder provided with a connection piece for vacuum tubes, a needle valve, a vacuum pump and a pressure gauge. This method, the so-called wafer-curvature method, provides an easy and controllable way for imposition of defined strain/stress states in thin films, deposited on (Si-)wafer substrates.

Validation of this method has been carried out using a W film of 500 nm thickness, where it was shown that both X-ray diffraction techniques (conventional

X-ray diffraction stress analysis on the film material and radii of curvature measurements on the substrate material) provide the same values for the state of imposed stress in the film.

Furthermore, this wafer curvature method has been applied on an aging (potentially whiskering) Sn film of 3  $\mu\text{m}$  thickness with a predominantly columnar microstructure. A homogeneous compressive stress in the Sn film, close to the yield limit of Sn, has been induced which, however, did not lead to formation of Sn whiskers or hillocks on the film surface. This finding confirmed that stress gradients are essential for inducing whisker and/or hillock formation

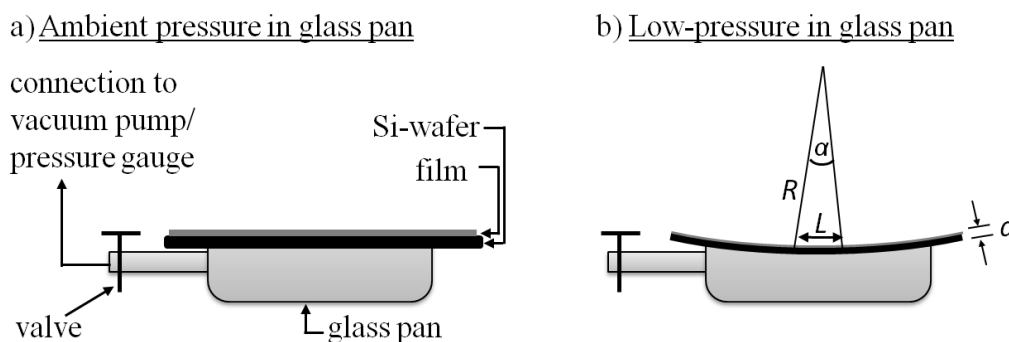


Fig. 7-4: Sketch of the experimental setup developed in this project. A coated Si-wafer fixed on top of the glass pan (see a)) can be bent when evacuating the glass cylinder to a defined low-pressure (see b)).

In Chapter 6, a model has been derived describing the probability for Sn whiskers for growing along certain crystallographic growth directions in the crystal structure. Therefore, the concept of periodic bond chains (PBC, i.e. uninterrupted chains of strong bonds), originally proposed by Hartman and Perdok, has been applied in a modified way.

For an experimental basis, crystallographic growth directions of 55 Sn whiskers were determined by measuring the physical growth angles of the whiskers with respect to a specimen frame of reference and the orientations of the whisker grains with respect to the crystallographic frame of reference.

The experimental findings of this study (frequently found whisker growth directions were:  $\langle 100 \rangle$ ,  $\langle 101 \rangle$  and  $\langle 111 \rangle$ , see Fig. 7-5) and also most of the results presented in the literature fit well to the model derived: Sn whiskers tend to grow along a direction parallel to a PBC vector and the smaller the number of strong bonds necessary to form a building unit for a PBC, the more frequently Sn whiskers grow along the corresponding PBC vector.

This can be understood when realizing that Sn whiskers cannot grow freely in all (three) dimensions because of the constraining neighboring grains in the surface. Thus Flat(F)-planes (containing at least 2 PBC vectors according to the Hartman-Perdok concept) bounding the whisker cannot form; however, it is proposed that the whisker axis, which is a zone axis for these F-planes, does run in the direction of a PBC vector.

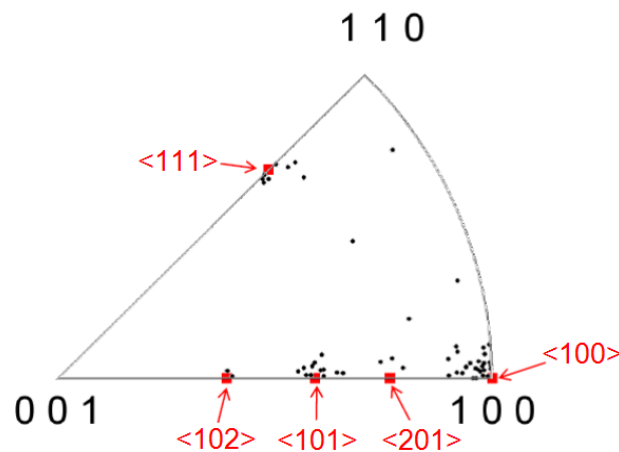


Fig. 7-5: Crystallographic orientations of the axes of 55 whiskers plotted in an inverse pole figure of  $\beta$ -tin indicating that Sn whiskers grow preferentially along low-indexed directions.

## 7.2 Zusammenfassung in Deutsch

Die vorliegende Arbeit befasst sich mit dem Aufbau von Spannungen und den Spannungsrelaxationsmechanismen in dünnen Zinn(-Basis)-Schichten, welche zuvor elektrolytisch auf reinen Kupfer- oder Kupferlegierungs-Substraten abgeschieden wurden. Im Besonderen wurde die Entstehung von Zinn-Whiskern, d.h. das Wachstum von einkristallinen, nadelförmigen Filamenten auf der Oberfläche der Zinn-Schicht sowie deren Verhinderung in den Fokus dieser Arbeit gestellt. Dabei kamen sowohl



neuentwickelte Verfahren, als auch bereits etablierte Analysemethoden zum Einsatz um: i) die Probenzusammensetzung, ii) die Mikrostruktur der Schicht und des Substrats, iii) den Spannungszustand in der Schicht in seinem anfänglichen Zustand sowie während der Lagerung bei Raumtemperatur zu untersuchen. Des Weiteren wurden die kristallografischen Wachstumsrichtungen der Zinn-Whisker untersucht und auf Basis des Konzeptes der periodischen Bindungsketten, wie von Hartman und Perdok vorgeschlagen, ein Model zur Erklärung abgeleitet.

In *Kapitel 2* kam eine in-situ-Röntgenbeugungsmethode zum Einsatz, bei welcher ein zwei-dimensionaler (2D) Detektor verwendet wurde. Diese Methode wurde auf alternden Rein-Zinnschichten, welche zuvor elektrolytisch auf Kupfersubstraten abgeschieden wurden, angewendet, um lokale mikrostrukturelle Veränderungen in den unter Spannung stehenden Zinnschichten zu verfolgen.

Es wurden Veränderungen an Beugungspunkten in den erzeugten 2D-Beugungsbildern beobachtet, wie z.B. Erscheinen, Verschwinden oder Wanderungen sowie Erhöhungen und Verminderungen der Intensität der Beugungspunkte. Diese Beugungspunkte stammen (in den meisten Fällen) von einzelnen Zinnkörnern innerhalb der Zinnschicht. Alle beobachteten Veränderungen in den 2D-Beugungsbildern konnten auf lokale mikrostrukturelle Änderungen in der Zinnschicht zurückgeführt werden: Kornrotation, Kornwachstum und Kornauflösungsprozesse konnten während und sogar vor dem Auftreten von Whisker-Wachstum beobachtet werden.

Kornrotation war durch das abrupte Erscheinen und Verschwinden von einzelnen Beugungspunkten zu erkennen. Eine tangentielle Wanderung von Beugungspunkten entlang des Beugungskreises/der Beugungsellipse fand immer dann statt, wenn die Orientierung der Kornrotationsachse nahe der des einfallenden Röntgenstrahls war. Eine langsame, zyklische Erhöhung und Verminderung der Intensität eines Beugungspunktes wurde beobachtet, wenn die Orientierung der Kornrotationsachse nahe der des Beugungsvektors war. Des Weiteren wurden radiale Wanderungen eines Beugungspunktes durch lokale Änderungen des inneren Spannungszustandes verursacht. Auch wurde eine allmähliche, monotone Erhöhung oder Verminderung der Intensität eines Beugungspunktes gezeigt, welche mit

Wachstum oder Auflösung eines Kornes innerhalb der Zinnschicht assoziiert werden konnte.

Die Ausbildung der intermetallischen Phase (IMP)  $\text{Cu}_6\text{Sn}_5$  an der Zinnschicht/Kupfersubstrat-Grenzfläche, welche spannungsinduziertes (Coble-)Kriechen verursacht, ist verantwortlich für diese exponierten Veränderungen in der Mikrostruktur der Zinnschicht während der Alterung bei Raumtemperatur: In sogenannten „post-baked“ (d.h. wärmebehandelten) Proben, bei denen kein Aufbau von Spannungsgradienten stattfindet, wurden auch keine (lokalen) mikrostrukturellen Veränderungen beobachtet.

In *Kapitel 3* wurde der Einfluss von Silber als Legierungselement auf die Ausbildung von Zinn-Whiskern auf Sn,Ag-Schichten erläutert. Im Ausgangszustand, d.h. direkt nach der Abscheidung der Sn,Ag-Schicht (der Silbergehalt betrug ungefähr 6 gew.%), konnte eine Mikrostruktur der Schicht beobachtet werden, die teilweise säulenförmige und teilweise kugelähnlichen Körner sowie isolierte  $\text{Ag}_3\text{Sn}$  Ausscheidungen entlang der Sn/Sn-Korngrenzen aufwies.

Während der Raumtemperaturalterung dieser Proben trat kein Whisker-Wachstum auf, obwohl die Ausbildung der IMP  $\text{Cu}_6\text{Sn}_5$  an der Schicht/Substrat-Grenzfläche in irregulärer Art und Weise und mit einer ähnlichen Wachstumsrate wie bei whiskernden Rein-Zinn/Kupfer-Proben stattfand.

Die Mikrostruktur der Sn,Ag-Schicht ermöglicht globale Spannungsrelaxation, da an vielen Stellen innerhalb der Schicht zur Oberfläche geneigte Korngrenzen der kugelähnlichen Körner zu finden sind. Spannungsrelaxationsprozesse in der Sn,Ag-Schicht können durch Formänderungen des Kornes und Korngrenz-Gleitprozesse aufgefangen werden. Zudem findet Kornvergrößerung (starkes laterales Kornwachstum) statt, da die Korngrenzmobilität aufgrund segregierten Silbers erhöht ist. Dabei geht jedoch die anfänglich mehr oder weniger homogene Verteilung des  $\text{Ag}_3\text{Sn}$  entlang der Zinn-Korngrenzen verloren.

Im Gegensatz zu den Sn,Ag-Schichten findet Spannungsrelaxation in reinen Zinnschichten mit vornehmlich säulenförmiger Mikrostruktur nur lokal an wenigen

Stellen (an denen zur Oberfläche geneigte Korngrenzen zu finden sind) statt: An diesen Stellen tritt Zinn-Whiskerwachstum auf.

In *Kapitel 4* wurden reine Zinnschichten untersucht, die elektrolytisch auf Kupfersubstraten, welche Zink als Legierungselement enthielten, abgeschieden wurden. Im Besonderen wurde der Einfluss des Zinks auf die Grenzflächenreaktion zwischen Kupfer und Zinn sowie die Konsequenzen auf die Zinn-Whiskerbildung, betrachtet.

Die  $\text{Cu}_6\text{Sn}_5$ -Bildung in Sn/Cu(Zn) Proben ist verglichen mit der in Sn/Rein-Cu Probe stark verlangsamt, da die Triebkraft für die  $\text{Cu}_6\text{Sn}_5$  Bildung an der Schicht/Substrat-Grenzfläche kleiner in der Sn/Kupferlegierung Probe ist (im Vergleich zur Sn/Rein-Cu Probe): Die Differenz des chemischen Potentials des Kupfers zwischen Substrat und Schicht ist in Sn/Cu(Zn) Proben reduziert, da das chemische Potential einer Komponente in einem (idealen) Mischkristall proportional zum Logarithmus der Konzentration dieser Komponente ist.

Aufgrund der relativ langsamen  $\text{Cu}_6\text{Sn}_5$  Bildung in Sn/Cu(Zn) Proben konnte beträchtliche Spannungsrelaxation durch Coble-Kriechen stattfinden bevor signifikante Spannungs-Tiefen Gradienten entstanden. Folglich fand kein signifikanter Zinntransport vom unteren zum oberen Teil der Zinnschicht statt und die Bildung von Zinn-Whiskern auf der Oberfläche der Schicht blieb aus.

In *Kapitel 5* wurden zwei voneinander unabhängige Röntgen-Spannungsanalyse-Methoden verwendet: Die Proben wurden hierfür auf einem neu entwickelten Apparat fixiert, welcher aus einem speziell angefertigten Glaszylinder mit Anschluss für Vakuumschläuche, einem Nadelventil, einer Vakuumpumpe und einem Druckmessgerät, bestand. Diese Methode, die sogenannte Waferkrümmungsmethode, bietet eine leicht zu kontrollierende Möglichkeit, um definierte Dehnungs-/Spannungszustände in dünnen Schichten auf Si-Wafer Substraten zu erzeugen.

Die Validierung dieser Methode wurde mit Hilfe einer 500 nm dicken Wolframschicht durchgeführt. Hierbei konnte gezeigt werden, dass beide Röntgenbeugungsmethoden (konventionelle Röntgenbeugungs-Spannungsanalyse am Schichtmaterial und Krümmungsmessungen am Substratmaterial) vergleichbare Werte für die auf die Schicht auferlegte Spannung zeigen.

Des Weiteren wurde die Waferkrümmungsmethode an alternden (potentiell whiskernden) 3  $\mu\text{m}$  dicken Zinnschichten mit vornehmlich säulenförmiger Mikrostruktur angewendet. Ein homogener Spannungszustand nahe der Fließgrenze des Zinns wurde induziert. Dieser führte jedoch nicht zur Bildung von Zinn-Whiskern oder Hillocks auf der Schichtoberfläche. Dieses Ergebnis bestätigt, dass Spannungsgradienten essentiell für die Indizierung von Whiskern und/oder Hillocks sind.

In *Kapitel 6* wurde ein Model abgeleitet, welches die Wahrscheinlichkeit beschreibt, dass ein Zinnwhisker entlang einer bestimmten kristallografischen Richtung in der Kristallstruktur wächst. Dafür wurde das Konzept der periodischen Bindungsketten (PBk, d.h. ununterbrochene Ketten starker Bindungen), welches ursprünglich von Hartman und Perdok entwickelt wurde, angewandt.

Als experimentelle Grundlage wurden die kristallografischen Richtungen von 55 Zinnwhiskern durch Messung der physischen Wachstumswinkel zum Probenkoordinatensystem und Messung der Orientierungen der Whiskerkörner zum Kristallkoordinatensystem bestimmt.

Die experimentellen Ergebnisse dieser Untersuchung (häufig gefundene Whiskerwachstumsrichtungen waren die:  $\langle 100 \rangle$ ,  $\langle 101 \rangle$  und  $\langle 111 \rangle$ ) und auch die meisten derer, die in der Literatur präsentiert wurden, passen gut zu dem abgeleiteten Model: Zinn-Whisker tendieren zu einem Wachstum parallel zu einer PBk. Je kleiner die Anzahl der starken Bindungen ist, welche für die Bildung eine Bindungskette benötigt wird, desto häufiger wachsen Zinn-Whisker entlang des entsprechenden PBk-Vektors.

Dies ist verständlich wenn man sich vor Augen hält, dass Zinn-Whisker nicht frei in allen (drei) Dimensionen wachsen können, da dies von Nachbarkörner an der Oberfläche behindert wird. Daher können Fläche(F)-Ebenen als Whisker-Oberflächen (welche mindestens 2 PBk-Vektoren gemäß des Hartman und Perdoks Konzeptes enthalten) nicht entstehen. Es wurde jedoch vorgeschlagen, dass die Whisker-Achse, welche eine Zonenachse für diese F-Ebenen wäre, genau in die Richtung eines PBk-Vektors verläuft.

## List of publications

1. Aging-time-resolved in situ microstructural investigation of tin films electroplated on copper substrates, applying two-dimensional-detector X-ray diffraction.  
J. Stein, U. Welzel, W. Hügel, S. Blatt and E.J. Mittemeijer.  
Journal of Applied Crystallography, Volume 46, pp. 1645–1653 (2013).  
Chapter 2 of this thesis.
2. The role of silver in mitigation of whisker formation on thin tin films  
J. Stein, S. Rehm, U. Welzel, W. Hügel and E.J. Mittemeijer.  
Journal of Electronic Materials, Volume 43, Issue 11, pp. 4308-4316 (2014).  
Chapter 3 of this thesis.
3. Microstructural development and possible whiskering behavior of thin Sn films electrodeposited on Cu(Zn) substrates.  
J. Stein, C.A. Cordova Tineo, U. Welzel, W. Hügel and E.J. Mittemeijer.  
Journal of Electronic Materials, Volume 44, Issue 3, pp. 886-894 (2015).  
Chapter 4 of this thesis.
5. Imposition of defined states of stress on thin films by a wafer-curvature method; validation and application to aging Sn films.  
J. Stein, M. Pascher, U. Welzel, W. Hügel and E.J. Mittemeijer.  
Thin Solid Films, Volume 568, pp. 52–57 (2014).  
Chapter 5 of this thesis.
6. The crystallographic growth directions of Sn whiskers.  
J. Stein, U. Welzel, A. Leineweber, W. Hügel and E.J. Mittemeijer.  
Acta Materialia, Volume 86, pp. 102–105 (2015).  
Chapter 6 of this thesis.



## Danksagung

Die vorliegende Arbeit wurde am Max-Planck-Institut für Intelligente Systeme (ehemals Max-Planck-Institut für Metallforschung) in Stuttgart, bei der Robert Bosch GmbH (Geschäftsbereich Automotive Electronics) in Schwieberdingen und dem Institut für Materialwissenschaft der Universität Stuttgart durchgeführt.

An erster Stelle möchte ich mich bei meinem Doktorvater, Herrn Prof. Dr. Ir. E.J. Mittemeijer, bedanken: Zum einen für die Möglichkeit der Anfertigung dieser Arbeit in seiner Abteilung, zum anderen für das außergewöhnlich große Engagement sowie die exzellente wissenschaftliche Betreuung, die maßgeblich zum Gelingen dieser Arbeit beigetragen hat. Insbesondere der regelmäßige, konstruktive Austausch hat mich stets motiviert und darin bestärkt, meine wissenschaftlichen Vorstellungen und Gedanken frei zu formulieren.

Herrn Prof. Dr. T. Schleid danke ich für die Bereitschaft den Prüfungsvorsitz zu übernehmen und Herrn Prof. Dr. J. Bill für die freundliche Übernahme des Mitberichts.

Desweiteren gilt mein Dank der Robert Bosch GmbH (Geschäftsbereich Automotive Electronics), im Besonderen allen Vorgesetzten und Mitarbeitern der Abteilung „Aufbau und Verbindungstechnik“ für die tatkräftige Unterstützung während der Erstellung dieser Arbeit.

Ebenfalls danke ich Herrn Dr. U. Welzel (Max-Planck-Institut für Intelligente Systeme, später Robert Bosch GmbH) für die tägliche Betreuung sowie für die wissenschaftliche Unterstützung während der Erstellung dieser Arbeit. Auch möchte ich mich für die Betreuung und den wissenschaftlichen Austausch bei Herrn Dr. W. Hügel (Robert Bosch GmbH) bedanken.

Bei allen Mitarbeitern und Doktorandenkollegen der Abteilung Prof. Mittemeijer des Max-Planck-Institut für Intelligente Systeme (ehemals Max-Planck-Institut für Metallforschung) möchte ich mich für die Unterstützung und die stets angenehme Zusammenarbeit bedanken. Hierbei gilt mein besonderer Dank Silke für die gemeinsamen Gespräche und ihre unermüdliche Unterstützung sowie Holger und Thomas für die freundschaftliche Zusammenarbeit.

Einen sehr herzlichen Dank möchte ich meinen lieben Eltern, Christina und Rainer, sowie meiner lieben Schwester Julia für die jahrelange Unterstützung aussprechen. Ganz besonders möchte ich auch meiner geliebten Frau Annika und meiner kleinen Tochter Lenya danken: Vielen Dank, dass ihr immer für mich da seid!





# Curriculum vitae

## *Persönliche Angaben*

Name: Jendrik Stein  
Geburtstag: 07. September 1983  
Geburtsort: Böblingen  
Staatsangehörigkeit: deutsch

## *Schulische Ausbildung*

August 2000 - Juni 2001 High-School in Lynchburg (VA), USA  
bis Juni 2003 Grundschule und Gymnasium in Böblingen  
Abschluss: Allgemeine Hochschulreife

## *Studium*

Oktober 2003 - Oktober 2004 Studiengang: Maschinenbau  
an der Universität Karlsruhe (TH)  
Oktober 2004 - Mai 2009 Studiengang: Werkstoffwissenschaft  
an der Universität Stuttgart  
Mai 2009 - November 2009 Diplomarbeit: „Löslichkeit von Stickstoff in Ferrit“  
an der Universität Stuttgart, Institut für Materialwissenschaft in Kooperation mit dem Max-Planck-Institut für Metallforschung (heute: Max-Planck-Institut für Intelligente Systeme), Stuttgart.  
Hauptberichter: Prof. Dr. Ir. E.J. Mittemeijer.

## *Promotion*

Seit Februar 2010 Promotionsthema: „Stress relaxation mechanisms in thin Sn films and its alloys – Sn whisker formation and its mitigation“ am Max-Planck-Institut für Intelligente Systeme (ehemals Max-Planck-Institut für Metallforschung), Stuttgart, und Institut für Materialwissenschaft, Universität Stuttgart, in Kooperation mit der Robert Bosch GmbH (Abteilung: AE/EAI), Schwieberdingen.  
Hauptberichter: Prof. Dr. Ir. E.J. Mittemeijer.



## **Erklärung über die Eigenständigkeit der Dissertation**

Ich versichere, dass ich die vorliegende Arbeit mit dem Titel:

„Stress relaxation mechanisms in thin Sn films and its alloys –  
Sn whisker formation and its mitigation“

selbständig verfasst und keine anderen als die angegebenen Quellen und Hilfsmittel benutzt habe; aus fremden Quellen entnommene Passagen und Gedanken sind als solche kenntlich gemacht.

## **Declaration of Authorship**

I hereby certify that the dissertation entitled

„Stress relaxation mechanisms in thin Sn films and its alloys –  
Sn whisker formation and its mitigation“

is entirely my own work except where otherwise indicated. Passages and ideas from other sources have been clearly indicated.

Name/Name: \_\_\_\_\_

Unterschrift/Signed: \_\_\_\_\_

Datum/Date: \_\_\_\_\_



